Universidade Federal de Juiz de Fora

Instituto de Ciências Exatas

Programa de Pós-Graduação em Modelagem Computacional

Rosmery Violeta Quispe Zavala

Traveling waves for the Newtonian foam displacement in porous media

Juiz de Fora

2022

Rosmery Violeta Quispe Zavala

Traveling waves for the Newtonian foam displacement in porous media

Tese apresentada ao Programa de Pós-Graduação em Modelagem Computacional da Universidade Federal de Juiz de Fora como requisito parcial para obtenção do grau de Doutor em Modelagem Computacional.

Orientador: Grigori Chapiro

Coorientador: Luis Fernando Lozano Guerrero

Juiz de Fora

2022

Ficha catalográfica elaborada através do programa de geração
automática da Biblioteca Universitária da UFJF,
com os dados fornecidos pelo(a) autor(a)

Quispe Zavala, Rosmery Violeta.
Traveling waves for the Newtonian foam displacement in porous media / Rosmery Violeta Quispe Zavala. -- 2022.
105 f.

Orientador: Grigori Chapiro
Coorientador: Luis Fernando Lozano Guerrero
Tese (doutorado) - Universidade Federal de Juiz de Fora, Instituto de Ciências Exatas. Programa de Pós-Graduação em Modelagem Computacional, 2022.

1. Foam Flow. 2. Porous Media. 3. Traveling Wave. 4. Riemann Problem. I. Chapiro, Grigori, orient. II. Lozano Guerrero, Luis Fernando, coorient. III. Título.

Rosmery Violeta Quispe Zavala

Traveling waves for the Newtonian foam displacement in porous media

Tese apresentada ao Programa de Pós-Graduação em Modelagem Computacional da Universidade Federal de Juiz de Fora como requisito parcial à obtenção do título de Doutora em Modelagem Computacional. Área de concentração: Modelagem Computacional.

Aprovada em 07 de outubro de 2022.

BANCA EXAMINADORA

Prof(a) Dr(a). Grigori Chapiro - Orientador

Universidade Federal de Juiz de Fora

Prof(a) Dr(a). Luis Fernando Lozano Guerrero - Coorientador

Universidade Federal de Juiz de Fora

Prof(a) Dr(a). Pacelli Lidio José Zitha

Technische Universiteit Delft

Prof(a) Dr(a). Pablo Castañeda Rivera

Instituto Tecnológico Autónomo de México

Prof(a) Dr(a). Rodrigo Weber dos Santos

Universidade Federal de Juiz de Fora

Prof(a) Dr(a). Pavel Zenon Sejas Paz

Universidade Federal de Juiz de Fora

Juiz de Fora, 28/09/2022.

Documento assinado eletronicamente por **Pavel Zenon Sejas Paz**, **Usuário Externo**, em 07/10/2022, às 12:43, conforme horário oficial de Brasília, com fundamento no § 3º do art. 4º do Decreto nº 10.543, de 13 de novembro de 2020.

Documento assinado eletronicamente por **Pablo Castañeda Rivera**, **Usuário Externo**, em 07/10/2022, às 14:29, conforme horário oficial de Brasília, com fundamento no § 3º do art. 4º do Decreto nº 10.543, de 13 de novembro de 2020.

Documento assinado eletronicamente por **LUIS FERNANDO LOZANO GUERRERO**, **Usuário Externo**, em 10/10/2022, às 07:45, conforme horário oficial de Brasília, com fundamento no § 3º do art. 4º do Decreto nº 10.543, de 13 de novembro de 2020.

Documento assinado eletronicamente por **Grigori Chapiro**, **Professor(a)**, em 13/10/2022, às 08:47, conforme horário oficial de Brasília, com fundamento no § 3º do art. 4º do Decreto nº 10.543, de 13 de novembro de 2020.

Documento assinado eletronicamente por **Rodrigo Weber dos Santos**, **Professor(a)**, em 13/10/2022, às 16:23, conforme horário oficial de Brasília, com fundamento no § 3º do art. 4º do Decreto nº 10.543, de 13 de novembro de 2020.

Documento assinado eletronicamente por **Pacelli Lídio José Zitha**, **Usuário Externo**, em 13/10/2022, às 19:01, conforme horário oficial de Brasília, com fundamento no § 3º do art. 4º do Decreto nº 10.543, de 13 de novembro de 2020.

A autenticidade deste documento pode ser conferida no Portal do SEI-Ufjf (www2.ufjf.br/SEI) através do ícone Conferência de Documentos, informando o código verificador **0969746** e o código CRC **1074A294**.

ACKNOWLEDGMENTS

I thank Deus for helping me through each person I met.

I thank my family, who encourage me to keep going, for facing new challenges to help me. I thank my parents for teaching me to love and to continue until the last. I thank my mom, who lives in my heart and in who loves her, a beautiful woman of great character. I thank my father, who always credits me and puts his children first; he is very dedicated and honest. I thank all my siblings Doris, Deysi, Flor, Lenin, Edil, Wilder, and Teo for their words and support each who to their form.

I thank to my advisors, this work materialized thanks their experience and support. I thank my advisor Dr. Grigori Chapiro, for his patience and care in leading me from my master's time. I thank him for trusting me and allowing me to fulfill my dream of obtaining my doctorate. My co-advisor Dr. Luis F. Lozano shared ideas and experiences with me.

I thank the examining board members who have carefully prepared suggestions for improving this thesis.

I thank my friends Carlos Lito, Carlos Mamani, Manuel Argomedo, and Edgar Rodriguez, who supported me continuously from before the doctor's time. I thank Manuel, Yvonne, Nelson, Alfeu, Tino, Julio, Santiago, Pablo, Daniel, Yobani, and Ronald for their time and love with whom I shared important moments.

I thank the LAMAP group for their knowledge shared in seminars and for preparing material important for our area, mainly to Juan and Andrés, whom I went to the most.

I thank FAPEMIG and SHELL Brasil LTDA, without financial support, without which this work would not be possible.

This work was carried out in association with the project R&D ANP 20715-9, "Mathematical and computational modeling of foam injection used in advanced oil recovery" (UFJF/Shell Brasil/ANP). Shell Brasil finances them in accordance with the ANP's R&D&I standards within the framework of the Investment Commitment in Research, Development, and Innovation. These projects are carried out in partnership with Petrobras. G.C. was supported in part by CNPq grant 303245/2019-0 and FAPEMIG grant APQ-00405-21. G.C. and L.L. were supported in part by CNPq grant 405366/2021-3.

"A scientist worthy of his name, above all a mathematician, experiences in his work the same impression as an artist; his pleasure is as great and of the same nature."

Henri Poincaré.

ABSTRACT

This thesis presents the analytical study of three systems of partial differential equations that describe foam flow in porous media. The first two models consider the surfactant concentration fixed above the critical micellar concentration: the linear kinetic model and a simplified version of the stochastic bubble population balance model. A significant difference between these models is the influence of critical water saturation in the first model. The third system generalizes the second by varying the surfactant concentration and considering gas mobility that depends on the surfactant concentration. We study the traveling wave solutions of such systems using phase portrait analysis. All obtained analytical solutions are confirmed using direct numerical simulations of the system of partial differential equations. The second model is validated with experimental data.

Keywords: Foam Flow · Porous Media · Traveling Wave · Riemann Problem

RESUMO

Esta tese apresenta o estudo analítico de três sistemas de equações diferenciais parciais que descrevem o fluxo de espuma em meios porosos. Os dois primeiros modelos consideram a concentração de surfactante fixa acima da concentração micelar crítica: o modelo cinético linear e uma versão simplificada do modelo estocástico de balanço populacional de bolhas. Uma diferença significativa entre estes modelos é a influência da saturação crítica da água no primeiro modelo. O terceiro sistema generaliza o segundo variando a concentração de surfactante e considerando a mobilidade do gás que depende da concentração de surfactante. Estudamos as soluções de ondas viajantes de tais sistemas utilizando a análise de retrato de fase. Todas as soluções analíticas obtidas são confirmadas utilizando simulações numéricas directas do sistema de equações diferenciais parciais. O segundo modelo é validado com dados experimentais.

Palavras-chave: Fluxo de Espuma · Meios Porosos · Ondas Viajantes · Problema de Riemann

LIST OF FIGURES

Figura 1 – Schematic diagram showing the effects of injection gas with and without foam. 21

Figura 2 – Schematic representation of a traveling wave that moves with a constant velocity v. 34

Figura 3 – Equilibria of System (3.12)-(3.13) belong to the intersection of the curve $(S_w, f_w^{LE}(S_w))$ (solid red curve) and lines passing through $(S_w^+, f_w^{LE}(S_w^+))$ with slope v_s (dashed black lines). Depending on the value of S_w^- relative to S_w^b, there are two or three equilibria. 41

Figura 4 – Classification of the eigenvalues of the Jacobian matrix associated to the vector field (3.12)-(3.13) in the semi plane $\{(S_w, K_c) : \ S_{wc} \leq S_w \leq 1 - S_{gr}, \ 0 < K_c < \infty\}$. (a) Classification of regions of S_w^- associated to $S_w^+ = 0.72$. (b) Zoom of regions close to S_w^* on a small box of Figure(a). The dotted line represents the vertical line $S_w = S_w^b$. 42

Figura 5 – Case $(S_w^+, n_D^+) = (0.72, 1)$, $K_c = 1$, and $(S_w^-, n_D^-) = (0.81, 1.0)$ corresponding to Region **I**, see Figure 4. (a) Solutions of System (3.12)-(3.13) in the phase space. There is no traveling wave connection from the left state (S_w^-, n_D^-) to right state (S_w^+, n_D^+). (b) The numerical solution of the Riemann problem (3.2)-(3.3) consists of a rarefaction wave connecting (S_w^-, n_D^-) to (S_w^+, n_D^+). 43

Figura 6 – Case $(S_w^+, n_D^+) = (0.72, 1)$, $K_c = 200$, and $(S_w^-, n_D^-) = (0.372, 0.664)$ corresponding to point A in Region **II**, see Figure 4(a). (a) Solutions of System (3.12)-(3.13) in the phase space. There is a the traveling wave connection from (S_w^-, n_D^-) to (S_w^+, n_D^+). (b) The numerical solution of the Riemann problem (3.2)-(3.3) consists of a traveling wave connecting (S_w^-, n_D^-) to (S_w^+, n_D^+). 44

Figura 7 – Case $(S_w^+, n_D^+) = (0.72, 1)$, $K_c = 1$, and $(S_w^-, n_D^-) = (0.372, 0.664)$ corresponding to point B in Region **III**, see Figure 4(b). (a) Solutions of System (3.12)-(3.13) in the phase space. There is an oscillating connection from (S_w^-, n_D^-) to (S_w^+, n_D^+). (b) The numerical solution of the Riemann problem (3.2)-(3.3) consists of an (oscillating) traveling wave connecting (S_w^-, n_D^-) to (S_w^+, n_D^+). 45

Figura 8 – Zoom on the Region **VI** from Figure 4(a) corresponding to $(S_w^+, n_D^+) = (0.72, 1)$. The curve $\mathcal{C}$ (red) is formed by points (S_w^-, K_c), such that there is a saddle-saddle connection between (S_w^-, n_D^-) and (S_w^+, n_D^+). Points α (left of $\mathcal{C}$), β (on $\mathcal{C}$) and γ (right of $\mathcal{C}$) are in Region **VI**. 45

Figura 9 – Case $(S_w^+, n_D^+) = (0.72, 1)$, $K_c = 10$, and $(S_w^-, n_D^-) = (0.205, 0)$ corresponding to point α in Region **VI**, see Figure 8. (a) Solutions of System (3.12)-(3.13) in the phase space. There is no connection between (S_w^-, n_D^-) and (S_w^+, n_D^+). The point (S_w^e, n_D^e) is also an equilibrium of (3.12)-(3.13) (b) The numerical solution of the Riemann problem (3.2)-(3.3) consists of a rarefaction wave connecting (S_w^-, n_D^-) to $(S_w^{\mathcal{C}}, n_D^{\mathcal{C}})$, followed by the traveling wave to (S_w^+, n_D^+). 46

Figura 10 – Case $(S_w^+, n_D^+) = (0.72, 1)$, $K_c = 10$, and $(S_w^-, n_D^-) = (0.3375, 0)$ corresponding to point β in Region **VI**, see Figure 8. (a) Solutions of System (3.12)-(3.13) in the phase space. There is a saddle-saddle connection between (S_w^-, n_D^-) and (S_w^+, n_D^+) (solid purple curve). The point (S_w^e, n_D^e) is also an equilibrium of (3.12)-(3.13). (b) The numerical solution of the Riemann problem (3.2)-(3.3) consists only of a traveling wave solution connecting (S_w^-, n_D^-) to (S_w^+, n_D^+). 47

Figura 11 – Case $(S_w^+, n_D^+) = (0.72, 1)$, $K_c = 10$, and $(S_w^-, n_D^-) = (0.36995, 0)$ corresponding to point γ in Region **VI**, see Figure 8. (a) Solutions of System (3.12)-(3.13) in the phase space. There is no connection between (S_w^-, n_D^-) and (S_w^+, n_D^+). The point (S_w^e, n_D^e) is also an equilibrium of (3.12)-(3.13). (b) The numerical solution of the Riemann problem (3.2)-(3.3) consists of a shock wave connecting (S_w^-, n_D^-) to $(S_w^{\mathcal{C}}, n_D^{\mathcal{C}})$ followed by the traveling wave to (S_w^+, n_D^+). 47

Figura 12 – Case $(S_w^+, n_D^+) = (0.72, 1)$ with $K_c = 0.5$, $A = 400$ and $(S_w^-, n_D^-) = (0.3705, 0.197375)$ corresponding to Region **IV**, see Figure 4. (a) Solution of System (3.12)-(3.13) in the phase space. There is no connection between (S_w^-, n_D^-) and (S_w^+, n_D^+). The point (S_w^e, n_D^e) is also an equilibrium of (3.12)-(3.13). (b) The numerical solution of the Riemann problem (3.2)-(3.3) consists of an oscillating wave (S_w^-, n_D^-) to $(S_w^{\mathcal{C}}, n_D^{\mathcal{C}})$ followed by a traveling wave to (S_w^+, n_D^+). 48

Figura 13 – Case $(S_w^+, n_D^+) = (0.72, 1)$, $K_c = 0.005$, $A = 200$ and $(S_w^-, n_D^-) = (0.3702, 0.03997867)$ corresponding to Region **V**, see Figure 4. (a) Solution of System (3.12)-(3.13) in the phase space. There is no connection between (S_w^-, n_D^-) and (S_w^+, n_D^+). The point (S_w^e, n_D^e) is also an equilibrium of (3.12)-(3.13). (b) The numerical solution of the Riemann problem (3.2)-(3.3) consists of a wave (S_w^-, n_D^-) to $(S_w^{\mathcal{C}}, n_D^{\mathcal{C}})$ followed by a traveling wave to (S_w^+, n_D^+). 49

Figura 14 – Analysis of instabilities for a small variations of the parameter K_c. (a) The "pinched" part of Region **III** surrounded by Region **II**. Fixing S_w^- we consider three points varying K_c. (b) Profile solution of n_D corresponding to points *1)* and *3)* in Region **II**. (c) Profile solution of n_D corresponding to point *2)* in Region **III**. 50
Figura 15 – Analysis of instabilities for a small variations of S_w^- on the border between regions **II**, **III** and **VI**. (a) Zoom near point $S_w^- = S_w^*$, $K_c = 145$. For a fixed K_c we consider three points varying S_w^- close to S_w^*. (b) Numerical solution profile for point *4)* in Region **VI**. (c) Numerical solution profile for point *5)* in Region **III**. (d) Numerical solution profile for point *6)* in Region **II**. 51
Figura 16 – A decay in the total relative mobility of gas for S_w^- inside Region **VI** close to S_w^*. 51
Figura 17 – Equilibria of System (4.13)-(4.14) for $S_w^+ = 0.999$, $K_g = 0.1$ and $n_{max} = 250$ mm^{-3}. Point S_w^T indicate the intersection point between the curve of f_w and the tangent line to f_w that passes through (S_w^+, f_w^+). Point S_w^M indicate the intersection between the curve of f_w and the line connecting $(S_{wc}, f_w(S_{wc}))$ to (S_w^+, f_w^+). (a) The solid curve represent the water fractional flow in Eq. (4.16). (b) Line $n_D = 1$ along which are the equilibria of System (4.13)-(4.14). 57
Figura 18 – Regions' classification according to the equilibrium type for $S_w^+ = 0.999$ and $K_d = 0$. Points S_w^T (boundary between regions I and II) and S_w^M (boundary between sub-regions with two and three equilibria) are obtained, as explained in Fig. 17. Simulations presented later in this chapter are represented with point $\mathcal{A}$, $\mathcal{F}$ and $\mathcal{G}$ (correspond to Figs. 27 and 28); points $\mathcal{B}$, $\mathcal{C}$ and $\mathcal{D}$ (correspond to Figs. 29 and 30). Experimental results correspond to points $\mathcal{A}$ and $\mathcal{E}$ (see Section 4.3.2). (a) Space $S_w^- \times K_g$ and $n_{max} = 250$ mm^{-3}. (b) Space $S_w^- \times n_{max}$ and $K_g = 0.1$. 58
Figura 19 – Case $S_w^- \in]S_w^M, S_w^+[$. Riemann problem solution for $(S_w^-, n_D^-) = (0.63, 1)$, $(S_w^+, n_D^+) = (0.999, 1)$, $K_g = 0.1$, and $n_{max} = 250$ mm^{-3}. (a) Orbits of System (4.13)-(4.14) in phase portrait. There is an orbit connecting (S_w^-, n_D^-) to (S_w^+, n_D^+). (b) Solution profile of (4.1)-(4.2). 58
Figura 20 – Case $S_w^- \in]S_w^T, S_w^M]$. Riemann problem solution for $(S_w^-, n_D^-) = (0.45, 1)$, $(S_w^+, n_D^+) = (0.999, 1)$, $K_g = 0.1$, and $n_{max} = 250$ mm^{-3}. (a) Orbits of System (4.13)-(4.14) in phase portrait. There is an orbit connecting (S_w^-, n_D^-) to (S_w^+, n_D^+). (b) Solution profile of (4.1)-(4.2). 59

Figura 21 – Schematic representation of System (4.13)-(4.14) solution's bifurcation happening when S_w^- moves between regions I and II (see Fig. 18). Red point represents the saddle equilibrium S_w^+, green point represents the equilibrium (S_w^e, n_D^e), blue point represents the saddle equilibrium S_w^-, and black point represents the node equilibrium $S_w^- = S_w^T$. The upper plane corresponds to Region I, the middle plane to the boundary and the lower plane corresponds to Region II. 60
Figura 22 – Case $S_w^- = S_w^T$. Riemann problem solution for $(S_w^-, n_D^-) = (S_w^T, 1)$, $(S_w^+, n_D^+) = (0.999, 1)$, $K_g = 0.1$, and $n_{max} = 250$ mm^{-3}. (a) Orbits of System (4.13)-(4.14) in phase portrait. There is an orbit connecting (S_w^-, n_D^-) to (S_w^+, n_D^+). (b) Solution profile of (4.1)-(4.2). 60
Figura 23 – Case $S_w^- \in]S_{wc}, S_w^T[$ in Region II, $K_g = 0.1$, and $n_{max} = 250$ mm^{-3}. (a) There is no direct connection from (S_w^-, n_D^-) to (S_w^+, n_D^+). (b) Riemann problem solution of System (4.1)-(4.2) for $(S_w^-, n_D^-) = (0.2, 1)$, $(S_w^+, n_D^+) = (0.999, 1)$. 61
Figura 24 – The apparent viscosity of the system for three different gas velocities 10^{-4} m/s, $3 \cdot 10^{-5}$ m/s, and $5 \cdot 10^{-6}$ m/s. 62
Figura 25 – Water saturation profiles at different times. Experimental data presented in [73] (dark green) compared to the solution of System (4.1)-(4.2) for $K_g = 0.1$, $n_{max} = 250$ mm^{-3} and $S_w^- = 0.63$ (blue). 63
Figura 26 – Water saturation profiles at different times. Experimental data presented in [74] (dark green) compared to the solution of System (4.1)-(4.2) for $K_g = 0.1$, $n_{max} = 250$ mm^{-3} and $S_w^- = 0.43$ (blue). 63
Figura 27 – Water saturation profiles for different values of n_{max} at different times. Here $(S_w, n_D)^- = (0.43, 0)$ and $(S_w, n_D)^+ = (0.999, 0)$. (a) Numerical results using IMPES and complete model, see [74]. (b) Solution of System (4.1)-(4.2). 64
Figura 28 – Bubble density profiles for different values of n_{max} at different times. Here $(S_w, n_D)^- = (0.43, 0)$ and $(S_w, n_D)^+ = (0.999, 0)$. (a) Numerical results using IMPES and complete model, see [74]. (b) Solution of System (4.1)-(4.2). 65
Figura 29 – Water saturation profiles for different values of K_g at different times. Here $n_{max} = 250$ and $(S_w, n_D)^+ = (0.999, 0)$. (a) Numerical results using IMPES and complete model, see [74]. (b) Solution of System (4.1)-(4.2). 66
Figura 30 – Bubble density profiles for different values of K_g at different times. Here $n_{max} = 250$ and $(S_w, n_D)^+ = (0.999, 0)$. (a) Numerical results using IMPES and complete model, see [74]. (b) Solution of System (4.1)-(4.2). 66

Figura 31 – Comparison between the functions MRF and MF^{-1} corresponding to the population balance model proposed in this chapter under LE conditions and the model implemented in CMG/STARS simulator. . . 71
Figura 32 – Water fractional flow for different values of C for the case $C_{cmc} = 0.8$. The vertical dotted line corresponds to $S_w^+ = 0.94$. The purple line passes through the point (S_w^+, f_w^+) with slope v. 76
Figura 33 – The parameter space $C^- \times C^+$ divided into regions with different equilibria quantities and their properties. We used $S_w^+ = 0.94$. 76
Figura 34 – Intersection between $f_w(S_w, C^-)$ and the straight line that passes through point (S_w^+, f_w^+) with slope v. The value S_w^l coincides with S_w^-. The purple line passes through the point (S_w^+, f_w^+) with slope v. (a) $v = v^L$ and $S_w^l < S_w^+$. (b) $v = v^N$ and $S_w^l > S_w^+$. 76
Figura 35 – Intersection between $f_w(S_w, C^-)$ and the straight line that passes through point (S_w^+, f_w^+) with slope v. The value S_w^τ coincides with S_w^-. The purple line passes through the point (S_w^+, f_w^+) with slope v. (a) $v = v^\tau$ and $C^+ < C^-$. (b) $v = v^\tau$ and $C^+ > C^-$. 77
Figura 36 – Schematic representation showing the equilibrium points of System (5.35)-(5.37) in $\mathfrak{R}^1$. Point $P_{\mathcal{R}}$ represents a source, $P_{\mathcal{S}}$ represents a saddle, and $P_{\mathcal{A}}$ represents a sink. (a) Intersection between $f_w(S_w, C^-)$ and the straight line that passes through point (S_w^+, f_w^+) with slope v. The equilibrium points are placed on the purple solid line. (b) Equilibria in phase portrait $S_w \times C$. Functions F_1 and F_2 represent to right sides of (5.35) and (5.36). 80
Figura 37 – Solution of System (5.35)-(5.37) for $(C^-, C^+) \in \mathfrak{R}^1$ with $(S_w^-, C^-) = P_{\mathcal{R}} = (0.92722, 0.7)$, $(S_w^+, C^+) = P_{\mathcal{A}} = (0.94, 0.3)$, and $v = 0.004538 > v^\tau = 0.003397$. (a) Analytical solution in the phase portrait. The purple line represents the traveling wave shown in Figure(b). (b) Solution profile. The solid line represents the analytical solution, and the dashed line corresponds to the numerical result. 81
Figura 38 – Solution of System (5.35)-(5.37) for $(C^-, C^+) \in \mathfrak{R}^1$ with $(S_w^-, C^-) = P_{\mathcal{S}}^1 = (0.94028, 0.7)$, $(S_w^+, C^+) = P_{\mathcal{A}} = (0.94, 0.3)$, and $v = 0.004538 > v^\tau = 0.003397$. (a) Analytical solution in the phase portrait. The purple line represents the traveling wave shown in Figure(b). (b) Solution profile. The solid line represents the analytical solution, and the dashed line corresponds to the numerical result. 82

Figura 39 – Solution of System (5.35)-(5.37) for $(C^-, C^+) \in \mathfrak{R}^2$ with $(S_w^+, C^+) = P_{\mathcal{S}}^2 = (0.94, 0.7)$ and $v = 0.004538 < v^\tau = 0.003397$. (a) Analytical solution in the phase portrait. The purple line represents the traveling wave. (b) Comparison between analytical (solid line) and numerical (dashed line) solution profiles. 82
Figura 40 – Equilibria in curves of water fractional flow for C^- and C^+. The purple line passes through the point (S_w^+, f_w^+) with slope v. (a) Case $(C^-, C^+) \in \mathfrak{R}^4$. (b) Case $(C^-, C^+) \in \mathfrak{R}^5$. 83
Figura 41 – Water fractional flow for $C > C_{cmc}$ corresponding to $\mathfrak{R}^7$. The dotted lines pass through (S_w^+, f_w^+). Value S_w^T corresponds the intersection point between $f_w(S_w, C^+)$ and the tangent line to $f_w(S_w, C^+)$ that passes through (S_w^+, f_w^+). Value S_w^M corresponds the intersection between $f_w(S_w, C^+)$ and the line connecting (S_{wc}, f_{wc}) to (S_w^+, f_w^+), where $f_{wc} = f_w(S_{wc}, C^+)$. 85
Figura 42 – Solution of System (5.35)-(5.37) for $(C^-, C^+) \in \mathfrak{R}^7$ for $(S_w^+, C^+) = (0.94, 0.85)$. The solid line represents the analytical solution, and the dashed line corresponds to the numerical simulation. (a) Case $S_{wc} < S_w^- < S_w^T$ with $S_w^- = 0.2$. (b) Case $S_w^- = S_w^T$. 86
Figura 43 – Riemann problem solution of System (5.35)-(5.37) in Region $\mathfrak{R}^7$ for $(S_w^+, C^+) = (0.94, 0.85)$. The solid line represents the analytical solution, and the dashed line corresponds to the numerical simulation. (a) Case $S_w^T < S_w^- < S_w^M$ with $S_w^- = 0.5$. (b) Case $S_w^M < S_w^- < S_w^+$ with $S_w^- = 0.6$. 86
Figura 44 – Schematic phase portrait for regions $\mathfrak{L}$ and $\mathfrak{N}$. Functions F_1 and F_2 represent to right sides of (5.35) and (5.36), respectively. 87
Figura 45 – Phase portrait for $(C^-, C^+) \in \mathfrak{T}$ with $C^- > C^+$. Functions F_1 and F_2 represent to right sides of (5.35) and (5.36), respectively. The red line represents the traveling wave from $P_{\mathcal{R}}$ to $P_{\mathcal{N}}$. The green line represents the traveling wave from $P_{\mathcal{S}}^1$ to (S_w^+, C^+). 88
Figura 46 – Solution of System (5.35)(5.37) for $(C^-, C^+) \in \mathfrak{T}$ with $C^- > C^+$ for $(S_w^-, C^-) = P_{\mathcal{R}} = (0.937126, 0.7)$ and $(S_w^+, C^+) = P_{\mathcal{N}} = (0.94, 0.219605)$. The solid line represents the analytical, and the dashed line corresponds to the numerical solution. (a) Comparison between solution profiles. (b) Zoom of Figure(a) for S_w and n_D. 89
Figura 47 – Case $C^- = C^+$ with $C^- < C_{cmc}$. Value S_w^T represents the intersection point between $f_w(S_w, C^+)$ and the tangent line to $f_w(S_w, C^+)$ that passes through (S_w^+, f_w^+). In S_w^T, the type of solution changes from a sequence wave to a traveling wave. (a) Representation of all values S_w^T depending on $C^+ = C^-$. (b) Zoom of Figure(a) close to $C^+ = 0$. . . . 90

Figura R_1 – Classification of the eigenvalues of the Jacobian matrix associated to the vector field of (3.12)-(3.13) in the semi plane $[S_{wc}, 1 - S_{gr}] \times K_c$ for $A = 10$ and $S_w^+ = 0.72$. (a) As we can see, decreasing A, the size of regions **III**, **IV**, and **V** decrease in K_c and increase in S_w, when compared with the original plot in Fig. 3. (b) Zoom of the small area close to S_w^* indicated by a black rectangle in the panel (a). Notice that the pinched part of Region **III** in Region **II** remains and increases in size. (c) Zoom of the small area close to S_w^* indicated by a black rectangle in the panel (b). The relative position of regions **IV** and **V** do not change. 101

Figura R_2 – Classification of the eigenvalues of the Jacobian matrix associated to the vector field of (3.12)-(3.13) in the semi plane $[S_{wc}, 1 - S_{gr}] \times K_c$ for $A = 100$ and $S_w^+ = 0.72$. (a) As we can see, decreasing A, the size of regions **III**, **IV**, and **V** decrease in K_c and increase in S_w, when compared with the original plot in Fig. 3. (b) Zoom of the small area close to S_w^* indicated by a black rectangle in the panel (a). Notice that the pinched part of Region **III** in Region **II** remains and increases in size. (c) Zoom of the small area close to S_w^* indicated by a black rectangle in the panel (b). The relative position of regions **IV** and **V** do not change. 101

Figura R_3 – Classification of the eigenvalues of the Jacobian matrix associated to the vector field of (3.12)-(3.13) in the semi plane $[S_{wc}, 1 - S_{gr}] \times K_c$ for $A = 200$ and $S_w^+ = 0.72$. (a) As we can see, decreasing A, the size of regions **III**, **IV**, and **V** decrease in K_c and increase in S_w, when compared with the original plot in Fig. 3. (b) Zoom of the small area close to S_w^* indicated by a black rectangle in the panel (a). Notice that the pinched part of Region **III** in Region **II** remains and increases in size. (c) Zoom of the small area close to S_w^* indicated by a black rectangle in the panel (b). The relative position of regions **IV** and **V** do not change. 102

Figura R_4 – Classification of the eigenvalues of the Jacobian matrix associated to the vector field of (3.12)-(3.13) in the semi plane $[S_{wc}, 1 - S_{gr}] \times K_c$ for $A = 300$ and $S_w^+ = 0.72$. (a) As we can see, decreasing A, the size of regions **III**, **IV**, and **V** decrease in K_c and increase in S_w, when compared with the original plot in Fig. 3. (b) Zoom of the small area close to S_w^* indicated by a black rectangle in the panel (a). Notice that the pinched part of Region **III** in Region **II** remains and increases in size. (c) Zoom of the small area close to S_w^* indicated by a black rectangle in the panel (b). The relative position of regions **IV** and **V** do not change. 102

Figura R_5 – Classification of the eigenvalues of the Jacobian matrix associated to the vector field of (3.12)-(3.13) in the semi plane $[S_{wc}, 1 - S_{gr}] \times K_c$ for $A = 500$ and $S_w^+ = 0.72$. (a) As we can see, increasing A, the size of regions **III**, **IV**, and **V** increase in K_c and decrease in S_w, when compared with the original plot in Fig. 3. (b) Zoom of the small area close to S_w^* indicated by a black rectangle in the panel (a). Notice that the pinched part of Region **III** in Region **II** remains and decreases in size. (c) Zoom of the small area close to S_w^* indicated by a black rectangle in the panel (b). The relative position of regions **IV** and **V** do not change. 103

Figura R_6 – Classification of the eigenvalues of the Jacobian matrix associated to the vector field of (3.12)-(3.13) in the semi plane $[S_{wc}, 1 - S_{gr}] \times K_c$ for $A = 400$ and $S_w^+ = 0.68$. (a) As we can see, decreasing S_w, the size of regions **III**, **IV**, and **V** increase in K_c and decrease in S_w, when compared with the original plot in Fig. 3. (b) Zoom of the small area close to S_w^* indicated by a black rectangle in the panel (a). Notice that the pinched part of Region **III** in Region **II** remains and decreases in size. 104

Figura R_7 – Classification of the eigenvalues of the Jacobian matrix associated to the vector field of (3.12)-(3.13) in the semi plane $[S_{wc}, 1 - S_{gr}] \times K_c$ for $A = 400$ and $S_w^+ = 0.55$. (a) As we can see, decreasing S_w, the size of regions **III**, **IV**, and **V** increase in K_c and decrease in S_w, when compared with the original plot in Fig. 3. (b) Zoom of the small area close to S_w^* indicated by a black rectangle in the panel (a). Notice that the pinched part of Region **III** in Region **II** remains and decreases in size. 104

Figura R_8 – Classification of the eigenvalues of the Jacobian matrix associated to the vector field of (3.12)-(3.13) in the semi plane $[S_{wc}, 1 - S_{gr}] \times K_c$ for $A = 400$ and $S_w^+ = 0.47$. (a) As we can see, decreasing S_w, the size of regions **III**, **IV**, and **V** increase in K_c and decrease in S_w, when compared with the original plot in Fig. 3. (b) Zoom of the small area close to S_w^* indicated by a black rectangle in the panel (a). Notice that the pinched part of Region **III** in Region **II** remains and decreases in size. 105

LIST OF SYMBOLS

S_w	Water saturation.
n_D	Dimensionless foam texture.
n_f	Dimensional foam texture.
C	Dimensionless surfactant concentration.
C_s	Dimensional surfactant concentration.
C_{cmc}	Critical micelle concentration.
u	Total Darcy velocity.
ϕ	Porosity of the medium.
k	Permeability of the medium.
S_{wc}	Connate water saturation.
S_{gr}	Residual gas saturation.
f_w	Water fractional flow function.
λ_w	Mobility of water phase.
λ_g	Mobility of gas phase.
k_{rw}	Gas relative permeability.
k_{rg}	Water relative permeability.
n_{max}	Maximum foam texture
P_c	Capillary pressure.
μ_w	Viscosity of water.
μ_g	Viscosity of gas.

Superscripts:

"LE"	Mean the expression evaluated at conditions of local equilirium.
"$+$"	Expression is evaluated at injection conditions (Left state).
"$-$"	Expression is evaluated at reservoir conditions (Right state).

CONTENTS

1	**INTRODUCTION**	**20**
2	**MATHEMATICAL MODELING**	**23**
2.1	FOAM FLOW IN POROUS MEDIA	23
2.2	FOAM FLOW MODELS	26
2.3	CONSERVATION LAWS	28
2.3.1	**Shock waves and Hugoniot Locus**	30
2.3.2	**Rarefaction waves**	32
2.4	BALANCE EQUATION	33
2.5	THE METHOD OF CHARACTERISTICS AND TRAVELING WAVE	33
3	**MATHEMATICAL PROPERTIES OF THE FOAM FLOW IN POROUS MEDIA**	**36**
3.1	MATHEMATICAL FOUNDATIONS AND THE PHYSICAL MODEL	37
3.1.1	**The model**	37
3.2	EQUILIBRIUM STATES	40
3.3	CLASSIFICATION OF SOLUTIONS	41
3.3.1	**Region I**	43
3.3.2	**Region II**	43
3.3.3	**Region III**	44
3.3.4	**Region VI**	44
3.3.4.1	The curve $\mathcal{C}$	46
3.3.5	**Region IV**	48
3.3.6	**Region V**	49
3.4	PARTIAL CONCLUSIONS	49
4	**ANALYTICAL SOLUTION FOR THE POPULATION-BALANCE MODEL DESCRIBING FOAM DISPLACEMENT**	**52**
4.1	THE SIMPLIFIED MODEL	52
4.2	TRAVELING WAVE SOLUTION	54
4.2.1	**Classification of equilibria**	56
4.2.2	**Region** I	57
4.2.3	**Boundary between regions** I **and** II	59
4.2.4	**Region** II	59
4.3	APPROACH VALIDATION	60
4.3.1	**Experiment description**	61

4.3.2 **Experimental validation** . . . 62
4.3.3 **Numerical validation for different values of n_{max}** . . . 64
4.3.4 **Numerical validation for different values of K_g** . . . 65
4.4 PARTIAL CONCLUSIONS . . . 66

5 FOAM FLOW IN POROUS MEDIA FOR LOW SURFACTANT CONCENTRATION . . . 68
5.1 MATHEMATICAL FOUNDATIONS AND THE PHYSICAL MODEL . 68
5.1.1 **Equilibrium foam texture as function of surfactant concentration** 70
5.2 DIMESIONLESS DIFFERENTIAL EQUATIONS . . . 70
5.3 TRAVELING WAVE FORMULATION . . . 72
5.3.1 **Equilibria of system of ordinary differential equation** . . . 75
5.4 EXISTENCE OF TRAVELING WAVE CONNECTION . . . 79
5.4.1 **Region $\mathfrak{R}^1$** ($C^- > C^+$ & $v > v^\tau$): . . . 79
5.4.1.1 Case (S_w^-, C^-) is $P_{\mathcal{R}}$. . . . 79
5.4.1.2 Case (S_w^-, C^-) is $P_{\mathcal{S}}^1$. . . . 80
5.4.2 **Region $\mathfrak{R}^2$** ($C^- > C^+$ & $v < v^\tau$): . . . 81
5.4.2.1 Case (S_w^-, C^-) is $P_{\mathcal{R}}$ . . . 81
5.4.2.2 Case (S_w^-, C^-) is $P_{\mathcal{S}}^1$ . . . 82
5.4.3 **Region $\mathfrak{R}^3$** ($C^- < C^+$ & $v < v^L$): . . . 83
5.4.4 **Region $\mathfrak{R}^4$** ($C^- < C^+$ & $v^L < v < v^\tau$) : . . . 83
5.4.5 **Region $\mathfrak{R}^5$** ($C^- < C^+$ & $v^\tau < v < v^N$): . . . 84
5.4.6 **Region $\mathfrak{R}^6$** ($C^- < C^+$ & $v^N < v$): . . . 84
5.4.6.1 Case (S_w^-, C^-) is $P_{\mathcal{S}}^2$ . . . 84
5.4.6.2 Case (S_w^-, C^-) is $P_{\mathcal{A}}$ . . . 84
5.4.7 **Region $\mathfrak{R}^7$** ($C^- \geq C_{cmc}$ & $C^+ \geq C_{cmc}$): . . . 84
5.4.7.1 Case $-vS_w^+ + f_w^+ = 0$ . . . 84
5.4.7.2 Case $C^- = C^+$ . . . 84
5.4.8 **Curve $\mathfrak{L}$** ($v = v^L$): . . . 87
5.4.9 **Curve $\mathfrak{N}$** ($v = v^N$): . . . 87
5.4.10 **Curve $\mathfrak{T}$** ($v = v^\tau$): . . . 88
5.4.10.1 Case $C^- > C^+$ . . . 88
5.4.10.2 Case $C^- \leq C^+$ . . . 89
5.4.11 **Curve $\mathfrak{D}$** ($C^- = C^+ < C_{cmc}$): . . . 89
5.5 PARTIAL CONCLUSIONS . . . 89

6 CONCLUSIONS AND DISCUSSIONS . . . 91
6.1 ACADEMIC CONTRIBUTIONS . . . 92

REFERENCES . . . 94

APPENDIX A – Variation in parameter A 101
A.1 Maintaining $S_w^+ = 0.72$. and considering $A = 10$. 101
A.2 Maintaining $S_w^+ = 0.72$. and considering $A = 100$. 101
A.3 Maintaining $S_w^+ = 0.72$. and considering $A = 200$. 102
A.4 Maintaining $S_w^+ = 0.72$. and considering $A = 300$. 102
A.5 Maintaining $S_w^+ = 0.72$. and considering $A = 500$. 103

APPENDIX B – Variation in parameter S_w^+ 104
B.1 Maintaining $A = 400$ and considering $S_w^+ = 0.68$. 104
B.2 Maintaining $A = 400$ and considering $S_w^+ = 0.55$. 104
B.3 Maintaining $A = 400$ and considering $S_w^+ = 0.47$. 105

1 INTRODUCTION

Oil Recovery is commonly based on the continuous injection of an auxiliary fluid through the injection well, displacing oil from the reservoir towards the production well. This technique reaches its breaking point of efficiency when the injected fluid arrives at the production well. Various Enhanced Oil Recovery (EOR) techniques aim to improve reservoir oil production compared to conventional techniques. Enhanced Oil Recovery is defined as oil recovery by injecting materials not normally present in the reservoir. The definition of EOR intends to exclude all pressure maintenance processes, but it is not restricted to a specific phase (primary, secondary, or tertiary) in the reservoir's production life. Primary recovery is oil recovery by natural drive mechanisms. Secondary recovery refers to techniques, such as gas or water injection, whose purpose is mainly to raise or maintain reservoir pressure. Tertiary recovery is any technique applied after secondary recovery [6, 49].

Although the gas injection technique is very effective, it has poor sweep efficiency leaving a significant amount of oil in the reservoir. Gravity override and viscous instability are among the main mechanisms responsible for poor oil recovery by gas injection. These phenomena are related to gas density and viscosity. Gravity override refers to the phenomenon in which gas injected into the reservoir tends to migrate toward the upper part of the reservoir due to its low density compared to that of oil. Since, the viscosity of gas is inherently lower than that of most reservoir oils, the mobility of the injected gas is much higher than that of the displaced oil. Because of this unfavorable mobility ratio, gas tends to flow through the more permeable rock sections, and the displacement front is subject to instability when injected gas displaces oil from a reservoir. Front instability and gravity override lead to viscous fingering, see [68].

Alternating water and gas (WAG) injection is one option to avoid this loss of efficiency. This method is one of several EOR techniques that seek to reduce the mobility of the injected fluid and thus have a better oil recovery from the porous medium. Although this method increases oil recovery, it can also be hindered by effects such as viscous fingering formation, gravity override, and reservoir heterogeneities (see [35, 77]). There is a way to increase recovery enhancement further. An alternative is diluting surfactant in the aqueous phase so that the flow inside the porous medium generates foam by reducing gas mobility considerably, consequently improving recovery efficiency. This strategy is known as foam injection. Foam injection addresses all three causes of poor sweep efficiency mentioned above, [67].

Figure 1 presents a schematic diagram showing the effects of gas injection with and without foam in the porous medium.

In porous media, foam is a dispersion of the gas phase inside a liquid phase, where

the liquid (containing surfactant) remains as a continuous phase creating a discontinuity of the gas phase by thin liquid films called *lamellae* [36].

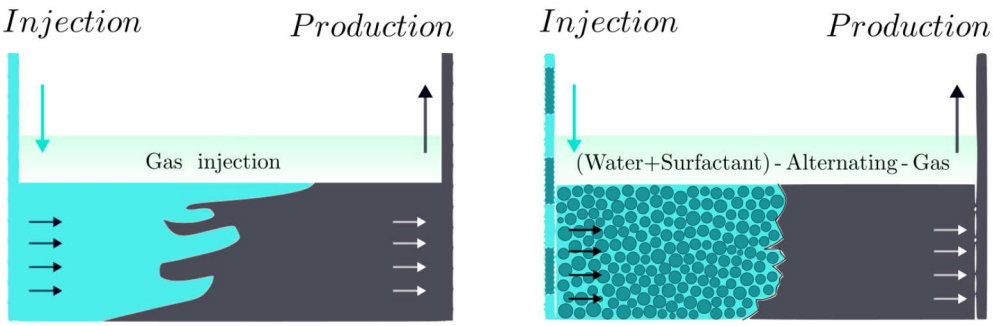

Figura 1 – Schematic diagram showing the effects of injection gas with and without foam.

Much research in foam flow through porous media has broadly increased due to its applications in the complex processes such as oil recovery [67] and soil remediation [38, 86]. The non-Newtonian properties of flow and its dependence on foam generation and coalescence turn the development of physical models of foam flow in porous media into a challenge.

Several models have been developed for a better understanding of the features of foam flow in porous media [3, 44, 48, 80, 94]. In the literature, there are substantial experimental and numerical studies of this topic [3, 37, 44, 47, 48, 74, 80, 94]. However, there are few works addressing the foam flow from the mathematical point of view [3, 46, 56, 69, 78]. It can be explained by the topic's novelty and the equations' complexity.

A promising classification of models for foam displacement in porous media is based on the variable describing the foam texture (bubble density) [57, 91]. Models can be empiric (called equilibrium models) and mechanistic (based on bubble population balance); see [35] for more details.

Empiric foam models consider that the foam texture is defined through certain empirical relations depending on an equilibrium between foam generation and destruction/coalescence. These models are less complex and more numerically stable [45]. However, a model that assumes that the foam immediately attains local steady-state as the strong foam is clearly inadequate in cases where strong foam generation is in doubt [45]. The empiric model with water and gas was investigated using the method of characteristics in the context of hyperbolic differential equations in [46]. The empiric foam model with water, gas, and oil phases was investigated using Conservation Laws Theory in [78]. The authors used *n-dimensional Riemann Problem* (RPn), a computer-assisted design package, to describe all Riemann problems' possible solutions as a sequence of shocks and rarefactions; see [78] for details.

Mechanistic foam models consider foam texture as an independent variable and have a specific differential equation to describe it. These models have successfully matched several laboratory experiments [8, 31, 48, 74]. Developing a predictive foam simulator requires a foam model tracking the change in foam texture, which results from dynamic mechanisms of in-situ *lamellae* creation and coalescence [44]. From a mathematical point of view, mechanistic models describe foam generation and coalescence as a source term depending linearly on the kinetic parameter [31, 45, 48, 74, 94].

Several experimental investigations point to saturation and foam texture profiles similar to traveling waves [40, 41, 47, 48, 73, 74]. Ashoori and coauthors deal with the foam displacement model, searching for the mathematical solution in the form of traveling waves [2, 3].

This work aims to provide analytical solutions for systems that model foam injection. We present numerical solutions and experimental data to validate analytical solutions.

The remainder of this thesis is organized as follows: Chapter 2 shows some fundamental concepts and statements necessary of the foam flow in porous media and the mathematical models used in this thesis. Chapter 3 presents the mathematical study of a linear kinetic model called by First-Order-Kinetic model describing foam displacement in porous media. For this study, we consider the large initial reservoir water saturation and all possibilities of injection saturation. We observed that the model contains some structural instabilities; and that the solution for one of the obtained cases presented localized decay in relative gas mobility. Chapter 4 presents the study of the existence and behavior of traveling wave solutions to a simplified version of the Stochastic Bubble Population model. The analytical solutions obtained are validated with experimental data and the complete model's numerical solutions. Chapter 5 introduces a foam population balance model with a separate balance equation for the surfactant concentration in the aqueous phase. We consider that the Mobility Reduction Factor depends on the surfactant concentration. We analyze the traveling wave solutions for this model. Finally, In Chapter 6, the discussions and main contributions of this thesis are presented.

2 MATHEMATICAL MODELING

In this chapter, we describe some fundamental concepts for understanding the modeling of foam displacement in a porous medium. Also, we review foam flow models used in this thesis. For more details, see [1, 7, 49, 66].

2.1 FOAM FLOW IN POROUS MEDIA

The modeling of two-phase flow in a porous medium needs some general concepts:

Porous media: In petroleum reservoir engineering, a naturally occurring porous medium is a geological formation below the ground surface, composed of a sedimentary rock called the solid matrix and a void connected space occupied by one or more fluid phases.

Porosity: As the sediments were deposited and the rocks were formed during past geological times, some developed void spaces became isolated from the other void spaces by excessive cementation. Thus, many void spaces are interconnected, while some pore spaces are completely isolated. This fact leads to two distinct types of porosity: Absolute porosity and Effective porosity. The absolute porosity is defined as the ratio of the total pore space in the rock and the bulk volume. The effective porosity is the percentage of interconnected pore space concerning the bulk volume.

The effective porosity ϕ of the medium is the ratio of the interconnected pore volume to the total volume (bulk volume):

$$\phi = \frac{Pore\ volume}{Bulk\ volume}. \tag{2.1}$$

Homogeneous/Heterogeneous media: In natural formations the medium properties change within location in the reservoir (heterogeneous media). In this thesis, we consider a simplified case, when the formation properties do not change with location (homogeneous media). This hypothesis is common in the literature and agrees with some laboratory experiments.

Fluid saturation: A fluid comprises one (single-phase fluid) or many phases (multi-phase fluid). *Phase* is a portion of a substance that is chemically uniform, physically distinct, and (often) mechanically separable. It is common for three phases to coincide, dividing the pore space, such as water, oil, and gas. However, we considered a two-phase (water and gas) fluid to facilitate (support) the analytical study made in this thesis. *The saturation of phase* α can be defined as

$$Saturation\ of\ phase\ \alpha = \frac{Pore\ volume\ occupied\ by\ the\ phase\ \alpha}{Pore\ volume}. \tag{2.2}$$

A medium is saturated if the sum of the saturations of all phases in the system must be unity.

Capillary pressure: In a petroleum reservoir, the capillary forces result from the combined effect of the surface and interfacial tensions of the rock and fluids, the pore size and geometry, and the wetting characteristics of the system. Any curved surface between two immiscible fluids tends to contract into the smallest possible area per unit volume. This is true whether the fluids are oil and water, water and gas (*e.g.,* air), or oil and gas. When two immiscible fluids are in contact, a discontinuity in pressure exists between both fluids, which depends on the curvature of the interface separating the fluids. This pressure difference is called the capillary pressure and is denoted by P_c. A fluid displacement, during the multi-phase flow, is affected by the capillary pressure's surface forces in co-flow or counter-flow directions. Denoting the pressure in the wetting fluid by p_w and that in the nonwetting fluid by p_{nw}, the capillary pressure can be expressed as $P_c = p_{nw} - p_w$. Brooks-Corey and Van Genuchten models describe the capillary pressure as the function of saturation [11, 24, 79, 83].

Permeability: The permeability is a property of a porous medium that characterizes the ability of a porous medium to allow fluid flow; it increases with both porosity and pore size. In fact, the equation which defines permeability k in terms of the flow rate, pressure gradient, and fluid viscosity is called *Darcy's law* given below by Eq. (2.4). In a multi-phase flow, *the effective permeability* k_α *of phase* α is the phase α's ability to flow in the medium in the presence of other phases. These can be expressed as fractions of the single-phase permeability k. The sum of effective permeabilities is not unity. *The relative permeability* $k_{r\alpha}$ *of* α is the ratio between the effective and absolute permeabilities:

$$k_{r\alpha} = k_\alpha / k. \tag{2.3}$$

There are a variety of empirical and theoretical models of water and gas relative permeabilities in the literature, [11, 24, 29, 53, 83].

Darcy's law: Henry Darcy experimentally formulated a relation for predicting flow in porous media, which will later be named in his honor as Darcy's law, [25]. Darcy's law describes the hydrodynamic behavior of a single-phase flow in a porous medium. Darcy also introduced the concept of permeability. Considering a homogeneous medium and disregarding gravitational effects, Darcy's Law is as follows [23]:

$$u = -\frac{k}{\mu} \nabla p, \tag{2.4}$$

where u is the Darcy velocity, p is the pressure to which the fluid is subjected, k is the permeability of the medium, and μ is the viscosity—a measure of a fluid's ability to resist flow—of the fluid.

The Darcy velocity (or superficial velocity), u, is defined as the effective rate of mass displacement in the porous medium. The actual fluid velocity (or interstitial velocity), v, occurs only within the pores because that is where the fluid actually moves. By adopting

the continuum hypothesis, we assume that the fluid moves through the entire volume of the medium with velocity u. The two velocities are related as follows

$$u = \phi v. \tag{2.5}$$

In this thesis, we assume two phase flow (water and gas), which is described by the extension of Darcy's Law to multi-phase flows (often called Darcy's multi-phase Law, or just Darcy's Law [23]):

$$u_\alpha = -\frac{k_\alpha}{\mu_\alpha}\nabla p_\alpha, \tag{2.6}$$

where the subscript α indicate the given expression corresponds to phase $\alpha \in \{w, g\}$ for water or gas, respectivly. u_α is the Darcy velocity, p_α is pressure, k_α is the permeability, and μ_α is the viscosity. Darcy's velocity of phase α is the portion of the interstitial velocity of phase α corresponding to the volume fraction that the α phase occupies in the porous medium, *i.e.*:

$$u_\alpha = \phi S_\alpha v_\alpha, \tag{2.7}$$

where ϕ is the porosity of medium and S_α is the saturation of phase α.

Steady-state flow: The *steady-state flow* is characterized by invariance with the time of all physical variables. *Isotropic medium* is a medium whose properties are the same in all directions. *Incompressible fluid* is a fluid whose density remains constant for isothermal pressure changes. For a unidimensional horizontal two phase flow of a homogeneous incompressible fluid through an isotropic porous medium, the combination of Darcy's law and the equation of continuity yields the following equation

$$\frac{\partial u_\alpha}{\partial x} = \frac{\partial}{\partial x}\left(-\frac{k_\alpha}{\mu_\alpha}\frac{\partial p_\alpha}{\partial x}\right) = 0 \quad \text{and} \qquad \frac{\partial p_\alpha}{\partial x} = constant. \tag{2.8}$$

Here, the fluid viscosity and permeability are considered constant.

Mobility: We define the mobility of phase α (its capacity to move inside the medium), λ_α, relative mobility, $\lambda_{r\alpha}$, and total mobility, λ_t, as follows

$$\lambda_\alpha = k\, k_\alpha/\mu_\alpha, \quad \lambda_{r\alpha} = k\, k_{r\alpha}/\mu_\alpha, \quad \text{and} \qquad \lambda_t = \sum_\alpha \lambda_\alpha, \tag{2.9}$$

where k_α and $k_{r\alpha}$ are given in (2.3).

Foam texture: In general, foams with more bubbles, and consequently more *lamellae*, are the ones that most reduce the mobility of the gas. Therefore, some foam structures are more efficient than others. Foams with many *lamellae* are called strong foam, while the presence of few *lamellae* characterizes a weak foam. The foam texture (n_f) is then defined to quantify the number of *lamellae* or bubbles present per unit area or volume.

Surfactant in enhanced oil recovery: The concept of oil recovery by surfactant flooding dates back to 1929 when De Groot was granted a patent claiming water-soluble surfactants

as an aid to EOR. Surfactants are molecules with a hydrophilic structure at one end and hydrophobic one at the other. These molecules could reduce the interfacial tension between the brine and residual oil. Using proper surfactant can effectively lower the interfacial tension resulting in a corresponding increase in the capillary number and facilitating the formation of stable *lamellae*. The success of surfactant flooding depends on many factors such as formulation, cost of surfactants, availability of chemicals, and oil prices in the market. The solution's superficial tension drops as the surfactant concentration increases due to the deposition of these molecules on the aqueous surface. However, when the surface is saturated with the surfactant, the molecules agglomerate inside the liquid in spherical conformations called micellae. The point at which this occurs is called the Critical Micelle Concentration (CMC). Therefore, any surfactant concentration above the CMC does not present a significant change in surface tension.

Fractional flow: The development of the fractional flow equation is attributed to Leverett (1941). For two immiscible fluids, water and gas, the fractional flow of water, f_w (or any immiscible displacing fluid), is defined as:

$$f_w = \frac{\lambda_w}{\lambda_t} = \frac{\lambda_w}{\lambda_w + \lambda_g}, \tag{2.10}$$

where λ_t is total mobility.

Newtonian/non-Newtonian flow: The viscosity of a *non-Newtonian fluid* varies in response to the duration and magnitude of the applied shear rate. A *Newtonian fluid* is an idealized fluid such that its viscosity only varies in response to changes in temperature or pressure. In this thesis, we consider the foam as a Newtonian fluid.

2.2 FOAM FLOW MODELS

The foam's displacement dynamics can be described using mass balance and bubble-population balance equations, which can be handled similarly.

If adsorption and chemical reactions are neglected, the phases are incompressible, and the flow is one-dimensional with fixed injection rates; mass balance for fluid flow in porous media becomes the following equation

$$\frac{\partial}{\partial t}(\phi S_\alpha) + \frac{\partial}{\partial x}(u_\alpha) = 0, \qquad \alpha = w \text{ or } g. \tag{2.11}$$

If capillary pressure is taken into account, the velocity of phase α is written depending on capillary pressure. For example, the water velocity is given by

$$u_w = u f_w + f_w \lambda_g \nabla P_c. \tag{2.12}$$

The foam displacement in a porous medium can be modeled by the following equations: the conservation of the mass for the water phase (Rapoport-Leas equation) and

a so-called population-balance equation for foam texture:

$$\frac{\partial}{\partial t}(\phi S_w) + \frac{\partial}{\partial x}\left(u f_w + f_w \lambda_g \frac{dP_c}{dS_w}\frac{\partial S_w}{\partial x}\right) = 0, \tag{2.13}$$

$$\frac{\partial}{\partial t}(\phi S_g\, n_D) + \frac{\partial}{\partial x}(u_g\, n_D) = \Phi, \tag{2.14}$$

where $n_D = n_f/n_{max}$ is the dimensionless foam texture, where n_{max} is the maximum foam texture and n_f is the dimensional foam texture.

The several foam displacement models proposed over the years are focused on the gas relative permeability k_{rg}, water relative permeability k_{rw}, the modification of the gas mobility λ_g, and mainly the net foam generation term Φ, that actively models the dynamic of foam generation and coalescence.

First-Order-Kinetic (FOK) model: This foam model, proposed by [2, 3], is based on the well-known steady-state foam behavior in porous media. It considers a large, nearly constant, reduction in gas mobility at high water saturation and an abrupt weakening or collapse of foam at a limiting capillary pressure (or, equivalently, at a limiting water saturation). Foam texture in local-equilibrium (n_D^{LE}) depends on the water saturation (S_w):

$$n_D^{LE}(S_w) = \begin{cases} \tanh(A\,(S_w - S_w^*)) & \text{if } \; S_w > S_w^*, \\ 0 & \text{if } \; S_w \leq S_w^*, \end{cases} \tag{2.15}$$

with constant A. The dynamic foam net generation in (2.14) is given by the first-order approach to local-equilibrium bubble texture at any saturation, with a time constant $1/K_c$, as follows

$$\Phi = \frac{\phi}{n_{max}} S_g\,[r_g - r_c], \qquad [r_g - r_c] = K_c\, n_{max}\,(n_D^{LE}(S_w) - n_D), \tag{2.16}$$

where r_g and r_c are the generation and coalescence functions, respectively. n_{max} is the maximum foam texture (reflecting a lower limit to bubble size), see [2, 3, 45].

In this model, the viscosity is considered constant (*i.e.,* the fluid is Newtonian) the gas mobility reduction modifies the gas relative permeability k_{rg} as follows:

$$k_{rg}(S_w, n_D) = \frac{k_{rg}^0(S_w)}{MRF(n_D)} = \frac{k_{rg}^0(S_w)}{18500\, n_D + 1}. \tag{2.17}$$

where k_{rg}^0 gas relative permeability in the absence of foam. The large Mobility Reduction Factor (MRF) is assumed as 18500 for the strongest foam and MRF as 1 for no foam. MRF is interpolates as a linear function of foam texture between those two foam extremes, see [2, 3, 93]:

Stochastic Bubble Population (SBP) model: The model proposed by Zitha and Du in [94] is based on foam rheology and stochastic bubble generation ideas. Inspired by [2, 3],

we seek the mobility reduction factor (MRF) as a linear function and the viscosity constant, thus obtaining Newtonian flow. So we correlate the gas phase mobility expressions for both models: FOK [3] and SBP model [37, 94]. One contribution of this thesis is investigate the Newtonian version of SBP model.

Here, the modification of gas mobility is accomplished in terms of the foam rheology theory. The net bubble generation is expressed as

$$\Phi = \phi S_g[K_g(1 - n_D) - K_d n_D], \tag{2.18}$$

or, equivalently,

$$\Phi = \phi\, S_g\, (K_g + K_d)(n_D^{LE} - n_D), \qquad n_D^{LE} = \frac{K_g}{K_d + K_g}, \tag{2.19}$$

where K_g and K_d are the bubble generation and bubble destruction rate coefficients, respectively.

Therefore, this model simplifies foam description in porous media without significantly sacrificing the physics. The SBP model does not contain any arbitrary terms relative to trapped gas. This model contains only three parameters (K_g, K_d, and n_{max}). In fact, since bubble and pore volumes are approximately equal near the steady-state, a rough estimate of n_{max} is the number of pores occupied by gas, *i.e.*, $n_{max} \approx S_g\phi/r^3$, where r is the mean pore radius. Hence, we are left with only two parameters to be determined by fitting the solution of the bubble population's evolution to experimental data.

2.3 CONSERVATION LAWS

A conservation law states that when there is no production or consumption, the variation of a quantity conserved in a fixed domain is equal to the inflow minus the outflow in the domain, see [27, 65]. Let $\Omega \subset \mathbb{R}$ be in a fixed region of space through which the fluid flows; Ω is called the control volume. Applied to this control volume, the fundamental physical principle that mass is conserved means that

$$\begin{pmatrix} \textit{Total mass transfer rate out of the control} \\ \textit{volume across its boundary} \end{pmatrix} = \begin{pmatrix} \textit{Rate of change of mass} \\ \textit{within the control volume} \end{pmatrix}$$

where the vector function $S : \Sigma \subset \mathbb{R} \times \mathbb{R}_+ \to \mathbb{R}^n$ represents the quantities to be conserved, such as mass, moment, and energy; $q = F(S)$ denotes the density of the mass flow (or the mass flow); and the function $F : \mathbb{R}^n \to \mathbb{R}^n$ is called a flow function, where each of its components represents the flow of the associated quantity [65]. The conservation law of mass can be expressed mathematically in integral form:

$$-\int_{\partial\Omega} q(x,t)dS = \frac{d}{dt}\int_{\Omega} S(x,t)dV, \tag{2.20}$$

Therefore, the mathematical expression for the conservation law of mass in a fixed control volume Ω is the integral equation

$$\frac{d}{dt}\int_{\Omega} S + \int_{\partial\Omega} F(S) = 0. \tag{2.21}$$

The divergence theorem allows to obtain a differential equation from this integral equation. Substituting this expression into the mass conservation law, and passing the derivation operator inside the integral

$$\int_{\Omega}\left[\frac{\partial S}{\partial t} + \operatorname{div}(F(S))\right] = 0. \tag{2.22}$$

Since the conservation law of mass is valid for any arbitrary Ω control volume, the conservation law can be expressed mathematically as the partial differential equation of evolution (2.11) or (2.13) that briefly we write as

$$S_t + (F(S))_x = 0. \tag{2.23}$$

Following [65, 82], we consider the Eq. (2.23) as a *strictly hyperbolic equation*, that is, each matrix $F'(S)$ has distinct eigenvalues $\lambda_1(S) < \cdots < \lambda_n(S)$, thus there exists a base of $\mathbb{R}^n$ composed of eigenvectors $\{r_k(S)\}_{k=1}^n$, where each pair $(\lambda_k(S), r_k(S))$ is an eigenpair for $F'(S)$. The system's eigenvalues and eigenvectors are called *characteristic velocities* and *characteristic vectors* of the system, respectively. The term *"k-family"*, $1 \leq k \leq n$, refers to the k-th eigenpair.

A problem involving conservation laws generally has initial conditions and, when the spatial domain is limited, boundary conditions. *Cauchy Problem* is a classic type of Initial Value Problem (IVP) in which

$$S(x,0) = S_0(x), \qquad -\infty < x < \infty. \tag{2.24}$$

In this case, S_0 is the initial condition for the solution S of the problem. A particular case of the Cauchy problem widely used in the theory of conservation laws and the development of numerical methods is the so-called *Riemann Problem*, in which the initial condition is of the form

$$S_0(x) = \begin{cases} S^- & \text{if } x < 0, \\ S^+ & \text{if } x > 0, \end{cases} \tag{2.25}$$

where the constant vectors S^- and S^+ are the left and right states, respectively.

As [65], for the IVP (2.23)-(2.25) we define *characteristic curve of the k-family* as the parameterized curve $(x(t), t)$ that satisfies the following

$$x'(t) = \lambda_k(S(x(t),t)), \quad t > 0, \tag{2.26}$$

$$x(0) = x_0, \tag{2.27}$$

for some x_0.

A differentiable solution that satisfy the Eq. (2.23) is called *strong (classic) solution.* A generalized solution can be admitted for cases where it is impossible to obtain a robust solution.

Following [65], we say that S is a *weak (generalized) solution* of the conservation law (2.23) and (2.25), if

$$\int_0^\infty \int_{-\infty}^\infty [S\,\phi_t + F(S)\,\phi_x]dxdt + \int_{-\infty}^\infty S_0(x)\,\phi(x,0)dx = 0, \tag{2.28}$$

for all $\phi \in C^\infty(\mathbb{R} \times [0,\infty))$ with compact support.

Generally, the weak solution to a conservation law problem is not unique; using additional criteria is necessary to find a physically relevant solution.

One way to find a physically relevant solution is to add a small diffusion in the conservation law (2.23), which results in the so-called *viscous form*

$$S_t^\epsilon + (F(S^\epsilon))_x = \epsilon\, S_{xx}^\epsilon, \tag{2.29}$$

where ϵ is a positive constant. Thus, the Eq. (2.23) will be called *inviscid equation.* In some cases, it is possible to verify the uniqueness of the viscous profile solution. Then, uniqueness can be extended to the inviscid form through the limit

$$S = \lim_{\epsilon \to 0} S^\epsilon. \tag{2.30}$$

Finding the solution S^ϵ is not simple; the other method to find a unique solution for the inviscid equation is using the so-called entropy conditions, explained below.

2.3.1 Shock waves and Hugoniot Locus

The solution of Riemann problem (2.23) and (2.25) consisting only of a shock is given by

$$S(x,t) = \begin{cases} S^- & \text{if } x < s\,t, \\ S^+ & \text{if } x > s\,t, \end{cases} \tag{2.31}$$

where s satisfies the following proposition.

Proposition 2.3.1. *A discontinuity between S^- and S^+ in a solution of the Riemann problem of a conservation law must satisfy the condition*

$$F(S^+) - F(S^-) = s\,(S^+ - S^-), \tag{2.32}$$

for some velocity s. This condition is known as Rankine-Hugoniot condition.

The demonstration of this proposition can be found in [65, 75].

Let $\hat{S}$ be a fixed state (left or right), the set of states $\tilde{S}$ that can be connected to $\hat{S}$ through a discontinuity (that is, $\hat{S}$ and $\tilde{S}$ satisfy Eq. (2.32) for some s) is called the *Hugoniot Locus* for the state $\hat{S}$. This problem results in a system with n equations and $n+1$ unknowns since the velocity s is unknown. For F smooth enough, it has been proved in [52, 75] that the solution set is a family of n curves branches containing $\hat{S}$. These branches accept differentiable settings, and the function s on them is also differentiable. The analysis that follows considers this particular case.

Let $\tilde{S}_k$ be a parameterization of one of the n-branches of points that satisfy the Eq. (2.32) such that $\tilde{S}_k(0) = \hat{S}$. If $s_k(\xi)$ is the velocity function for each point in this branch, the Rankine-Hugoniot condition becomes

$$F(\tilde{S}_k(\xi)) - F(\hat{S}) = s_k(\xi)\,(\tilde{S}_k(\xi) - \hat{S}). \tag{2.33}$$

Assuming $\tilde{S}_k$ and s_k to depend smoothly on ξ, we find after differentiating

$$F'(\tilde{S}_k(\xi))\tilde{S}'_k(\xi) = s'_k(\xi)\,(\tilde{S}_k(\xi) - \hat{S}) + s_k(\xi)\,\tilde{S}'_k(\xi). \tag{2.34}$$

When evaluating the derivative of the above expression at the point $\xi = 0$, we obtain

$$F'(\hat{S})(\tilde{S}'_k(0)) = s_k(0)\,\tilde{S}'_k(0), \tag{2.35}$$

such that the eigenvector $r_k(\hat{S})$ is tangent to the curve branch parameterized by $\tilde{S}_k$ in $\xi = 0$, where this branch is associated with the k-family. In addition, $s_k(0) = \lambda_k(\hat{S})$.

The state $\tilde{S}$ is in the Hugoniot locus of $\hat{S}$ if the discontinuity satisfies the Rankine-Hugoniot condition, regardless of whether this discontinuity could exist in an inviscid solution. We now define an entropy condition that can be applied directly to a discontinuous weak solution to determine whether the discontinuity should be allowed. The following definition is necessary to present the entropy conditions proposed in [52].

Definition 2.3.1. The k-th field of characteristic eigenvalues is said *genuinely non-linear* [75], if

$$\nabla\lambda_k(S)\,r_k(S) \neq 0, \qquad \forall S. \tag{2.36}$$

In other words, a field λ_k is genuinely non-linear if the λ_k function is monotonous, increasing or decreasing over any integral curve of the vector field r_k.

Definition 2.3.2 (Lax entropy conditions [65])**.** If the k-th field of characteristic eigenvalues is genuinely non-linear Lax's entropy condition says that a discontinuity between S^- and S^+ is admissible only if

$$\lambda_k(S^-) > s > \lambda_k(S^+), \tag{2.37}$$

where s is the velocity of discontinuity.

2.3.2 Rarefaction waves

The solution of Riemann problem (2.23) and (2.25) consisting only of a rarefaction wave is given by

$$S(x,t) = \begin{cases} S^- & \text{if } x \leq \xi_1\, t, \\ G(x/t) & \text{if } \xi_1\, t < x < \xi_2\, t, \quad x \in \mathbb{R},\ t > 0, \\ S^+ & \text{if } x \geq \xi_2\, t, \end{cases} \tag{2.38}$$

for some pair (ξ_1, ξ_2) such that $\xi_1 < \xi_2$ (here, $S^- = G(\xi_1)$, $S^+ = G(\xi_2)$, $\xi_1 = \lambda_k(S^-)$, and $\xi_2 = \lambda_k(S^+)$, see [65] for details). The function G characterizes the wave and must be determined for each type of equation, The function G is determined by the function F given in Equation (2.23).

An *integral curve* of r_k for a single k-family is a curve which has the property that the tangent to the curve at any point S lies in the direction $r_k(S)$. If $S_k(\xi)$ is a parameterization (for $\xi \in \mathbb{R}$) of an integral curve in the k-th family, then the tangent vector is proportional to $r_k(S_k(\xi))$ at each point, *i.e.*

$$S_k'(\xi) = \alpha(\xi) r_k(S_k(\xi)), \tag{2.39}$$

where $\alpha(\xi)$ is some scalar factor, see [82] for more details.

We suppose F is smooth enough for the following calculations. By deriving G, given by (2.38), in time and space and replacing the result in the conservation law (2.23), we obtain

$$-\frac{x}{t^2} G'(x/t) + \frac{1}{t} F'(G(x/t))\, G'(x/t) = 0. \tag{2.40}$$

Rearranging the terms and denoting $\xi = x/t$, we obtain

$$F'(G(\xi))\, G'(\xi) = \xi\, G'(\xi). \tag{2.41}$$

Since the function G is expected to be smooth and connect the two states S^- and S^+, it is assumed that $G'(\xi) \neq 0$, that is, $G'(\xi)$ is proportional to some eigenvector $G'(\xi)$. Since the eigenvectors are linearly independent, $G'(\xi)$ must be proportional to only one of the n eigenvectors, so that $G(\xi)$ lies on the integral curve of r_k for a single k-family.

A rarefaction wave between two states S^- and S^+ is obtained in the same integral curve of the k-family, whether ξ be monotonously increasing between the states. Note that the relation

$$\xi = \lambda_k(G(\xi)) \tag{2.42}$$

is valid, so that the monotonicity of λ_k over the integral curve is equivalent to the monotonicity of the parameter ξ. For cases with genuine non-linearity of the k-field of eigenvalues, $G(\xi)$ is a parameterization of the respective integral curve of the eigenvector r_k and for this type of wave, the characteristic curves are

$$\lambda_k(S^-) < \lambda_k(S^+). \tag{2.43}$$

The details of calculating the expression $G(\xi)$ are shown in [65, 75, 82].

2.4 BALANCE EQUATION

There is a possibility that mass is created or destroyed through some internal or external source (*e.g.,* through chemical reactions or nuclear processes, among others). In this case, the physical principle of conservation of mass needs to be rewritten as follows [9]

$$\begin{pmatrix} \textit{Total mass transfer rate out} \\ \textit{of the control volume} \\ \textit{across its boundary} \end{pmatrix} + \begin{pmatrix} \textit{Rate of mass creation} \\ \textit{or destruction within} \\ \textit{the control volume} \end{pmatrix} = \begin{pmatrix} \textit{Rate of change} \\ \textit{of mass within} \\ \textit{the control volume} \end{pmatrix}$$

Let $\Omega \subset \mathbb{R}$ be a region of space fixed through which the fluid flows; Ω is called a control volume, ρ is the density of the fluid and q is the density of the mass flow. If $F(x,t)$ is the rate of mass creation or destruction (the rate has a negative sign if mass destruction occurs), the conservation law of mass becomes

$$\frac{d}{dt}\int_{\Omega} \rho(x,t)dV + \int_{\partial\Omega} q(x,t)\cdot \overrightarrow{n}\, dS = \int_{\Omega} F(x,t)dV, \tag{2.44}$$

and the corresponding differential equation, through the divergence theorem, is given by

$$\int_{\Omega} \frac{d}{dt}\rho(x,t)dV + \int_{\Omega} \operatorname{div}(q(x,t))dS = \int_{\Omega} F(x,t)dV, \tag{2.45}$$

Since the control volume Ω is arbitrary, the **balance equation** is obtained

$$\frac{\partial \rho}{\partial t} + \operatorname{div}(q) = F. \tag{2.46}$$

The balance equations are formulated at the microscopic level from classical continuum mechanics for each phase of the porous medium and are then transformed to the macroscopic level.

Notice that the foam displacement model studied mathematically in this thesis and presented in Section 2.2 is composed by a conservation law (2.13) and a balance equation (2.14).

2.5 THE METHOD OF CHARACTERISTICS AND TRAVELING WAVE

The method of characteristics allows us to solve partial differential equations (PDEs) as a system of ordinary differential equations (ODEs) along certain curves in the xt plane. Buckley and Leverett solved the Riemann problem (explained below) for two-phase flow using the method of characteristics [13]. They gave rise to an ingenious graphical construction, discovered independently by Oleĭnik for general scalar conservation laws [61]. In the context of Buckley-Leverett theory, the foam flow is composed of constant states (where the one on the extreme left corresponds to injection conditions and the one on the

extreme right to the native reservoir) separated by rarefaction waves and shock waves, where:

- **Rarefaction (spreading) waves** are continuous solutions, which are invariant under the scaling $x \to ax, t \to at$ for any $a > 0$.
- **Shock (discontinues) waves** are solutions corresponding to discontinuities in the saturation along a fractional-flow curve. There are two rules for shocks. Firstly, there are algebraic conditions derived from material balances on components involved in displacement (Rankine-Hugoniot conditions [75]). Secondly, the shock-front profile must approximate a valid traveling wave solution for the same boundary conditions (left and right constant states).
- **Traveling waves** are solutions characterized geometrically as a wave that moves with a constant velocity maintaining the profile, as shown in Figure 2. These solutions only depend on the *traveling variable* $\xi = x - vt$, which means that the original system of PDEs is transformed into a system of ODEs. Traveling wave solutions appear in nonlinear transport problems involving balance equations [84] and others physical problems, [16, 18, 33, 84]. Note that the traveling wave not associated with any shock wave can exist, precisely the foam flow case examined in this thesis.

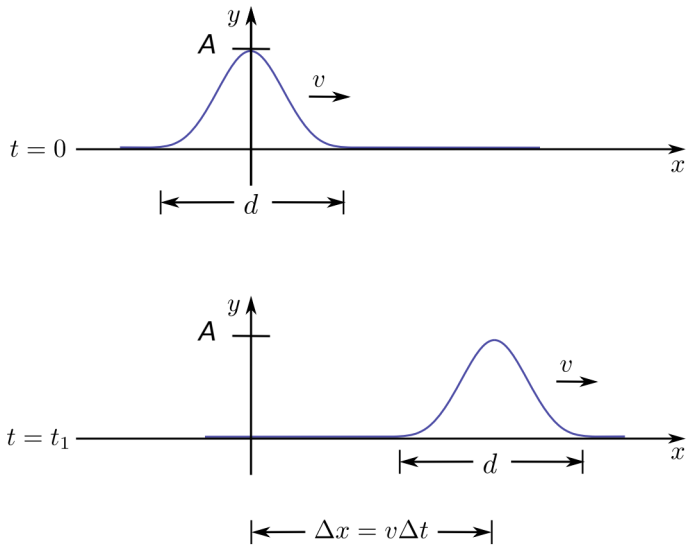

Figura 2 – Schematic representation of a traveling wave that moves with a constant velocity v.

Definition 2.5.1 (Traveling wave solution)**.** A solution $S_w(x,t)$, $n_D(x,t)$ of System (2.13)-(2.14) is a **traveling wave** connecting the left state $(S_w^-, n_D^-) \in \mathbb{R}^2$, and the right state $(S_w^+, n_D^+) \in \mathbb{R}^2$, if there exists a velocity $v \in \mathbb{R}$ and functions $\widetilde{S}_w(\xi)$ and $\widetilde{n}_D(\xi)$ such that

$$S_w(x,t) = \widetilde{S}_w(\xi), \quad n_D(x,t) = \widetilde{n}_D(\xi), \quad \xi = x - vt, \tag{2.47}$$

$$\lim_{\xi \to \pm\infty} \widetilde{S}_w(\xi) = S_w^{\pm}, \quad \lim_{\xi \to \pm\infty} \widetilde{n}_D(\xi) = n_D^{\pm}. \tag{2.48}$$

Definition 2.5.2. A bounded traveling wave solution that is monotonic, but not constant, and such that

$$\lim_{\xi\to\pm\infty}(\widetilde{S}_w(\xi),\widetilde{n}_D(\xi)) = (S_w^{\pm}, n_D^{\pm}), \quad (S_w^-, n_D^-) \neq (S_w^+, n_D^+). \tag{2.49}$$

for some S_w^-, n_D^-, S_w^+, $n_D^+ \in [0,\infty)$ are equilibrium points of the reaction term, is said to be a *wavefront* solution from (S_w^-, n_D^-) to (S_w^+, n_D^+).

One standard procedure to find traveling wave solutions consists in analyzing the phase space [76]. In the context of foam dynamics, it was used by Ashoori and colleagues [2, 3, 4]. We can summarize this procedure as follows. (1) Rewrite the system of PDEs in traveling wave form $w' = g(w)$, where w represents the vector (S_w, n_D) and prime represents the derivative in ξ. (2) Locate all equilibria in the system ($g(w_0) = 0$) and classify them according to the sign of the eigenvalues of the Jacobian of the flux at the equilibrium ($Jg(w_0)$); (3) Show the ODE solutions (also called connection [84]) that approach both equilibria asymptotically.

Equilibrium points appearing in this thesis are classified according to their eigenvalues as follows. For other types of equilibria and corresponding classification, see [34, 76].

- An equilibrium with two real positive eigenvalues is called a source;
- An equilibrium with two real negative eigenvalues is called a sink;
- An equilibrium with two real eigenvalues of different signs is called a saddle point;
- An equilibrium with two complex conjugate eigenvalues is called a sink or source (spiral) point depending on whether the sign of the real part of the eigenvalues is positive or negative;
- An equilibrium with one zero and other nonzero eigenvalues is called a node.

The method for locating connections used in this thesis is performed computationally and is based on the initial conditions' smart choice, for more details, see [3, 19]. This method works well when there are no null eigenvalues, which is the case in this text. Notice that building a connection between two equilibria asymptotically is not always possible. Considering connections with direction from the left state (α-limit) to the right state (ω-limit), there is no connection in the following cases: (1) right equilibrium is a source, (2) left equilibrium is a sink, or (3) left equilibrium is a complex sink.

3 MATHEMATICAL PROPERTIES OF THE FOAM FLOW IN POROUS MEDIA

This chapter is a reprint of work published in Computational Geosciences, 2021 by Springer, [56]. DOI: 10.1007/s10596-020-10020-3.

In the current chapter, we use the model presented by Ashoori *et al.*, [2], where the kinetic parameter is K_c. One form determining the kinetic parameter is analyzing the length of the entrance region (more specifically, the length it takes to form a foam in equilibrium) [45], which can be narrow [2] making it challenging to estimate K_c correctly. The kinetic parameters can also be estimated in laboratory experiments focusing on the transient foam flow in a homogeneous porous medium containing a surfactant solution; see [74], where it was done for a simpler model. One of the present chapter goals is to show how small changes of the kinetic parameter can influence mathematical solutions of the foam flow models and, consequently, impact numerical simulations.

We follow the approach used in [2, 3] and considered the apparent gas viscosity, proposed in [37, 59], independent of gas velocity to investigate a traveling wave solution of the same simple mechanistic foam displacement model. Although this simplification essentially transforms foam displacement into a Newtonian flow, it showed good agreement with experiments and allowed a mathematically accurate analysis. Also, we obtained the complete classifications of all possible traveling wave solutions and Riemann problems. In this sense, the current chapter generalizes one presented in [3], since [3] only obtained the solution for three points in the foam generation/coalescence kinetic parameter space $S_w^- \times K_c$.

The presented classification allowed us to find two types of structural instabilities that need to be considered in numerical simulations of the foam flow in a porous medium. One of them can influence the numerical solutions by introducing oscillations. The other one is responsible for the abrupt decay in the total relative mobility close to the critical pressure point. Such behavior was already observed in the simulations described in the literature [30, 68, 72, 81].

This chapter is organized as follows. In Section 3.1, we introduce the mathematical and physical concepts used in the analysis, describes the foam displacement model and summarizes the main results found in the literature [2, 3]. In Section 3.2, we begin the investigation of the model by analyzing the critical points of the vector field associated to the system of ordinary differential equations that describes the traveling waves. In Section 3.3, we classify the equilibria found in the previous section. In Section 3.4, the main results are presented and discussed together with final remarks.

3.1 MATHEMATICAL FOUNDATIONS AND THE PHYSICAL MODEL

The model is based on the fractional-flow theory used to describe the immiscible flooding since the '40s (see [13]) with several applications for EOR techniques [49, 64, 85], among others. In the context of foam displacements, the fractional-flow theory was first applied by Zhou *et al.*, [92]. The following standard assumptions are considered in this chapter: 1D horizontal flow, incompressibility of all phases, immediate attainment of local steady-state mobilities, Newtonian mobilities, absence of dispersion, absence of viscous fingering, and small capillary pressure gradients. The water fractional flux function f_w is given by [13], as defined in Section 2.1. Remembering

$$f_w = \frac{\lambda_w}{\lambda_w + \lambda_g}, \quad \lambda_w = \frac{k\, k_{rw}}{\mu_w}, \quad \text{and} \quad \lambda_g = \frac{k\, k_{rg}}{\mu_g}, \tag{3.1}$$

where λ_w and λ_g are the mobility of water and gas phases, respectively. k denotes the permeability of the medium, relative permeabilities of water and gas phases are denoted by k_{rw} and k_{rg}, while corresponding viscosities are given by μ_w and μ_g. The porous medium is considered to be fully saturated, *i.e.*, $S_w + S_g = 1$, where S_w and S_g are water and gas saturations. In the foam displacement context λ_g and f_w depend on the foam texture or the bubble size n_f, defined as the number of *lamellae* per unit volume of gas-phase [3].

The fractional flow theory describes the physics of the displacements in porous media in terms of hyperbolic partial differential equations, which can be solved analytically by the method of characteristics (also known as Conservation Law Theory).

3.1.1 **The model**

As this chapter relies on existing models, we will summarize the results found in the works [2, 3]. In this chapter, we study the System (2.13)-(2.14) with (2.16) and use the parameter values given in [2, 3] and summarized in Table 1.

Tabela 1 – Parameter values for the foam displacement in porous medium [2].

Symbol	Parameter	Value & unit
S_{wc}[-]	Connate water saturation	0.2
S_{gr}[-]	Residual gas saturation	0.18
μ_w [Pa s]	Water viscosity	$1 \cdot 10^{-3}$
μ_g^0[Pa s]	Gas viscosity in absence of foam	$2 \cdot 10^{-5}$
k [m^2]	Permeability of the medium	$1 \cdot 10^{-12}$
ϕ[-]	Porosity of the medium	0.25
u[m s^{-1}]	Total superficial velocity	$2.93 \cdot 10^{-5}$
n_{max} [m^{-3}]	Maximum foam texture	$8 \cdot 10^{13}$
S_w^*[-]	Critical water saturation	0.37
A[-]	Foam parameter in the model	400

The population-balance model for foam displacement in a porous medium is described by the water mass balance (Rapoport-Leas equation) and the foam texture:

$$\frac{\partial}{\partial t}(\phi S_w) + \frac{\partial}{\partial x}\left(u f_w + \ f_w \lambda_g \frac{dP_c}{dS_w}\frac{\partial S_w}{\partial x}\right) = 0, \tag{3.2}$$

$$\frac{\partial}{\partial t}(\phi S_g\, n_D) + \frac{\partial}{\partial x}(u_g\, n_D) = \Phi, \tag{3.3}$$

where ϕ is the porosity, u is the superficial velocity of the mixture (water+gas), P_c is the capillary pressure, u_g is the superficial velocity of the gas phase, n_f is the dimensional foam texture, n_D is the dimensionless foam texture $n_D = n_f/n_{max}$, where n_{max} is the maximum foam texture. The foam generation source term Φ, inspired by a linear kinetic model [94], is written as

$$\Phi = \frac{\phi}{n_{max}} S_g[r_g - r_c] = \phi\, K_c\, (1 - S_w)\, (n_D^{LE}(S_w) - n_D), \tag{3.4}$$

where r_g and r_c are the generation and coalescence functions, K_c is a constant representing the foam creation rate. The term n_D^{LE} is the Local-Equilibrium (dimensionless) foam texture, which is given by

$$n_D^{LE}(S_w) = \begin{cases} \tanh(A(S_w - S_w^*)) & \text{if } \ S_w > S_w^*, \\ 0 & \text{if } \ S_w \leq S_w^*, \end{cases} \tag{3.5}$$

where A is a constant and S_w^* is the critical water saturation (at which foam collapses). The gas Mobility Reduction Factor (MRF) [2, 3] due to the presence of foam is a simplified version of the apparent viscosity considering constant gas velocity

$$MRF(n_D) = 18500\, n_D + 1. \tag{3.6}$$

The relative permeabilities [2, 3] are

$$k_{rg} = \frac{k_{rg}^0(S_w)}{MRF(n_D)}, \tag{3.7}$$

$$k_{rg}^0(S_w) = \begin{cases} 0.94 & \text{if } \ 0 \leq S_w < S_{wc}, \\ 0.94\left(\dfrac{1 - S_w - S_{gr}}{1 - S_{wc} - S_{gr}}\right)^{1.3} & \text{if } \ S_{wc} \leq S_w < 1 - S_{gr}, \\ 0 & \text{if } \ 1 - S_{gr} \leq S_w \leq 1, \end{cases} \tag{3.8}$$

and

$$k_{rw}(S_w) = \begin{cases} 0 & \text{if } \ 0 \leq S_w \leq S_{wc}, \\ 0.2\left(\dfrac{S_w - S_{wc}}{1 - S_{wc} - S_{gr}}\right)^{4.2} & \text{if } \ S_{wc} < S_w \leq 1 - S_{gr}, \\ 0.2 & \text{if } \ 1 - S_{gr} < S_w \leq 1, \end{cases} \tag{3.9}$$

where S_{wc} is the connate water saturation and S_{gr} is the residual gas saturation. The capillary pressure is given by

$$P_c = 15,000 \times \frac{0.022\,(1 - S_w - S_{gg})^c}{(S_w - S_{wc})}, \quad c = 0.01. \tag{3.10}$$

The factor $(1-S_{wc}-S_{gr})^c$ with very small c guarantees a continuous function at residual gas saturation, while hardly affecting capillary-pressure values at the other water saturation, see [3].

The system of PDEs (3.2)-(3.3) was solved as a Riemann problem, *i.e.*, a problem with the initial conditions in the form of a step function:

$$S_w(x,0) = \begin{cases} S_w^- & \text{if } x < 0, \\ S_w^+ & \text{if } x > 0, \end{cases} \qquad \text{and} \qquad n_D(x,0) = \begin{cases} n_D^- & \text{if } x < 0, \\ n_D^+ & \text{if } x > 0. \end{cases} \tag{3.11}$$

The superscripts "+" and "−" mean the given expression is evaluated at conditions downstream and upstream of the wave (right and left states), where $n_D^- = n_D^{LE}(S_w^-)$ and $n_D^+ = n_D^{LE}(S_w^+)$.

A traveling wave solution of System (3.2)-(3.3) is defined as in Section 2.5.

By abuse of notation, the tildes are dropped from now on. Considering $v_s = v\phi/u$ and substituting the expressions (2.47)-(2.48) into (3.2)-(3.3) results in the following system of ODEs describing the variation of water saturation and foam texture within the traveling wave:

$$\frac{dS_w}{d\xi} = \frac{u[f_w - v_s S_w - (f_w - v_s S_w)^+]}{-f_w \lambda_g \frac{dP_c}{dS_w}}, \tag{3.12}$$

$$\frac{dn_D}{d\xi} = \frac{\phi\, K_c\, (1 - S_w)\, (n_D^{LE}(S_w) - n_D)}{n_{max}\, u\, (1 - f_w^+ - v_s(1 - S_w^+))}. \tag{3.13}$$

In this chapter, we are interested in solutions associated to the vector field of (3.12)-(3.13) connecting the left state to the right state yielding the existence of the traveling wave solution of System (3.2)-(3.3). We call such a solution by the traveling wave connection from the left state to the right state. In this chapter, we do not deal with connections in the opposite direction.

Ashoori and colleagues derive the equations describing the traveling waves approaching shock waves during a foam displacement without the simplification of foam equilibrium [3]. Besides, the capillary-pressure gradients were also considered. The authors investigated the solution structure for the boundary conditions[1] $(S_w^-, n_D^-) = (0.372, 0.664)$ and $(S_w^+, n_D^+) = (0.72, 1.0)$ for three values of the kinetic parameter: $K_c = 200$, $K_c = 1$ and $K_c = 0.01$.

For the cases $K_c = 200$ and $K_c = 0.01$, using the parameter values in Table 1, the left and the right states were classified as a source and as a saddle, respectively.

[1] Mathematically, $n_D^{LE} \neq 1$ for any value of S_w. However, for $S_w > 0.415$ the distance from 1 is below the machine precision. We follow [3] and abuse the notation $n_D^{LE}(0.72) = 1$.

These cases are represented in the parameter plane $S_w^- \times K_c$ in Figure 4 with the points $A = (0.372, 200)$ and $C = (0.372, 0.01)$. For the case $K_c = 1$, the left state was classified as a spiral source (complex eigenvalue with positive real part), the right state was classified as a saddle. They show that the foam dynamics within the traveling wave lead to oscillations and stressed that these are not numerical artifacts, but reflections of the model. This case is represented in the parameter plane $S_w^- \times K_c$ in Figure 4(b) with the point $B = (0.372, 1)$. In all cases, there is a valid traveling wave solution.

Notice that the complete analysis of the parameter space $S_w^- \times K_c$ was not performed. Although it leads to some new results, as shown in the present chapter.

3.2 EQUILIBRIUM STATES

The focus of the present chapter consists in classifying all traveling wave solutions for System (3.12)-(3.13). Traveling wave solution always connects equilibria in the sense of ODEs, see [84]. Thus, in order to do the classification, we fix states (S_w^-, n_D^-) and (S_w^+, n_D^+), and study the singularities of the vector field associated to the right side of System (3.12)-(3.13), *i.e.,* all states (S_w, n_D), such that

$$\frac{\partial S_w}{\partial \xi} = 0, \quad \frac{\partial n_D}{\partial \xi} = 0, \quad \text{where} \quad v_s = \frac{f_w^+ - f_w^-}{S_w^+ - S_w^-} \tag{3.14}$$

is the Rankine-Hugoniot jump condition [75], which coincides with the traveling wave velocity in this case. Substituting (3.14) into (3.12)-(3.13) yields

$$\frac{u[f_w - v_s S_w - (f_w - v_s S_w)^+]}{-f_w \lambda_g \frac{dP_c}{dS_w}} = 0, \tag{3.15}$$

$$\frac{\phi(1 - S_w)\,(r_g - r_c)}{n_{max}\, u\,(1 - f_w^+ - v_s(1 - S_w^+))} = 0. \tag{3.16}$$

Equation (3.16) results in $S_w = 1$ or $r_g = r_c$. For the water saturation in the interior of the definition interval ($S_{wc} < S_w < 1 - S_{gr}$), only the option $r_g = r_c$ is valid. Using Eq. (3.4) it follows that the dynamic foam texture is in local-equilibrium $n_D = n_D^{LE}(S_w)$. Therefore, Equation (3.15) is solely a function of water saturation and its denominator is not null. Then, the equilibria of the vector field associated to the System (3.12)-(3.13) are given by the solutions of

$$f_w(S_w, n_D^{LE}(S_w)) - v_s S_w - (f_w - v_s S_w)^+ = 0, \tag{3.17}$$

where (S_w^-, n_D^-) and (S_w^+, n_D^+) are the states given by (3.11). By abuse of the notation, we denoted $f_w^{LE}(S_w) = f_w(S_w, n_D^{LE}(S_w))$ henceforth. Notice that (S_w^-, n_D^-) and (S_w^+, n_D^+) also are singularities of the vector field associated to the System (3.12)-(3.13) and they do not depend on K_c. The number of equilibria can be two or three depending of the state (S_w^-, n_D^-). To see this, notice that (3.17) represents the intersection between the curve

of fractional flow function in local equilibrium (see Figure 3) and the straight line that passes through the points (S_w^-, n_D^-) and (S_w^+, n_D^+) with slope $v_s = v_s(S_w^-, S_w^+)$ defined in Eq. (3.14).

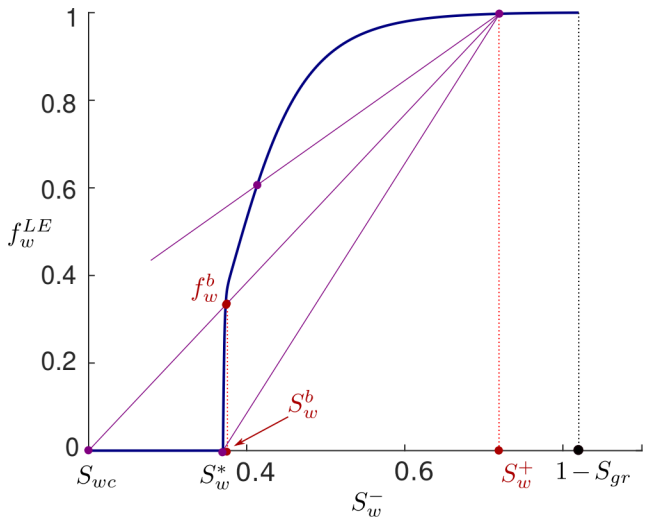

Figura 3 – Equilibria of System (3.12)-(3.13) belong to the intersection of the curve $(S_w, f_w^{LE}(S_w))$ (solid red curve) and lines passing through $(S_w^+, f_w^{LE}(S_w^+))$ with slope v_s (dashed black lines). Depending on the value of S_w^- relative to S_w^b, there are two or three equilibria.

Remark 3.2.1. Figure 3 shows the case where $S_w^+ = 0.72$. Notice that there is a point S_w^b, such that (S_w^b, f_w^b) lies on the straight line which passes through the points $(S_{wc}, 0)$ and (S_w^+, f_w^+). There are three possibilities:

- If $S_{wc} \leq S_w^- < S_w^*$, there are three equilibria S_w^-, S_w^e and S_w^+, such that $S_w^- < S_w^e < S_w^+$.
- If $S_w^* < S_w^- \leq S_w^b$, there are three equilibria S_w^-, S_w^e and S_w^+, such that $S_w^e < S_w^- < S_w^+$.
- In other cases, there are only two equilibria S_w^- and S_w^+.

3.3 CLASSIFICATION OF SOLUTIONS

In this section, we classify the solutions of System (3.2)-(3.3) with initial data (3.11) for a fixed right state S_w^+ varying the left state S_w^- and the foam kinetic rate K_c as plotted in Figure 4. This classification is based on the analysis of traveling wave solutions, which are solutions of System (3.12)-(3.13) with boundary limits (2.48). The traveling wave type is determined by eigenvalues of the Jacobian matrices associated to the vector field in (3.12)-(3.13) in neighborhoods of equilibria (S_w^-, n_D^-) and (S_w^+, n_D^+).

As the system is bidimensional, there are two eigenvalues of the Jacobian matrix. The notation used here is $\lambda_1 = \lambda_1(S_w, n_D)$ and $\lambda_2 = \lambda_2(S_w, n_D)$. When the eigenvalues are real, we assume $\lambda_1 < \lambda_2$. In the complex case the real parts are equal: $\mathrm{Re}(\lambda_1) = \mathrm{Re}(\lambda_2)$.

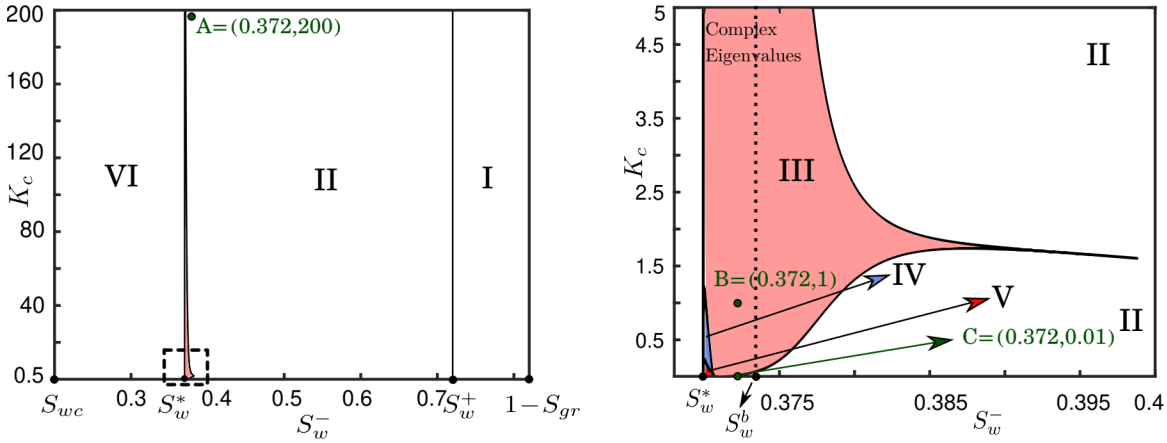

(a) (b)

Figura 4 – Classification of the eigenvalues of the Jacobian matrix associated to the vector field (3.12)-(3.13) in the semi plane $\{(S_w, K_c) : \ S_{wc} \leq S_w \leq 1 - S_{gr}, \ 0 < K_c < \infty\}$. (a) Classification of regions of S_w^- associated to $S_w^+ = 0.72$. (b) Zoom of regions close to S_w^* on a small box of Figure(a). The dotted line represents the vertical line $S_w = S_w^b$.

In what follows, the superscript $(-)$ and $(+)$ denote the eigenvalues associated with the left and the right states, respectively.

We begin considering regions **I**, **II** and **III**. As the analysis inside regions **IV** and **V** depend on the analysis of the Region **VI**, we first discuss the Region **VI** and then we continue with regions **IV** and **V**. The equilibria classification in each region are summarized in Table 2.

Tabela 2 – Classifications and type of solutions for each region showed in Figure 4.

Region	(S_w^-, n_D^-)	(S_w^+, n_D^+)	Classification of Solutions
I	Saddle	Source	Rarefaction
II	Source	Saddle	Traveling Wave
III	Complex Source	Saddle	Oscillating T. Wave
IV	Complex Sink	Saddle	Seq. of Waves (Oscillating)
V	Sink	Saddle	Seq. of Waves
VI	Saddle	Saddle	Seq. of Waves

To solve PDEs (3.1), we chose the nonlinear Crank-Nicolson implicit finite-difference scheme combined with Newton's method to perform numerical simulations, see [50] for details. This scheme is second-order accurate in space and time. To solve the system of ODEs (3.12)-(3.13), we use the routine *ode45* of MATLAB.

In each region in Figure 4(a) we analyze the existence of a traveling wave solution, and, in case there is no such, we present the construction of a Riemann problem solution.

3.3.1 Region I

Traveling wave solution. Consider the state $S_w^- > S_w^+$, with S_w^- in Region **I**, see Figure 4(a). In this case we have $\lambda_1^- < 0$, $\lambda_2^- > 0$, $\lambda_1^+ > 0$, and $\lambda_2^+ > 0$. Thus the left state is a saddle, and the right is a source. Considering that in this text, a connection possesses a direction, it follows that there is no traveling wave connection from the left state to the right state. Therefore the solution does not possess a traveling wave.

Riemann problem solution. Notice that the left and right states are in the set $f_w^{LE} \cap f_w(S_w, 1)$. As $n_D^- = n_D^+ = 1$ with fractional flux given by the function $f_w(S_w, 1)$. The resulting two phases flow is governed by the Buckley-Leverett (BL) equation, see Figure 3. Therefore the solution corresponds to a rarefaction wave with increasing characteristic velocity. Figure 5(a) shows the traveling wave connections and the equilibria in the phase space. Figure 5(b) shows the profile solution for this case.

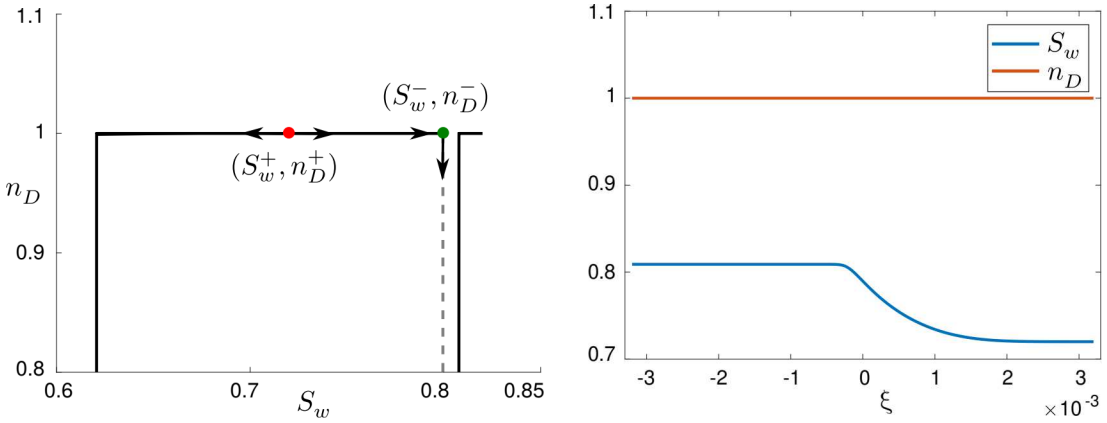

Figura 5 – Case $(S_w^+, n_D^+) = (0.72, 1)$, $K_c = 1$, and $(S_w^-, n_D^-) = (0.81, 1.0)$ corresponding to Region **I**, see Figure 4. (a) Solutions of System (3.12)-(3.13) in the phase space. There is no traveling wave connection from the left state (S_w^-, n_D^-) to right state (S_w^+, n_D^+). (b) The numerical solution of the Riemann problem (3.2)-(3.3) consists of a rarefaction wave connecting (S_w^-, n_D^-) to (S_w^+, n_D^+).

3.3.2 Region II

Traveling wave solution. Consider the state $S_w^- < S_w^+$, with S_w^- in Region **II**, see Figure 4. In this case we have $\lambda_1^- > 0$, $\lambda_2^- > 0$, $\lambda_1^+ < 0$, and $\lambda_2^+ > 0$. It means that the left state is a source and the right state is a saddle. As we see in Remark 3.2.1 there are two possibilities: $S_w^b \leq S_w^- < S_w^+$ or $S_w^- < S_w^b$. In the first case, the only equilibria are the left and right states. In the second case, we have another saddle type equilibrium (S_w^e, n_D^e), however $S_{wc} < S_w^e < S_w^*$. Thus, in Region **II** there exists a traveling wave connection from the left state to the right state, see Figure 6(a). Therefore, a solution in the form of a traveling wave is possible with solution profile plotted in Figure 6(b).

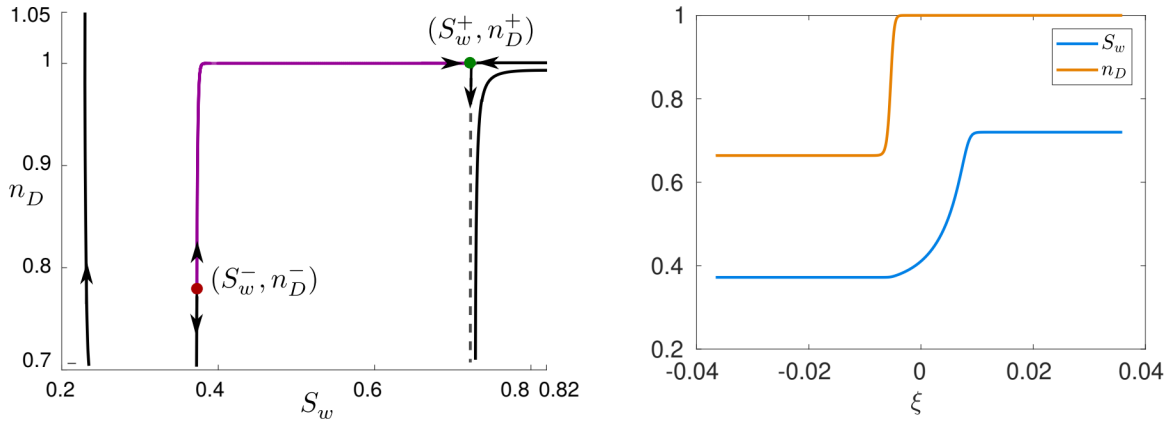

Figura 6 – Case $(S_w^+, n_D^+) = (0.72, 1)$, $K_c = 200$, and $(S_w^-, n_D^-) = (0.372, 0.664)$ corresponding to point A in Region **II**, see Figure 4(a). (a) Solutions of System (3.12)-(3.13) in the phase space. There is a the traveling wave connection from (S_w^-, n_D^-) to (S_w^+, n_D^+). (b) The numerical solution of the Riemann problem (3.2)-(3.3) consists of a traveling wave connecting (S_w^-, n_D^-) to (S_w^+, n_D^+).

3.3.3 Region III

Traveling wave solution. Consider the state $S_w^- < S_w^+$, with S_w^- in Region **III**, see Figure 4. In this case we have that λ_1^- and λ_2^- are complex conjugated with $\mathrm{Re}(\lambda_1^-) = \mathrm{Re}(\lambda_2^-) > 0$, meanwhile $\lambda_1^+ < 0$ and $\lambda_2^+ > 0$ are real. It means that the left state is a complex source, and the right state is a saddle. The traveling wave overshoots and oscillates around the left state with a decreasing amplitude as the traveling wave passes. Figure 7 highlights the oscillations around state S_w^-. As was discussed in [3] the oscillations within the traveling wave are not numerical artifacts, but reflections of the model. Notice that in Figure 4(b) there is a thin "pinched" part of Region **III** inside Region **II**. We go into more detail on this phenomenon in Section 3.4.

3.3.4 Region VI

Traveling wave solution. Consider the left state $S_w^- < S_w^+$ in the Region **VI**, which satisfies $S_{wc} \leq S_w^- \leq S_w^*$, see Figure 4. In this case $\lambda_1^- < 0$, $\lambda_2^- > 0$, $\lambda_1^+ < 0$, and $\lambda_2^+ > 0$ yielding both left and right states are saddles. As it is known in the context of dynamical systems, a connection between two saddle-points is structurally unstable, see [34]. This means that small perturbations in the parameters cause the traveling wave connection between saddles to break. One possible procedure to find these saddle-saddle connections in the context of foam displacement is described in [4].

In our case, fixing the right state $S_w^+ = 0.72$, for all K_c there is a unique S_w^-, such that $S_{wc} \leq S_w^- \leq S_w^*$, with a traveling wave connection from (S_w^-, n_D^-) to (S_w^+, n_D^+). The set of all possible states (S_w^-, K_c) form the set $\mathcal{C}$, which is a curve inside $\{(S_w, K_c) : \ S_{wc} \leq$

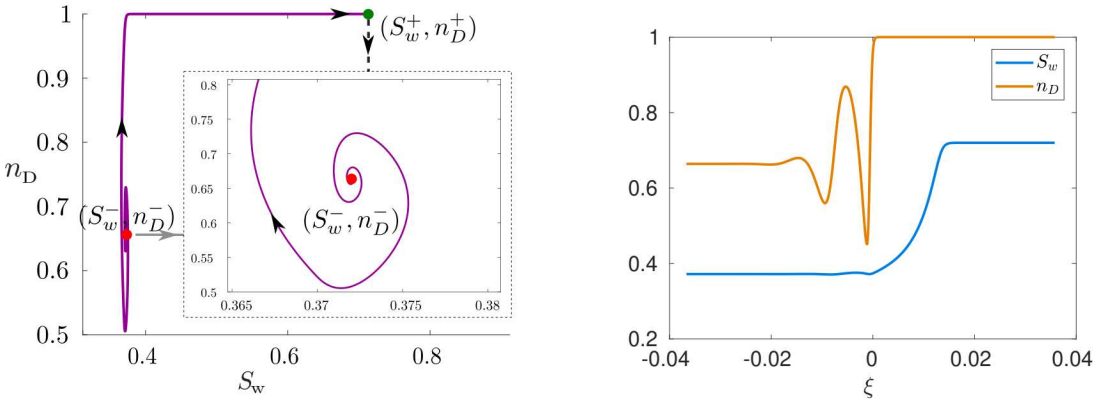

(a) (b)

Figura 7 – Case $(S_w^+, n_D^+) = (0.72, 1)$, $K_c = 1$, and $(S_w^-, n_D^-) = (0.372, 0.664)$ corresponding to point B in Region **III**, see Figure 4(b). (a) Solutions of System (3.12)-(3.13) in the phase space. There is an oscillating connection from (S_w^-, n_D^-) to (S_w^+, n_D^+). (b) The numerical solution of the Riemann problem (3.2)-(3.3) consists of an (oscillating) traveling wave connecting (S_w^-, n_D^-) to (S_w^+, n_D^+).

$S_w \leq S_w^*,\ 0 < K_c < \infty\}$, see Figure 8. Therefore, given a value of K_c, the only remaining possibility for a traveling wave solution for states $S_w^-,\ S_{wc} \leq S_w^- \leq S_w^*$, is that (S_w^-, K_c) belongs to the curve $\mathcal{C}$. For the construction of the curve $\mathcal{C}$ see Section 3.3.4.1.

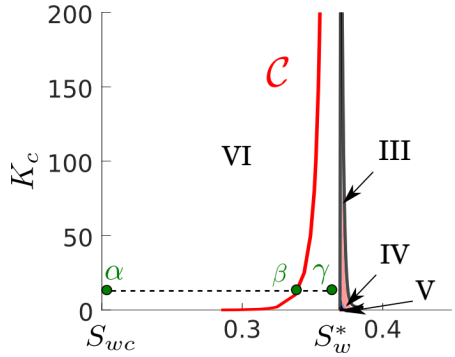

Figura 8 – Zoom on the Region **VI** from Figure 4(a) corresponding to $(S_w^+, n_D^+) = (0.72, 1)$. The curve $\mathcal{C}$ (red) is formed by points (S_w^-, K_c), such that there is a saddle-saddle connection between (S_w^-, n_D^-) and (S_w^+, n_D^+). Points α (left of $\mathcal{C}$), β (on $\mathcal{C}$) and γ (right of $\mathcal{C}$) are in Region **VI**.

Riemann problem solution. For a given left state in the Region **VI** , which satisfies $S_{wc} \leq S_w^- \leq S_w^*$, there are three possibilities for a solution of the original PDE System (3.2)-(3.3). Consider a fixed value for K_c and let $S_w^{\mathcal{C}}$ be the corresponding saturation value such that $(S_w^{\mathcal{C}}, K_c)$ is on the curve $\mathcal{C}$.

If $S_w^- < S_w^{\mathcal{C}}$, there is no possible traveling wave connection between the left and right states. There is another equilibrium (S_w^e, n_D^e) between (S_w^-, n_D^-) and (S_w^+, n_D^+),[2] which

[2] Point (S_w^e, n_D^e) stays between (S_w^-, n_D^-) and (S_w^+, n_D^+) along the curve $n_D(S_w) = n_D^{LE}(S_w)$,

is a source, and it prevents the direct connection as shown in Figure 9(a). Then, this case's solution consists of a rarefaction from (S_w^-, n_D^-) until $(S_w^{\mathcal{C}}, n_D^{\mathcal{C}})$ with increasing velocity followed by a traveling wave to (S_w^+, n_D^+). Figure 9(b) shows the solution profile for the point α plotted in Figure 8.

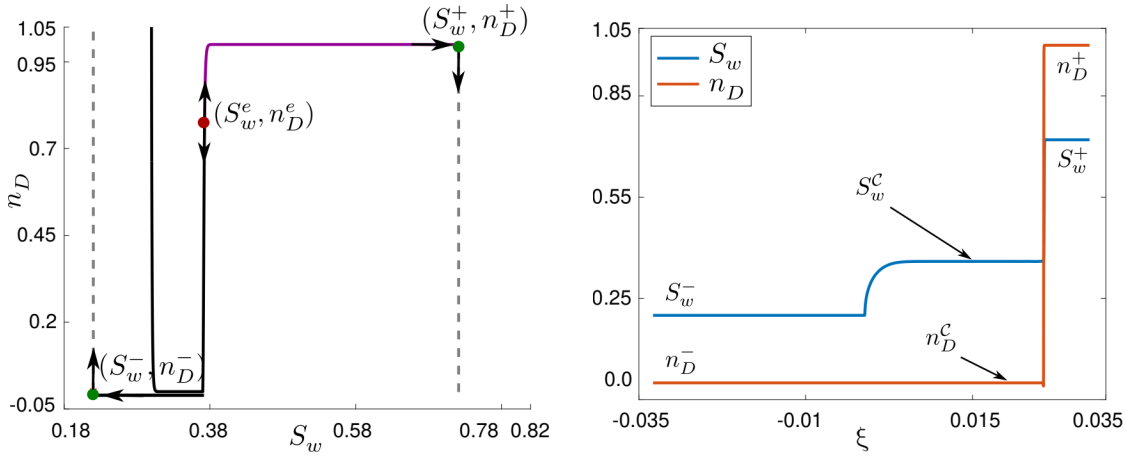

Figura 9 – Case $(S_w^+, n_D^+) = (0.72, 1)$, $K_c = 10$, and $(S_w^-, n_D^-) = (0.205, 0)$ corresponding to point α in Region **VI**, see Figure 8. (a) Solutions of System (3.12)-(3.13) in the phase space. There is no connection between (S_w^-, n_D^-) and (S_w^+, n_D^+). The point (S_w^e, n_D^e) is also an equilibrium of (3.12)-(3.13) (b) The numerical solution of the Riemann problem (3.2)-(3.3) consists of a rarefaction wave connecting (S_w^-, n_D^-) to $(S_w^{\mathcal{C}}, n_D^{\mathcal{C}})$, followed by the traveling wave to (S_w^+, n_D^+).

If $S_w^- = S_w^{\mathcal{C}}$ there is a direct saddle-saddle traveling wave connection between (S_w^-, n_D^-) and (S_w^+, n_D^+) as detailed above, see Figure 10(a) for the phase space diagram and Figure 10(b) for the profile solution. Both figures correspond to point β plotted in Figure 8.

If $S_w^- > S_w^{\mathcal{C}}$, there is no possible traveling wave connection between the left and right states. In this case there is another equilibrium (S_w^e, n_D^e) between (S_w^-, n_D^-) and (S_w^+, n_D^+), which is a source and it prevents the direct connection, see Figure 11(a). The solution of Riemann problem (3.2)-(3.3), (3.14) for this case consists of a shock from (S_w^-, n_D^-) to $(S_w^{\mathcal{C}}, n_D^{\mathcal{C}})$ followed by a traveling wave to (S_w^+, n_D^+). Figure 11(b) shows the profile solution for the point γ plotted in Figure 8.

3.3.4.1 The curve $\mathcal{C}$

The construction of the set $\mathcal{C}$ is done semi-numerically. From Remark 3.2.1, there are three equilibria in this case.

For S_w close to S_{wc}, the phase portrait is similar to one plotted in Figure 9(a). In particular the unstable manifold of (S_w^-, n_D^-) grows unbounded ($n_D \to +\infty$), while the

where all three points belong.

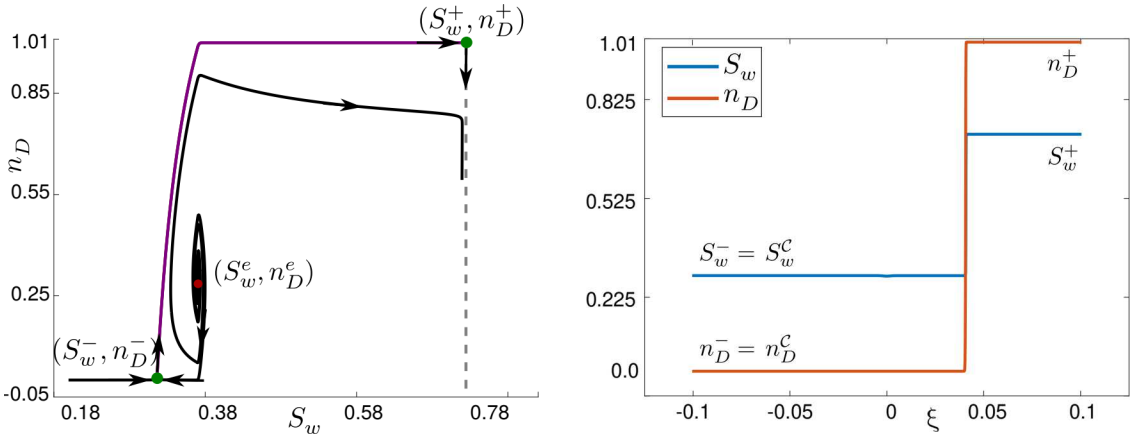

(a) (b)

Figura 10 – Case $(S_w^+, n_D^+) = (0.72, 1)$, $K_c = 10$, and $(S_w^-, n_D^-) = (0.3375, 0)$ corresponding to point β in Region **VI**, see Figure 8. (a) Solutions of System (3.12)-(3.13) in the phase space. There is a saddle-saddle connection between (S_w^-, n_D^-) and (S_w^+, n_D^+) (solid purple curve). The point (S_w^e, n_D^e) is also an equilibrium of (3.12)-(3.13). (b) The numerical solution of the Riemann problem (3.2)-(3.3) consists only of a traveling wave solution connecting (S_w^-, n_D^-) to (S_w^+, n_D^+).

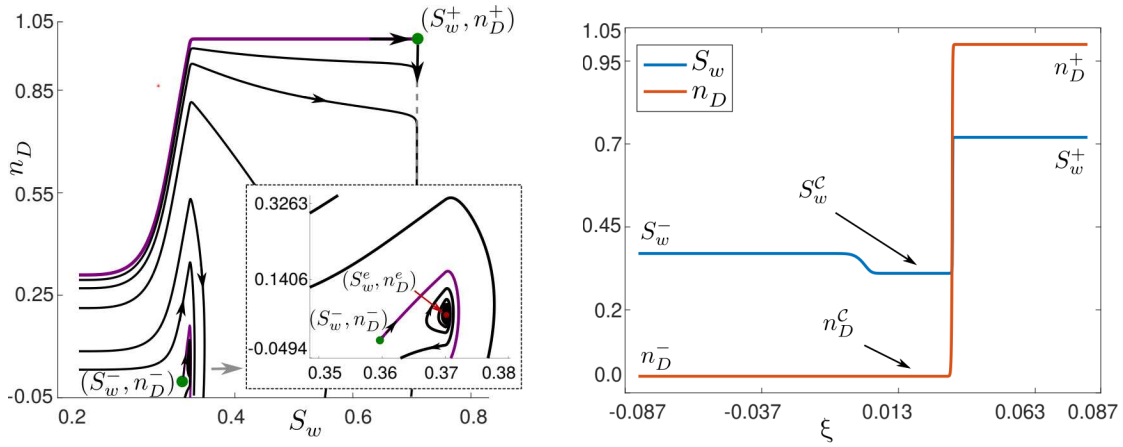

(a) (b)

Figura 11 – Case $(S_w^+, n_D^+) = (0.72, 1)$, $K_c = 10$, and $(S_w^-, n_D^-) = (0.36995, 0)$ corresponding to point γ in Region **VI**, see Figure 8. (a) Solutions of System (3.12)-(3.13) in the phase space. There is no connection between (S_w^-, n_D^-) and (S_w^+, n_D^+). The point (S_w^e, n_D^e) is also an equilibrium of (3.12)-(3.13). (b) The numerical solution of the Riemann problem (3.2)-(3.3) consists of a shock wave connecting (S_w^-, n_D^-) to $(S_w^{\mathcal{C}}, n_D^{\mathcal{C}})$ followed by the traveling wave to (S_w^+, n_D^+).

stable manifold of (S_w^+, n_D^+) decreases unbounded ($n_D \to -\infty$). Both manifolds are plotted in purple in Figure 9(a). From left to right the unstable manifold (S_w^-, n_D^-) stays over the stable manifold of (S_w^+, n_D^+).

For S_w close to S_w^*, the phase portrait is as one plotted in Figure 11(a). In particular the unstable manifold of (S_w^-, n_D^-) grows slightly and decays unbounded, while the stable manifold of (S_w^+, n_D^+) contours (S_w^-, n_D^-) decreases unbounded. Both manifolds are plotted

in purple in Figure 11(a). From left to right the unstable manifold (S_w^-, n_D^-) stays under the stable manifold of (S_w^+, n_D^+).

Although the rigorous proof of manifolds' relative positions described above stays outside of the scope of this chapter, this observation together with the Intermediate Value Theorem indicates the existence of at least one point S_w^-, where unstable manifold of (S_w^-, n_D^-) and stable manifold of (S_w^+, n_D^+) intersect. Equivalently, for such (S_w^-, n_D^-) there exists a traveling wave connection from (S_w^-, n_D^-) to (S_w^+, n_D^+). Similar proof explained in detail can be found in [19, 20, 62].

Rigorous uniqueness proof (for example, using Melnikov integral following [19, 20]), also stays outside this chapter scope. However, the bifurcation described above indicates that for each K_c there is a unique point S_w^- yielding that the set $\mathcal{C}$ is, in fact, a curve.

3.3.5 Region IV

Traveling wave solution. Consider the left state S_w^- in Region **IV**, which satisfies $S_w^* \leq S_w^- < S_w^+$, see Figure 4. In this case λ_1^- and λ_2^- are complex conjugate with $\mathrm{Re}(\lambda_1^-) = \mathrm{Re}(\lambda_2^-) < 0$, while $\lambda_1^+ < 0$ and $\lambda_2^+ > 0$ are real. It follows that the left state is a complex sink, and the right state is a saddle. Thus, there is no traveling wave connection from the left to the right state, see Figure 12(a) for the phase portrait.

Riemann problem solution. The solution of (3.2)-(3.3) in Region **IV** is similar to the case $S_w^{\mathcal{C}} < S_w^-$ in Region **VI**, in the sense that there is an oscillating wave connecting $S_w^{\mathcal{C}} < S_w^-$ to the corresponding point $(S_w^{\mathcal{C}}, K_c)$ on the curve $\mathcal{C}$ followed by the traveling wave to (S_w^+, n_D^+), see Figure 12(b).

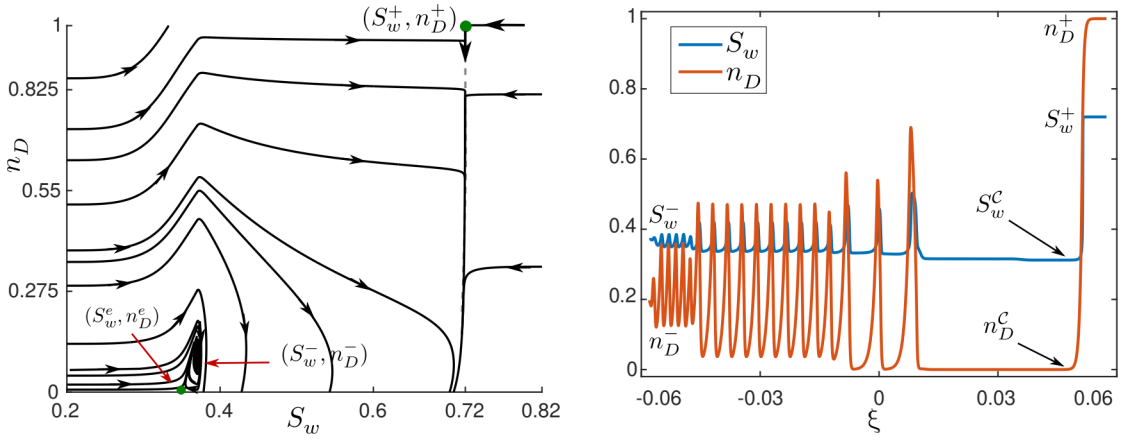

Figura 12 – Case $(S_w^+, n_D^+) = (0.72, 1)$ with $K_c = 0.5$, $A = 400$ and $(S_w^-, n_D^-) = (0.3705, 0.197375)$ corresponding to Region **IV**, see Figure 4. (a) Solution of System (3.12)-(3.13) in the phase space. There is no connection between (S_w^-, n_D^-) and (S_w^+, n_D^+). The point (S_w^e, n_D^e) is also an equilibrium of (3.12)-(3.13). (b) The numerical solution of the Riemann problem (3.2)-(3.3) consists of an oscillating wave (S_w^-, n_D^-) to $(S_w^{\mathcal{C}}, n_D^{\mathcal{C}})$ followed by a traveling wave to (S_w^+, n_D^+).

3.3.6 Region V

Traveling wave solution. For S_w^- in Region **V** the eigenvalues satisfy $\lambda_1^- < \lambda_2^- < 0$ and $\lambda_1^+ < 0$ and $\lambda_2^+ > 0$. It means that the left state is a sink and the right state is a saddle. As in Region **IV**, there is no possible traveling wave connection. The phase portrait is plotted in Figure 13(a).

Riemann problem solution. The solution of (3.2)-(3.3) for this case consists of a wave (S_w^-, n_D^-) to $(S_w^{\mathcal{C}}, n_D^{\mathcal{C}})$ followed by a traveling wave to (S_w^+, n_D^+). It is similar to one for Region **VI**, except there are no oscillations. The solution profiles are plotted in Figure 13(b).

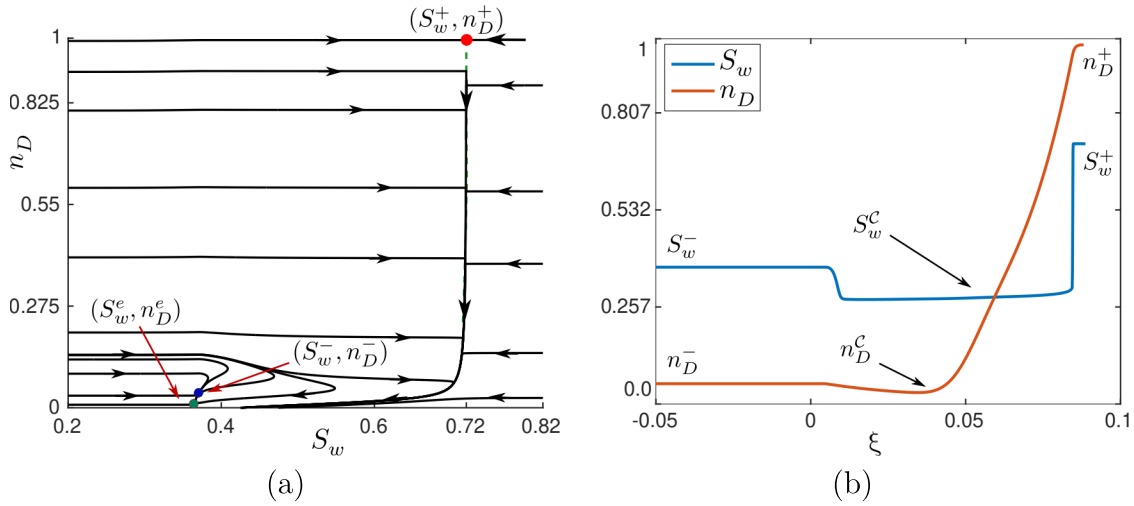

Figura 13 – Case $(S_w^+, n_D^+) = (0.72, 1)$, $K_c = 0.005$, $A = 200$ and $(S_w^-, n_D^-) = (0.3702, 0.03997867)$ corresponding to Region **V**, see Figure 4. (a) Solution of System (3.12)-(3.13) in the phase space. There is no connection between (S_w^-, n_D^-) and (S_w^+, n_D^+). The point (S_w^e, n_D^e) is also an equilibrium of (3.12)-(3.13). (b) The numerical solution of the Riemann problem (3.2)-(3.3) consists of a wave (S_w^-, n_D^-) to $(S_w^{\mathcal{C}}, n_D^{\mathcal{C}})$ followed by a traveling wave to (S_w^+, n_D^+).

3.4 PARTIAL CONCLUSIONS

The presented classification of solutions possesses a potential for practical applications in investigating the foam flow in porous media. The classification obtained in this chapter and shown in Figure 4 is similar for different values of parameter A and S_w^+. These results are presented in appendices A and B. The immediate result from this classification consists of the presence of two types of instabilities presented next. As far as we know, neither of them was observed in laboratory experiments, indicating this type of model's limitations.

The first one is connected to the value of K_c and is due to the "pinched" part of Region **III** inside Region **II** as depicted in Figure 14(a). Notice that the parameter K_c is a parameter that can not be precisely measured. A small variation (error) in the choice of

this parameter, see points *1), 2)* and *3)* in Figure 14(a) results in qualitatively different solutions as shown in Figure 14(b) and (c). Still, we can take parameters in the boundary between Regions **II** and **III**, the complex source of Region **III** and the source of Regions **II** collapse obtaining the left state as an unstable proper node, see [63]. Notice that the amplitude of oscillations in Figure 14(c) are very small. However this can significantly influence numerical methods used to simulate this type of model.

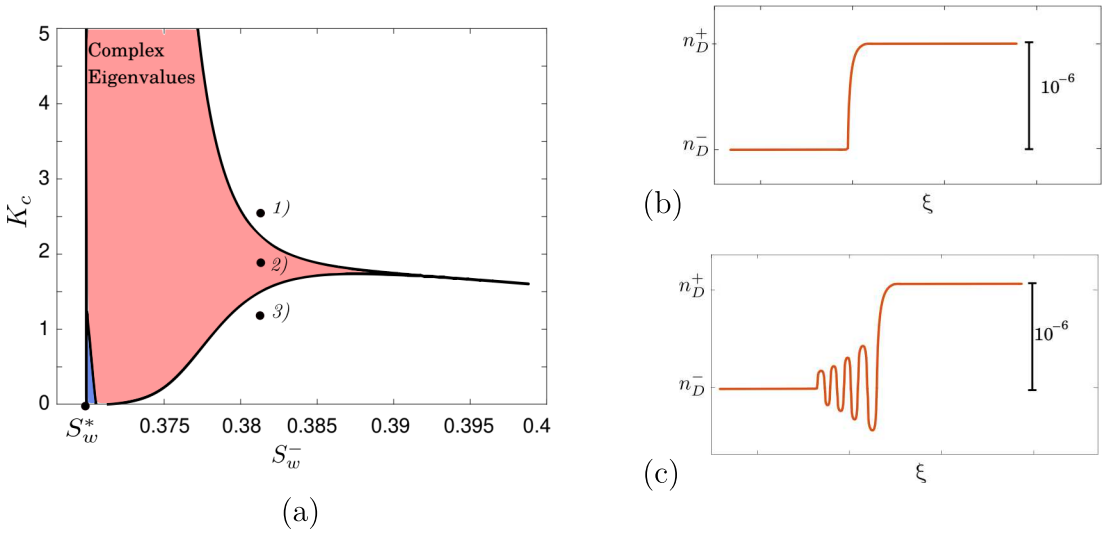

Figura 14 – Analysis of instabilities for a small variations of the parameter K_c. (a) The "pinched" part of Region **III** surrounded by Region **II**. Fixing S_w^- we consider three points varying K_c. (b) Profile solution of n_D corresponding to points *1)* and *3)* in Region **II**. (c) Profile solution of n_D corresponding to point *2)* in Region **III**.

The second type of instability is connected to the value of S_w^-. As shown in Figure 15(a) a small change in S_w^- can also result in qualitatively different solutions as showed in Figure 15(b), (c) and (d).

During physically accurate simulations of the drainage process, the water saturation can approach the critical value (S_w^*) [30]. Thus, water saturation can cross S_w^* many times. The moment the water saturation enters one of the three regions plotted in Figure 15(a), the exact solution changes to one of the solution types described in Figure 15(b)-(d). We believe that this behavior can be visually similar to numerical instabilities or instabilities caused by the porous medium heterogeneity.

Another application of this classification is a better understanding of the foam flow behavior in the vicinity of critical saturation point S_w^*. In [68], it was observed the localized and abrupt decay in the total relative mobility close to the shock front. This behavior was attributed to numerical issues. In [30], this abrupt decay was observed during numerical simulations. In [71], a similar behavior was observed in coreflood laboratory experiments. Notice that for S_w^- inside Region **VI** and close to Region **III** the mathematical solution includes a small decay in the saturation before the shock, see Figure 11(b). When one

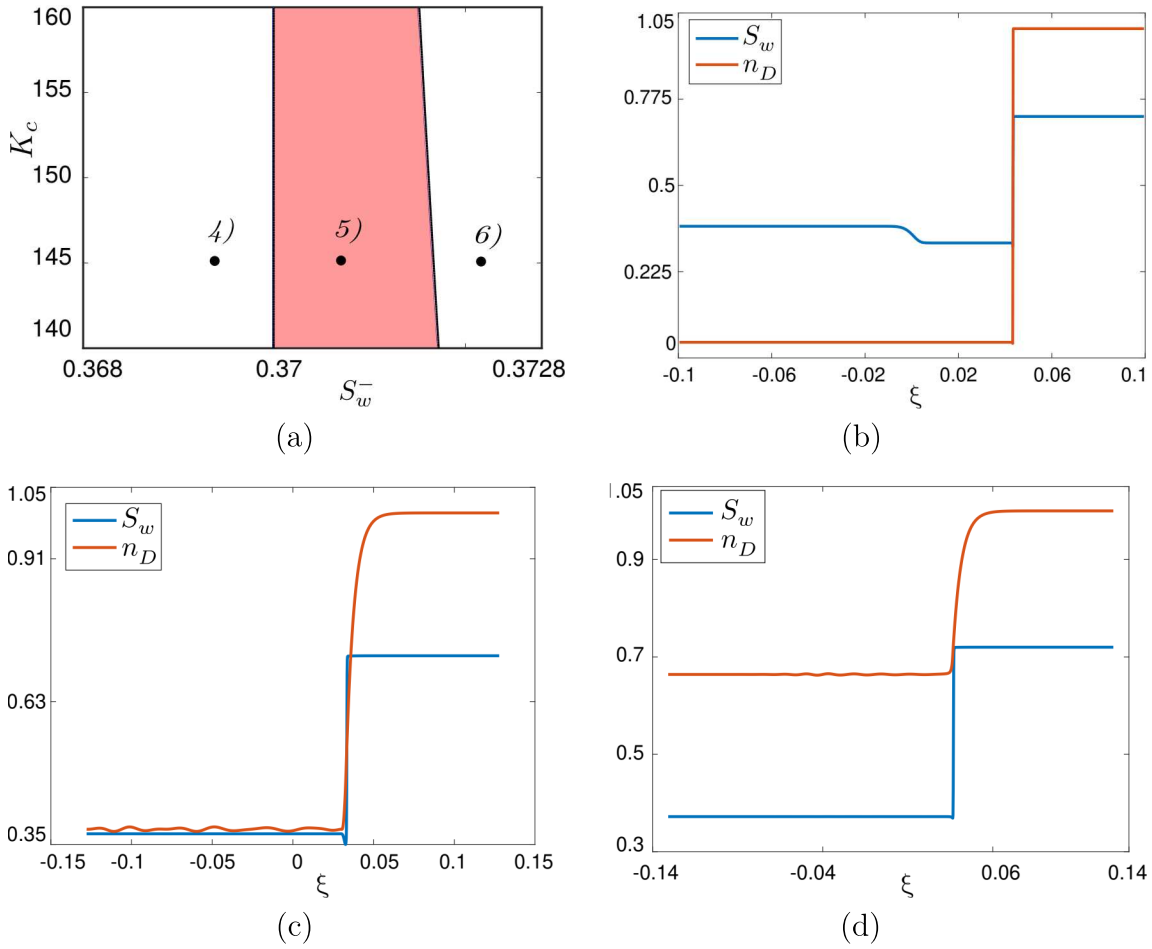

Figura 15 – Analysis of instabilities for a small variations of S_w^- on the border between regions **II**, **III** and **VI**. (a) Zoom near point $S_w^- = S_w^*$, $K_c = 145$. For a fixed K_c we consider three points varying S_w^- close to S_w^*. (b) Numerical solution profile for point *4)* in Region **VI**. (c) Numerical solution profile for point *5)* in Region **III**. (d) Numerical solution profile for point *6)* in Region **II**.

substitutes this solution into the total relative mobility equation, it results in a similar decay plotted in Figure 16.

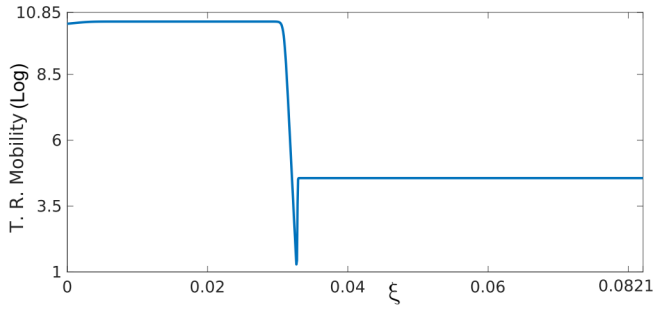

Figura 16 – A decay in the total relative mobility of gas for S_w^- inside Region **VI** close to S_w^*.

4 ANALYTICAL SOLUTION FOR THE POPULATION-BALANCE MODEL DESCRIBING FOAM DISPLACEMENT

This chapter is a reprint of work published in Transport in Porous Media, 2021 by Springer. [89]. DOI:10.1007/s11242-021-01589-z

In this chapter, we address the analytical solution of the simplified version of the mechanistic model model presented in [94]. We follow [2, 3] neglecting the apparent gas viscosity dependence on gas velocity, allowing us to search for traveling wave solutions.

We aim provide analytical solutions and, consequently, a better physical understanding of experimental data provided in [73, 74]. These experiments consisted in the co-injection of surfactant solution and gas into Bentheimer sandstone cores having, respectively, the porosity of about $20 \pm 1\%$ and permeability of about $2.0 \pm 2\%$ D. Saturation maps obtained by CT scanning the core were used to generate the saturation profiles at specific time intervals.

Considering negligible gas saturation at the initial reservoir conditions, we obtained analytical solutions for any injected water saturation, similar to the classical Buckley-Leverett theory, see [13]. We observed that there are two regions (I and II) in the parameter space, which will be detailed later in this chapter. All injection conditions in the considered experimental data [73, 74] correspond to Region I (shock region in Buckley-Leverett theory). They present a traveling wave solution with a good match with the experimental data. Similarly to rarefactions in Buckley-Leverett theory, analytical solutions in Region II are wave sequences.

This chapter is organized as follows. Section 4.1, presents the simplified foam displacement model used in this chapter. Section 4.2 is focused on the traveling wave solution, including solution classification based on the equilibria analysis. Section 4.3 presents the comparison of analytical solutions presented in this chapter with experimental data validating the approach. Finally, in Section 4.4 some conclusions are summarized.

4.1 THE SIMPLIFIED MODEL

In this chapter, we studied bubble population foam model in a porous medium described by the water mass balance (Rapoport-Leas equation) and the foam texture balance presented in (2.13)-(2.14) with (2.19), [74]:

$$\phi \frac{\partial}{\partial t}(S_w) + \frac{\partial}{\partial x}\left(u\, f_w + f_w \lambda_g \frac{dP_c}{dS_w}\frac{\partial S_w}{\partial x}\right) = 0, \tag{4.1}$$

$$\phi \frac{\partial}{\partial t}(S_g\, n_D) + \frac{\partial}{\partial x}(u_g\, n_D) = \Phi, \tag{4.2}$$

where ϕ is the porosity, u is the superficial velocity of the mixture (water+gas), P_c is the capillary pressure, u_g is the superficial velocity of the gas phase, the dimensionless foam

texture n_D is defined as a total foam texture n_f divided by a reference foam texture n_{max} (*i.e.* $n_D = n_f/n_{max}$).

Using bubble generation and coalescence coefficients K_g and K_d, in [94], the foam generation source term is written as $\Phi = \phi S_g[K_g(1 - n_D) - K_d n_D]$. Notice that it can be rewritten as

$$\Phi = \phi S_g(K_d + K_g)(n_D^{LE} - n_D), \quad \text{where} \quad n_D^{LE} = \frac{K_g}{K_g + K_d}. \tag{4.3}$$

In this form, the source term is similar to analogous terms appearing in [3, 48] with constant equilibrium foam texture. One can notice that the change of behavior for generation/coalescence depends on $K_g/(K_g + K_d)$. Thus, mathematically, both cases $K_d = 0$ and $K_d \neq 0$ are equivalent. As in [74], the authors consider $K_d = 0$, we follow the same assumption, yielding $n_D^{LE} = 1$. This assumption is even more precise if gas and a surfactant solution are forced through a porous medium saturated with the same surfactant solution, practically, $K_d = 0$.

We consider the medium saturated *i.e.*, $S_w + S_g = 1$. The total Darcy velocity can be written as $u = u_w + u_g$. In the context of foam displacements, the fractional-flow theory was first applied in [92]. The following standard assumptions are considered in this chapter [69, 70]: 1D horizontal flow, incompressibility of all phases, immediate attainment of local steady-state mobilities, Newtonian mobilities, absence of dispersion, absence of viscous fingering, and small capillary pressure gradients. Following [13], the water fractional flow f_w and relative mobilities of water and gas are given in Section (2.1). The water phase relative permeability k_{rw} is given by

$$k_{rw}(S_w) = \begin{cases} 0 & \text{if} \quad 0 \leq S_w \leq S_{wc}, \\ c_{krw}\left(\dfrac{S_w - S_{wc}}{1 - S_{wc} - S_{gr}}\right)^{\lambda} & \text{if} \quad S_{wc} < S_w \leq 1 - S_{gr}, \\ c_{krw} & \text{if} \quad 1 - S_{gr} < S_w \leq 1, \end{cases} \tag{4.4}$$

where c_{krw} is the end-point relative water permeability, λ is a modified pore-size-distribution parameter, S_{wc} is the connate water saturation, and S_{gr} is the residual gas saturation. The gas phase relative permeability k_{rg} is given by

$$k_{rg}(S_w, n_D) = \frac{k_{rg}^0(S_w)}{MRF(n_D)}, \tag{4.5}$$

where, following [3], we include the foam Mobility Reduction Factor $MRF = \beta n_{max}\, n_D + 1$ in the relative permeability. The foam free gas relative permeability is

$$k_{rg}^0(S_w) = \begin{cases} c_{krg}^0 & \text{if} \quad 0 \leq S_w < S_{wc}, \\ c_{krg}^0\left(\dfrac{S_w - S_{wc}}{1 - S_{wc} - S_{gr}}\right)^{(3\lambda+2)/\lambda} & \text{if} \quad S_{wc} \leq S_w < 1 - S_{gr}, \\ 0 & \text{if} \quad 1 - S_{gr} \leq S_w \leq 1, \end{cases} \tag{4.6}$$

where c^0_{krg} is the gas end-point relative permeability. The capillary pressure is given by

$$P_c = p_{c,0} \cdot \gamma \cdot \left(\frac{S_w - S_{wc}}{0.5 - S_{wc}}\right)^{-\frac{1}{\lambda}}, \qquad p_{c,0} = 2(\sigma_{gw}/r)\, cos(\theta), \tag{4.7}$$

where $p_{c,0}$ is the entry capillary pressure, γ is a proportionality coefficient, σ_{gw} is the surface tension between water and gas, θ is the contact angle and, r is effective pore radius.

The form of modeling foam mobility based on [3] is the main difference from the model used in [73, 74, 94]. It is necessary for analytical solutions, which are the focus of this article.

To fit the MRF function to experimental data, we need to estimate the parameters value β. We do so by equating the mobilities from [37] and the one used here:

$$k\frac{k_{rg}}{\mu_g^0 + \alpha^0 \frac{n_f}{(v_f)^d}} = k\frac{k_{rg}}{\mu_g^0\,(1 + \beta\, n_D\, n_{max})}, \tag{4.8}$$

where $v_f = u_g/(\phi S_g)$ is the approximate foam velocity, α^0 is the viscosity proportionality constant, and we consider $S_g = 1$ for this estimate. Then,

$$\beta = \frac{\alpha^0}{(v_f)^d\, \mu_g^0}. \tag{4.9}$$

The system of PDEs (4.1)-(4.2) was solved as a Riemann problem, *i.e.*, considering a step function initial conditions:

$$S_w(x,0) = \begin{cases} S_w^-, & x < 0, \\ S_w^+, & x > 0, \end{cases} \qquad n_D(x,0) = \begin{cases} n_D^-, & x < 0, \\ n_D^+, & x > 0. \end{cases} \tag{4.10}$$

The superscripts "+" and "−" mean the given expression is evaluated at conditions downstream (reservoir conditions or the right state) and upstream of the wave (injection conditions of the left state).

4.2 TRAVELING WAVE SOLUTION

We seek solutions to the System (4.1)-(4.2) in the form of traveling waves, *i.e*, solutions that maintain their shape in time and move at constant velocity v. These solutions only depend on the traveling variable $\xi = x - vt$, which means that the original system of PDEs is transformed into a system of ODEs. Traveling wave solutions commonly appear in nonlinear transport problems involving balance equations [84].

The traveling wave solution of System (4.13)-(4.14) is illustrated in the Section 2.5. In this chapter we use the parameters given in Table 3.

Tabela 3 – Model parameters used in this chapter. "Values 2015" correspond to [74]. For the parameters whose values were not presented in [73] we repeat the values from the other experiment summarized in "Values 2013". Parameter β was fitted using Eq. (4.9). PV values were fitted as explained in Section 4.3.1.

Symbol	*Parameter*	*Values 2015*	*Values 2013*
ϕ [-]	Porosity	0.21	0.21
u [m/s]	Total Darcy velocity	$1.6156 \cdot 10^{-5}$	$1.6156 \cdot 10^{-5}$
u_w [m/s]	Water velocity	$1.446 \cdot 10^{-6}$	$1.446 \cdot 10^{-6}$
u_g [m/s]	Gas velocity	$1.471 \cdot 10^{-5}$	$1.471 \cdot 10^{-5}$
K_g [s^{-1}]	Bubble generation coefficient	0.1	0.1
K_d [s^{-1}]	Bubble coalescence coefficient	0	0
n_{max} [m^{-3}]	Maximum bubble density	$2.5 \cdot 10^{11}$	$2.5 \cdot 10^{11}$
k [m^2]	Absolute permeability	$2.5 \cdot 10^{-12}$	$2.5 \cdot 10^{-12}$
S_{wc} [-]	Connate water saturation	0.10	0.10
S_{gr}[-]	Residual gas saturation	0	0
c_{krw}	Water end point relative perm.	0.75	0.75
c^0_{krg}	Foam end point relative perm.	1.0	1.0
μ_w [Pa s]	Water viscosity	$1.0 \cdot 10^{-3}$	$1.0 \cdot 10^{-3}$
μ_g [Pa s]	Gas viscosity	$1.8 \cdot 10^{-5}$	$1.8 \cdot 10^{-5}$
λ [-]	Pore-size-distribution parameter	5.0	5.0
β [m^3]	Non-Newtonian mobility param.	$7.8185 \cdot 10^{-10}$	$7.8185 \cdot 10^{-10}$
d [-]	Power law viscosity exponent	1/3	1/3
α^0 [$Pa\,s^{2/3}\,m^{10/3}$]	Viscosity proportionality const.	$5.8 \cdot 10^{-16}$	$5.8 \cdot 10^{-16}$
γ [-]	Capillary pressure coefficient	0.5	0.5
σ_{gw} [N/m]	Gas-water interfacial tension	$30.0 \cdot 10^{-3}$	$30.0 \cdot 10^{-3}$
θ [rad]	Contact angle	0	0
r [m]	Mean pore radius	$5 \cdot 10^{-6}$	$5 \cdot 10^{-6}$
D [m]	Core diameter	0.038	0.038
L [m]	Core length	0.384	0.17

Changing coordinates $(x,t) \longrightarrow (\xi = x - vt, t)$ in System (4.1)-(4.2) and considering the stationary solution yields:

$$\left(-f_w \lambda_g \frac{dP_c}{dS_w}\right) \frac{dS_w}{d\xi} = u[(f_w - v_s S_w) - (f_w - v_s S_w)^+], \tag{4.11}$$

$$\left(-u(v_s(1 - S_w^+) - 1 + f_w^+)\right) \frac{dn_D}{d\xi} = \phi(1 - S_w) K_g (1 - n_D). \tag{4.12}$$

System (4.11)-(4.12) can be rewritten in a standard form using boundary conditions (4.10) (see [3] for details):

$$\frac{dS_w}{d\xi} = \frac{u[f_w - v_s S_w - (f_w - v_s S_w)^+]}{-\lambda_g f_w \frac{dP_c}{dS_w}}, \tag{4.13}$$

$$\frac{dn_D}{d\xi} = \frac{\phi(1 - S_w)\, K_g (1 - n_D)}{-u\,[v_s(1 - S_w^+) - (1 - f_w^+)]}, \tag{4.14}$$

where

$$v_s = v\phi/u. \tag{4.15}$$

Notice that the passage from (4.11)-(4.12) to System (4.13)-(4.14) is only possible if functions on the right side in (4.13)-(4.14) are well defined for $S_{wc} \leq S_w \leq 1 - S_{gr}$. For the numbers presented in Table 3 this is true only if $S_w \neq 1$ or, equivalently if $S_{gr} \neq 0$.

We are interested in validating our solutions with experimental data from [73, 74], where S_w^+ was considered one. In order to do it, we consider $S_w^+ = 0.999$ in this chapter.

4.2.1 Classification of equilibria

Mathematically, equilibrium is a stationary solution of System (4.13)-(4.14) or, equivalently, the point (S_w, n_D) for which the right side of System (4.13)-(4.14) is zero. The traveling wave solutions always connect equilibria in the sense of Eq. (2.48). To proceed with the analysis and show the existence of such a connection, one has to find and classify all possible equilibria of System (4.13)-(4.14).

The right side of Equation (4.14) is zero if $S_w = 1$ or $n_D = 1$. As noticed previously, $S_w \neq 1$, otherwise System (4.13)-(4.14) is not well defined. The only valid option is $n_D = 1$, in particular $n_D^- = 1$, and $n_D^+ = 1$. Therefore, from equating the expression (4.14) to zero follows:

$$f_w(S_w, 1) - v_s S_w - f_w^+ + v_s S_w^+ = 0, \quad v_s = \frac{f_w^+ - f_w^-}{S_w^+ - S_w^-}. \tag{4.16}$$

As for viscous Buckley-Leverett equation, equilibria of System (4.13)-(4.14) stay on the line $n_D = 1$, and on the curve defined in Eq. (4.16), see Fig. 17 for graphical representation using parameter values from Table 3. Beside (S_w^-, n_D^-) and (S_w^+, n_D^+) can exist another equilibrium, see Fig. 17, in following possibilities:

- If $S_w^- \in [S_{wc}, S_w^T[$, there are three equilibria S_w^-, S_w^e and S_w^+, such that $S_w^- < S_w^e < S_w^+$.
- If $S_w^- \in]S_w^T, S_w^M]$, there are three equilibria S_w^-, S_w^e and S_w^+, such that $S_w^e < S_w^- < S_w^+$.
- In other cases, there are only two equilibria S_w^- and S_w^+.

Equilibrium points appearing in this chapter are classified according to their eigenvalues as definned in Section 2.5 (see [34, 76] for details).

Notice that building an orbit that connects two equilibria asymptotically is not always possible. For example, there is no orbit in the following cases: (1) right equilibrium is a source, or (2) left equilibrium is a sink.

In this section, we classify the traveling wave solutions of System (4.1)-(4.2), which are solutions of System (4.13)-(4.14) with boundary limits (2.48), for a fixed right equilibrium S_w^+ varying the left equilibrium S_w^-. Eigenvalues of the Jacobian matrix associated with the vector field in (4.13)-(4.14) in neighborhoods of equilibria (S_w^-, n_D^-) and (S_w^+, n_D^+) describe the necessary condition for the existence of the traveling wave.

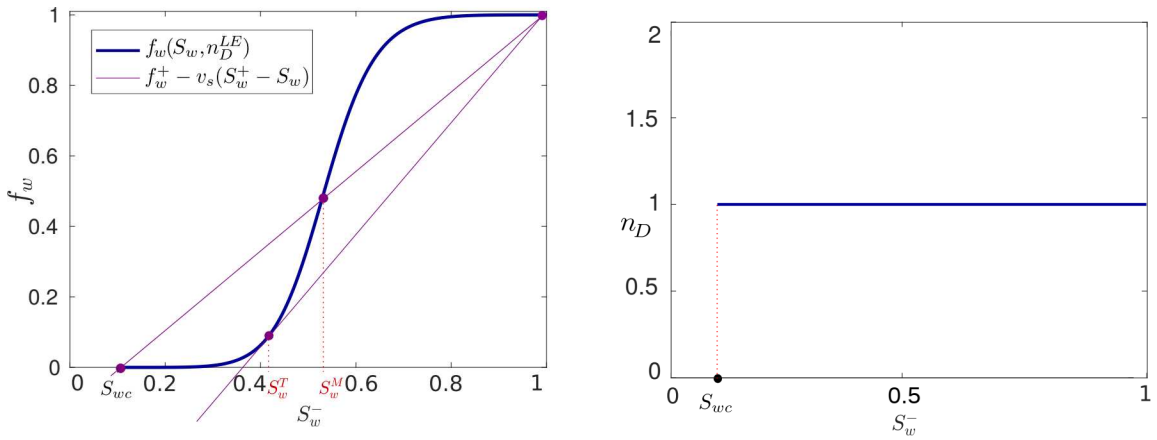

(a) (b)

Figura 17 – Equilibria of System (4.13)-(4.14) for $S_w^+ = 0.999$, $K_g = 0.1$ and $n_{max} = 250$ mm^{-3}. Point S_w^T indicate the intersection point between the curve of f_w and the tangent line to f_w that passes through (S_w^+, f_w^+). Point S_w^M indicate the intersection between the curve of f_w and the line connecting $(S_{wc}, f_w(S_{wc}))$ to (S_w^+, f_w^+). (a) The solid curve represent the water fractional flow in Eq. (4.16). (b) Line $n_D = 1$ along which are the equilibria of System (4.13)-(4.14).

As the system is bidimensional, there are two eigenvalues of the Jacobian matrix. In what follows, the superscript $(-)$ and $(+)$ denote the eigenvalues associated with the left and the right equilibria, respectively. We use the following notation: $\lambda_1^{\pm} = \lambda_1(S_w^{\pm}, n_D^{\pm})$ and $\lambda_2^{\pm} = \lambda_2(S_w^{\pm}, n_D^{\pm})$. We assume $\lambda_1^- < \lambda_2^-$ and $\lambda_1^+ < \lambda_2^+$.

Following the previous explanation, there are two regions: Region I with $\lambda_1^- > 0$, $\lambda_2^- > 0$, $\lambda_1^+ < 0$, $\lambda_2^+ > 0$ indicated with yellow color in Fig. 18, and Region II with $\lambda_1^- < 0$, $\lambda_2^- > 0$, $\lambda_1^+ < 0$, $\lambda_2^+ > 0$ indicated with blue color in Fig. 18. The curve separating both regions, which is important to the proceeding analysis corresponds to $\lambda_1^- = 0$, $\lambda_2^- > 0$, $\lambda_1^+ < 0$, $\lambda_2^+ > 0$.

In order to graphically represent these regions we do the following. Following [3, 56] and using the kinetic foam generation parameter K_g, we fix $n_{max} = 250$ mm^{-3} and plot regions in the parameter space $S_w^- \times K_g$, see Fig. 18(a). We also plot them in the parameter space $S_w^- \times n_{max}$, see Fig. 18(b), allowing to visualize better all experimental data presented in [73, 74].

4.2.2 **Region** I

In this section, we investigate a traveling wave solution of System (4.1)-(4.2) for the injection conditions in Region I. In this case the left equilibrium is a source ($\lambda_1^- > 0$ and $\lambda_2^- > 0$) and the right equilibrium is a saddle ($\lambda_1^+ < 0$ and $\lambda_2^+ > 0$). This case corresponds to the viscous shock profile in Buckley-Leverett theory, see [75]. In this case, there are two possibilities: (i) $S_w^- \in]S_w^M, S_w^+[$ or (ii) $S_w^- \in]S_w^T, S_w^M]$.

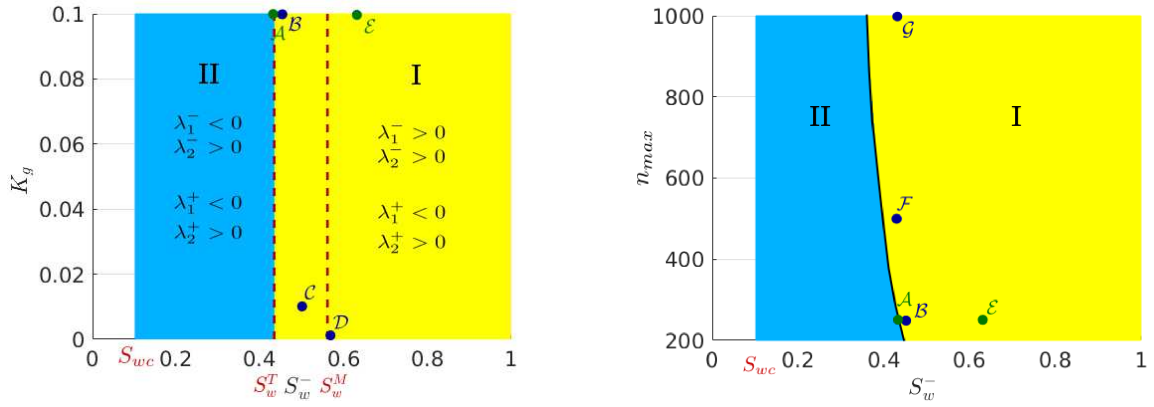

(a) (b)

Figura 18 – Regions' classification according to the equilibrium type for $S_w^+ = 0.999$ and $K_d = 0$. Points S_w^T (boundary between regions I and II) and S_w^M (boundary between sub-regions with two and three equilibria) are obtained, as explained in Fig. 17. Simulations presented later in this chapter are represented with point $\mathcal{A}$, $\mathcal{F}$ and $\mathcal{G}$ (correspond to Figs. 27 and 28); points $\mathcal{B}$, $\mathcal{C}$ and $\mathcal{D}$ (correspond to Figs. 29 and 30). Experimental results correspond to points $\mathcal{A}$ and $\mathcal{E}$ (see Section 4.3.2). (a) Space $S_w^- \times K_g$ and $n_{max} = 250$ mm^{-3}. (b) Space $S_w^- \times n_{max}$ and $K_g = 0.1$.

(i) If $S_w^- \in]S_w^M, S_w^+[$, there are only two equilibria (left and right). There is an orbit connecting the left to right, see Fig. 19(a). Therefore, there is a traveling wave solution of System (4.1)-(4.2) plotted in Fig. 19(b).

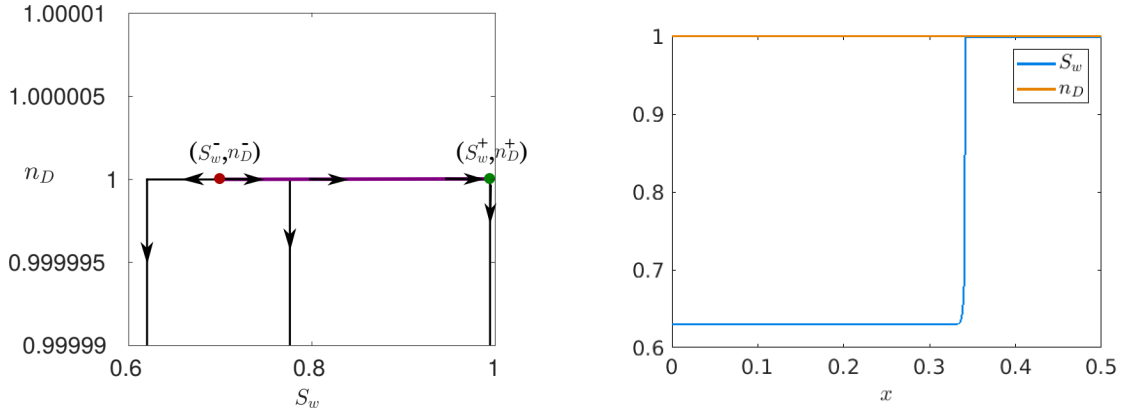

(a) (b)

Figura 19 – Case $S_w^- \in]S_w^M, S_w^+[$. Riemann problem solution for $(S_w^-, n_D^-) = (0.63, 1)$, $(S_w^+, n_D^+) = (0.999, 1)$, $K_g = 0.1$, and $n_{max} = 250$ mm^{-3}. (a) Orbits of System (4.13)-(4.14) in phase portrait. There is an orbit connecting (S_w^-, n_D^-) to (S_w^+, n_D^+). (b) Solution profile of (4.1)-(4.2).

(ii) If $S_w^- \in]S_w^T, S_w^M[$, there are three equilibria. Besides (S_w^-, n_D^-) and (S_w^+, n_D^+) there exists a saddle equilibrium (S_w^e, n_D^e), were $S_w^e \in]S_{wc}, S_w^T[$. In this case, there is an orbit connecting left and right equilibria, see Fig. 20(a). Therefore, there is a traveling wave solution of System (4.1)-(4.2) as plotted in Fig. 20(b).

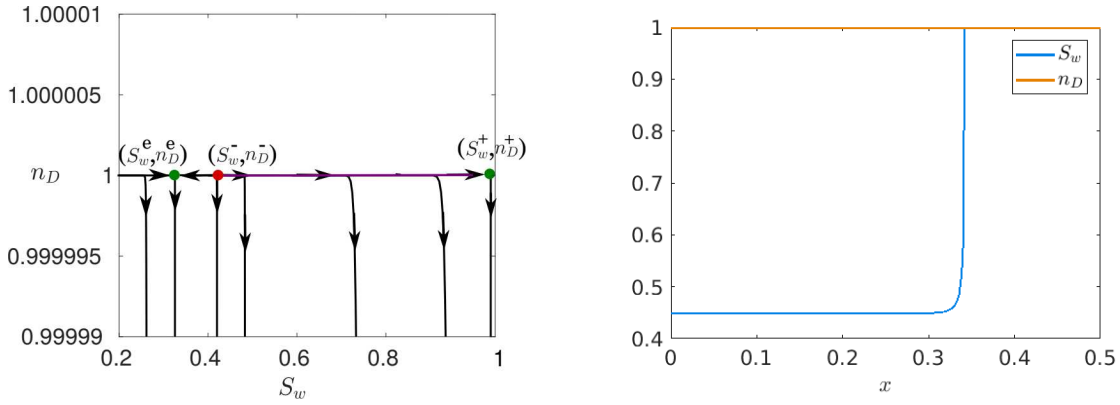

Figura 20 – Case $S_w^- \in]S_w^T, S_w^M]$. Riemann problem solution for $(S_w^-, n_D^-) = (0.45, 1)$, $(S_w^+, n_D^+) = (0.999, 1)$, $K_g = 0.1$, and $n_{max} = 250$ mm^{-3}. (a) Orbits of System (4.13)-(4.14) in phase portrait. There is an orbit connecting (S_w^-, n_D^-) to (S_w^+, n_D^+). (b) Solution profile of (4.1)-(4.2).

4.2.3 **Boundary between regions** I **and** II

Along the line $S_w^- = S_w^T$ in Fig. 18, there is a bifurcation in the System (4.13)-(4.14) solution's topology. When S_w^- approaches continuously to S_w^T from Region I to Region II, the eigenvalue λ_1^- tends to zero, and S_w^e approaches S_w^T from Region II to Region I, see Fig. 21. In the other hand, when considering S_w^- approaching S_w^T the connection (in the sense of Eq. (2.48)) between (S_w^-, n_D^-) and (S_w^+, n_D^+) persists.

When $S_w^- = S_w^T$ we have only two equilibria (left and right states). In this case, the left state is a node ($\lambda_1^- = 0$ and $\lambda_2^- > 0$) and the right state is a saddle ($\lambda_1^+ < 0$ and $\lambda_2^+ > 0$). In this case there is a connection joining one of the unstable directions of the node (S_w^-, n_D^-) to the saddle (S_w^+, n_D^+), see Fig. 22(a). Therefore, there is a traveling wave solution of System (4.1)-(4.2) as plotted in Fig. 22(b).

4.2.4 **Region** II

In this case, the left state is a saddle ($\lambda_1^- < 0$ and $\lambda_2^- > 0$), and the right state is a saddle ($\lambda_1^+ < 0$ and $\lambda_2^+ > 0$). As observed in Section 4.2.1 for S_w^- in Region II, there exist three equilibria along the line $n_D = n_D^{LE} = 1$ satisfying $S_w^- < S_w^e < S_w^+$, see Fig. 18. Thus there is no direct connection between (S_w^-, n_D^-) and (S_w^+, n_D^+).

From numerical simulations, we observe that the Riemann problem solution, in this case, is a sequence of two waves: one spreading wave connecting (S_w^-, n_D^-) to $(S_w^T, 1)$ and one traveling wave connecting $(S_w^T, 1)$ to (S_w^+, n_D^+), see Fig. 23. Notice that, in the absence of capilary effects, this region would correspond to rarefaction wave in Buckley-Leverett theory.

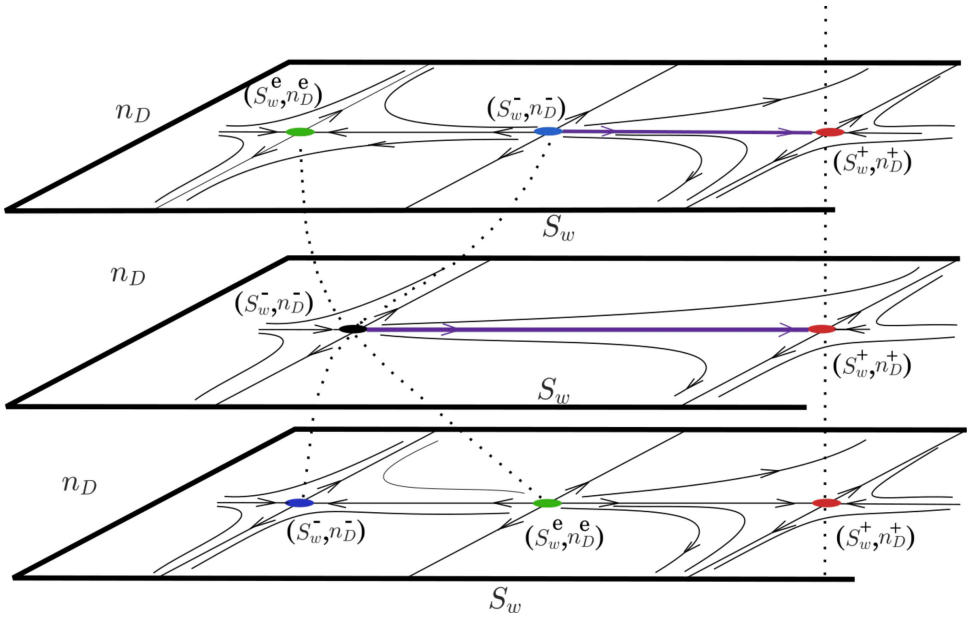

Figura 21 – Schematic representation of System (4.13)-(4.14) solution's bifurcation happening when S_w^- moves between regions I and II (see Fig. 18). Red point represents the saddle equilibrium S_w^+, green point represents the equilibrium (S_w^e, n_D^e), blue point represents the saddle equilibrium S_w^-, and black point represents the node equilibrium $S_w^- = S_w^T$. The upper plane corresponds to Region I, the middle plane to the boundary and the lower plane corresponds to Region II.

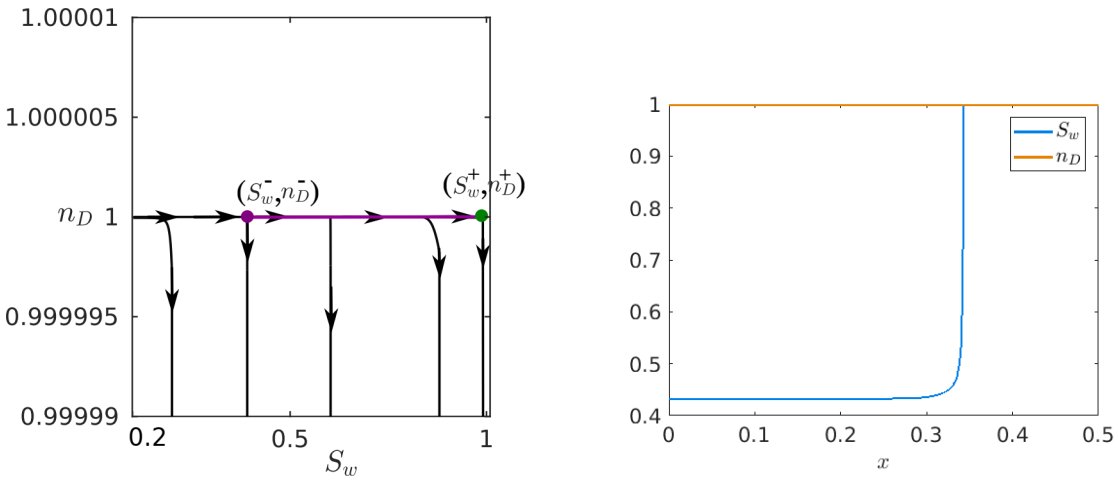

Figura 22 – Case $S_w^- = S_w^T$. Riemann problem solution for $(S_w^-, n_D^-) = (S_w^T, 1)$, $(S_w^+, n_D^+) = (0.999, 1)$, $K_g = 0.1$, and $n_{max} = 250$ mm^{-3}. (a) Orbits of System (4.13)-(4.14) in phase portrait. There is an orbit connecting (S_w^-, n_D^-) to (S_w^+, n_D^+). (b) Solution profile of (4.1)-(4.2).

4.3 APPROACH VALIDATION

This section compares our analytical results to numerical and experimental results presented in [73, 74].

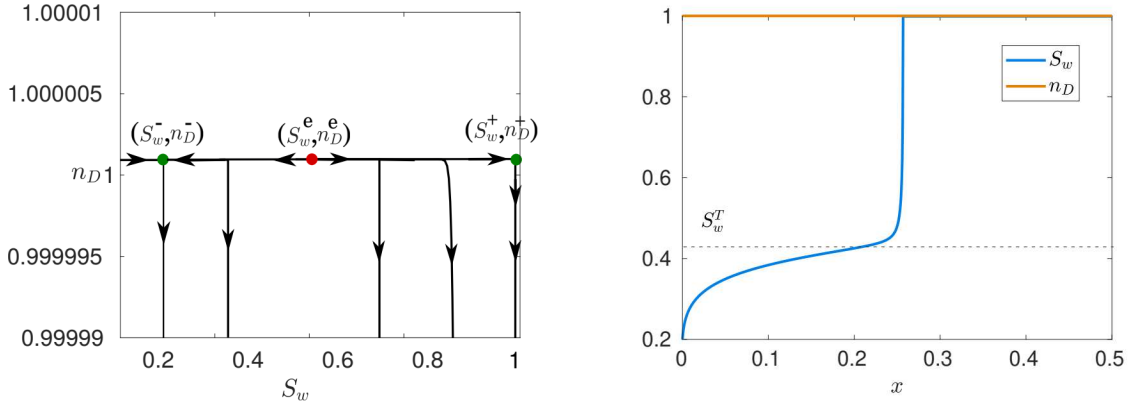

Figura 23 – Case $S_w^- \in]S_{wc}, S_w^T[$ in Region II, $K_g = 0.1$, and $n_{max} = 250$ mm^{-3}. (a) There is no direct connection from (S_w^-, n_D^-) to (S_w^+, n_D^+). (b) Riemann problem solution of System (4.1)-(4.2) for $(S_w^-, n_D^-) = (0.2, 1)$, $(S_w^+, n_D^+) = (0.999, 1)$.

4.3.1 Experiment description

For the chapter's self completeness, we present a brief description of the experiment details here.

Alpha Olefin Sulfonate (AOS) surfactant and nitrogen gas were used to generate foam inside the core-holder with Bentheimer sandstone core in both experiments. The sample was encapsulated in a thin layer of low X-ray attenuation Araldite self-hardening glue. The core-holder itself was made of synthetic material with good mecptionhanical properties and a low X-ray attenuation. Core flooding experiments used the following sequence:

1. First, the air was removed from the core using CO_2;
2. Then, the dry core was saturated by injecting brine;
3. Next, the surfactant solution was injected into the core.

Then N_2 gas and surfactant solution were injected simultaneously from the bottom of the core to generate foam in the porous medium varying either the surfactant concentration or the total superficial velocity. The water saturation values were determined by using an X-ray CT scan. For further details on the experiment, see [73].

The parameter values corresponding to experimental results from [74] are in Table 3. The time corresponding to one injected porous volume (PV) was estimated using a given breakthrough time.

In [73], the parameters describing the fractional flow were not presented. As both experiments used similar setups, in order to validate our solutions, we consider parameter

values shown in Table 3. We estimate the PV value using the flow rate considering core saturation $S_w = 0.63$.

4.3.2 Experimental validation

The system's apparent viscosity, for experimental data, is obtained using Darcy law depending on pressure gradient and total system velocity [26, 54]. For theoretical models, it is more convenient to describe the apparent viscosity as an inverse of the total system mobility $\mu_{app} = k/(\lambda_g + \lambda_w)$, where λ_g depends on the foam texture as in Eq. (8). In order to compare the apparent viscosity for Newtonian (μ^N_{app}) and non-Newtonian shear thinning (μ^S_{app}) we substitute the corresponding mobility reduction factors into the equation describing gas velocity considering equilibrium conditions ($n_D = n_D^{LE}$) and solve the resulting inverse problem. The results are plotted in Figure 24. Notice that, in the literature, this type of graph presents a sharper transition, at some critical foam quality (f_g), due to the different relative permeability functions.

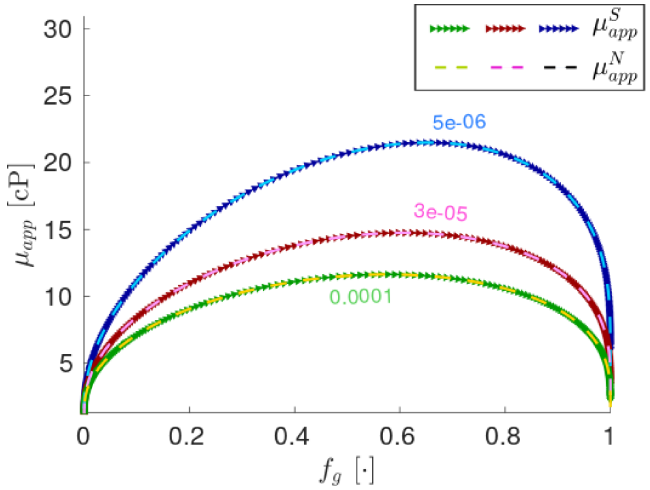

Figura 24 – The apparent viscosity of the system for three different gas velocities 10^{-4} m/s, $3 \cdot 10^{-5}$ m/s, and $5 \cdot 10^{-6}$ m/s.

We now compare the experimentally obtained water saturation profiles with the analytical solution. Figure 25 shows the comparison for data from [73] corresponding to the point $\mathcal{E}$ in Fig. 18. The same plot for data from [74] is shown in Fig. 26. This data corresponds to the point $\mathcal{A}$ in Fig. 18.

The analytical solution we seek here is of asymptotic type, i.e., the original problem, formulated in terms of partial differential equations, needs some time to present a solution in the form of a traveling wave. On the other hand, the experiment also takes a certain time to achieve stable front displacement. Thus theoretical and experimental data are expected to reach an agreement after some transient stage. As can be observed, the analytical solution is in good agreement with the experimental data for later times despite

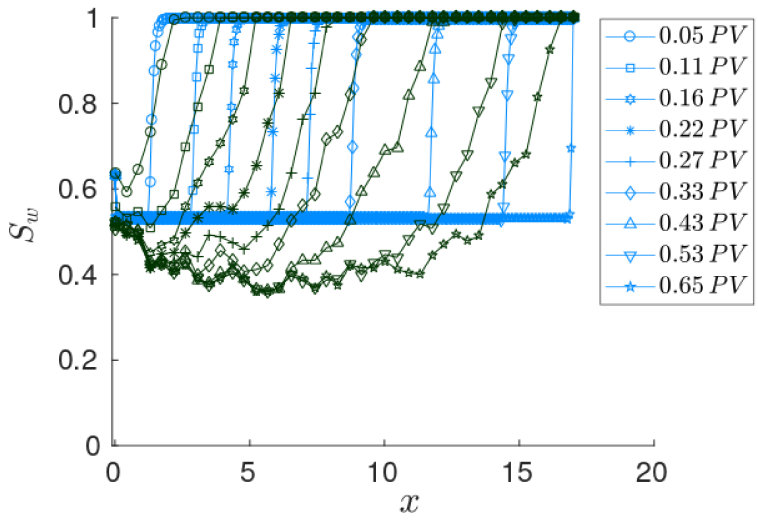

Figura 25 – Water saturation profiles at different times. Experimental data presented in [73] (dark green) compared to the solution of System (4.1)-(4.2) for $K_g = 0.1$, $n_{max} = 250$ mm^{-3} and $S_w^- = 0.63$ (blue).

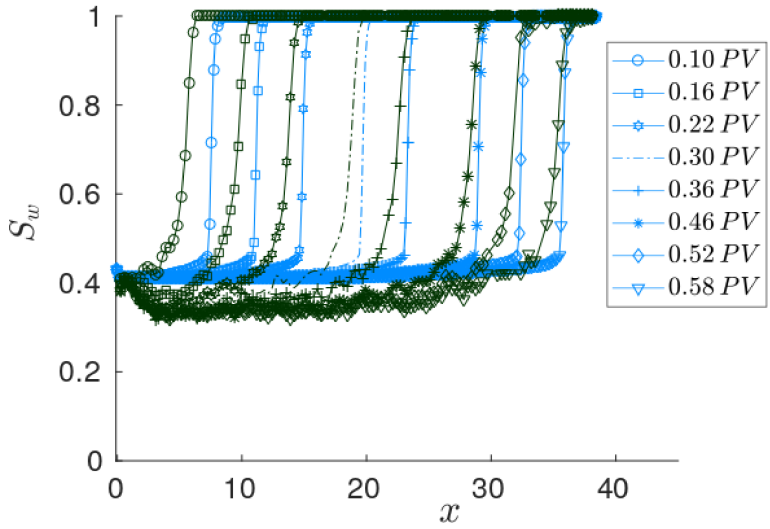

Figura 26 – Water saturation profiles at different times. Experimental data presented in [74] (dark green) compared to the solution of System (4.1)-(4.2) for $K_g = 0.1$, $n_{max} = 250$ mm^{-3} and $S_w^- = 0.43$ (blue).

the model's simplicity. Some key features of the analytical solution are in good agreement with the experimental data. For example, the experiments exhibit a traveling wave profile, which is correctly captured by analytical solutions, including a correct velocity. The fact that we obtain a good match between the model and both experiments evidences the robustness of the proposed approach. It shows further that, at least in some cases, it is acceptable to model the foam displacement in porous media assuming Newtonian behavior.

4.3.3 Numerical validation for different values of n_{max}

As explained in the introduction, the model used in [74] considered the apparent gas viscosity depending on gas velocity, as proposed in [37]. This model also takes pressure difference into account and uses complete Darcy's law. In what follows, we refer to it as a complete model. The authors [74] used the standard IMPES method (see [5, 21] for details) to obtain saturation profiles and validate them with experimental data for this model.

The model presented in Section 4.1 considers constant fluid velocity and a simplified version of apparent viscosity. In what follows, we call it a simplified model. To solve the system of PDEs (4.1)-(4.2) numerically, we use the nonlinear Crank-Nicolson implicit finite-difference scheme combined with Newton's method; see [50] for details. This scheme is second-order accurate both in space and time.

Below we compare the numerical solutions obtained by the two methods at the following times: $0.18\,PV = 838.2$s, $0.36\,PV = 1676.4$s, $0.54\,PV = 2514.6$s and considering parameter values from Table 3. Figs. 27 and 28 show respectively, the water saturation and foam texture (or bubble density described as $S_g n_f$) profiles for different values of n_{max}. We note that these solutions correspond to the points $\mathcal{A}$, $\mathcal{F}$, and $\mathcal{G}$ in Fig. 18.

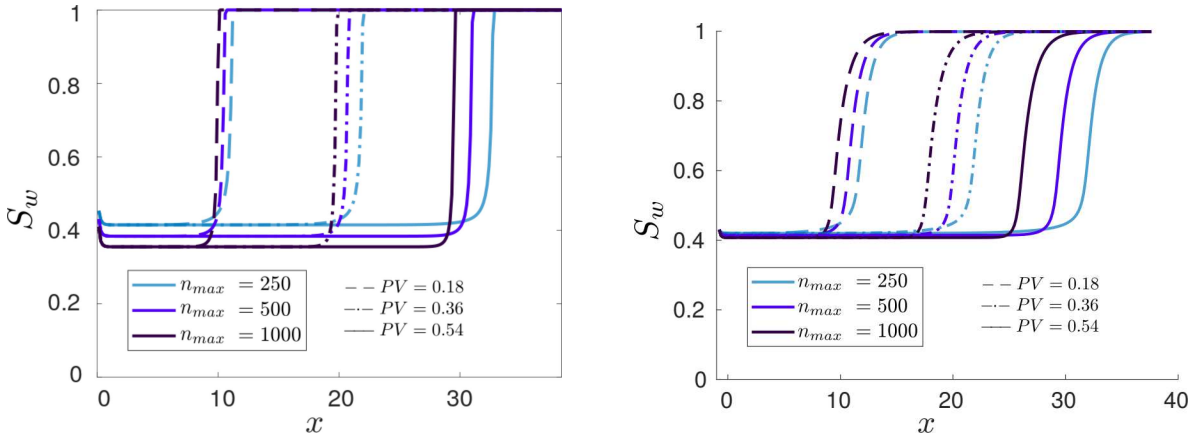

Figura 27 – Water saturation profiles for different values of n_{max} at different times. Here $(S_w, n_D)^- = (0.43, 0)$ and $(S_w, n_D)^+ = (0.999, 0)$. (a) Numerical results using IMPES and complete model, see [74]. (b) Solution of System (4.1)-(4.2).

The numerical simulation results of both models are in very good qualitative agreement, evidencing that the simplified model describes the main features of the physical phenomenon well. Examining the profiles more closely, we observed a few minor differences that we nevertheless would like to discuss. The simplified model seems to have a much smaller entrance effect (i.e., a slight decrease in the S_w) than the complete model. Next, the upstream saturation profiles decrease as the foam propagates while it remains constant in the case of the simplified model. Finally, saturation and bubble density fronts

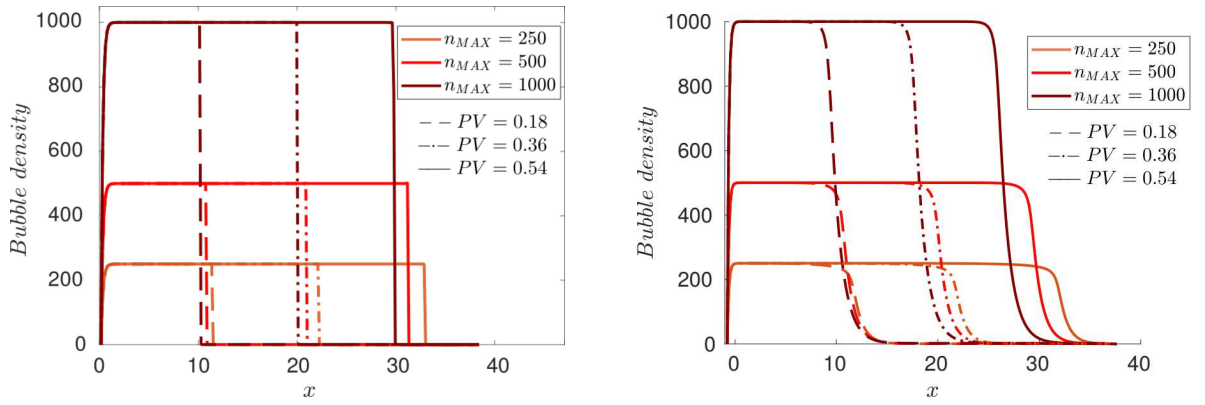

Figura 28 – Bubble density profiles for different values of n_{max} at different times. Here $(S_w, n_D)^- = (0.43, 0)$ and $(S_w, n_D)^+ = (0.999, 0)$. (a) Numerical results using IMPES and complete model, see [74]. (b) Solution of System (4.1)-(4.2).

present smoother profiles due to artificial diffusion, which was added to enable numerical convergence.

4.3.4 Numerical validation for different values of K_g

We now compare the numerical solutions for the complete and simplified models for different values of the kinetic foam generation parameter K_g, for $n_{max} = 250$ mm^{-3} and same times as in the previous section. The water saturation profiles and the bubble densities are plotted in Figs. 29 and 30. We considered left states $(S_w, n_D)^- = (0.45, 0)$, $(S_w, n_D)^- = (0.50, 0)$, and $(S_w, n_D)^- = (0.57, 0)$ corresponding to points $\mathcal{B}$, $\mathcal{C}$, and $\mathcal{D}$ in Fig. 18.

In addition to the previous section's remarks, simulations show some notable differences for both models. Firstly, we note transient behavior, which becomes more pronounced for small values of K_g. For the complete model, the traveling front takes more time to form and also presents a smoothing of the bubble density profile. Remarkably, the bubble density profiles for the complete model are systematically slower than for the simplified model. From experimental and numerical validation presented in this chapter, we conclude that the simplified (Newtonian) model represents well the saturation profiles. However, it does not seem to represent as well the bubble density distribution. Although the premise is that the foam displacement is physically better captured by the complete model based on its non-Newtonian nature, it is unclear which of the two models would match better the core-flood experiments. This is because, with current techniques, it is hard to measurement bubble densities.

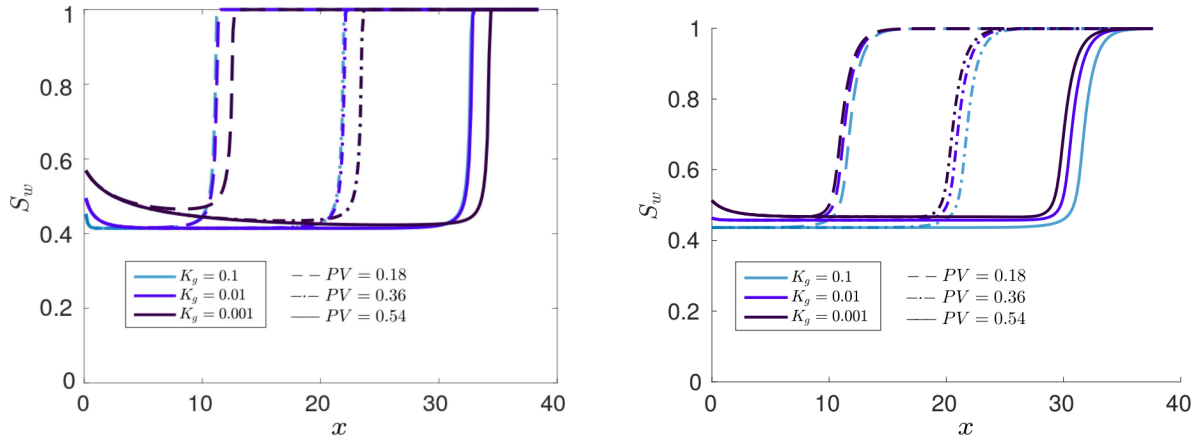

(a) (b)

Figura 29 – Water saturation profiles for different values of K_g at different times. Here $n_{max} = 250$ and $(S_w, n_D)^+ = (0.999, 0)$. (a) Numerical results using IMPES and complete model, see [74]. (b) Solution of System (4.1)-(4.2).

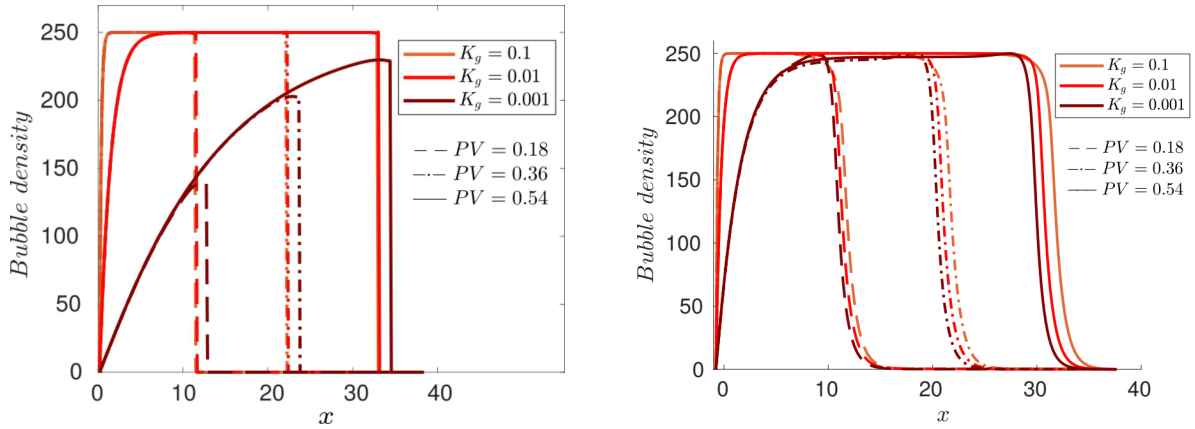

(a) (b)

Figura 30 – Bubble density profiles for different values of K_g at different times. Here $n_{max} = 250$ and $(S_w, n_D)^+ = (0.999, 0)$. (a) Numerical results using IMPES and complete model, see [74]. (b) Solution of System (4.1)-(4.2).

4.4 PARTIAL CONCLUSIONS

The analysis performed in the present chapter allowed us to obtain solutions in a broad parameter domain, pointing out the existence of flow profiles different from those found in the experiments.

Despite this model's simplicity, in the present chapter, we managed to adjust the model used to successfully describe the experiments allowing us to find analytical solutions as traveling waves. Obtained solutions present a change in behavior following Buckley-Leverett theory. The injection conditions in the examined experimental data correspond to Region I, where they present a traveling profile. In this region, the analytical solutions also match well the numerical simulations of the complete model. Analytical solutions for injection conditions in Region II present a different behavior, which was not

described earlier. They are a sequence of waves: one spreading wave and one traveling wave. From the physical point of view, each parameter region corresponds to a different flow regime. The new results suggest new experiments at lower injected water saturations for further verification.

5 FOAM FLOW IN POROUS MEDIA FOR LOW SURFACTANT CONCENTRATION

This chapter is a reprint of work under review.

The foam flow in porous media has been widely studied in applications, with main examples in the oil industry and in the environmental ecology, see [67, 86]. Among other properties, foam allows controlling the gas mobility improving the sweep efficiency, see [39, 94]. This effect can be significantly impaired by the surfactant adsorption to the surrounding matrix impacting the foam generation, and destruction [51, 58, 88]. It also motivates the investigation of foam dynamics with low surfactant concentration [80].

Above Critical Micelle Concentration (CMC), the surfactant starts forming micelles and does not significantly affect the foam formation [73]. A common simplification found in the literature assumes the surfactant concentration of the aqueous phase is almost constant and sufficiently large (above CMC) not to affect the bubble generation and destruction rate, see [3, 44, 48, 56, 89, 94]. Hence, no separate material balance equation on surfactant is needed. Such simplification is unrealistic; there are works stating that the surfactant's migration to the interfaces can decrease its concentration in the bulk solution. Thus, there is less surfactant available for new films (*lamellae*) formation, even if the initial concentration is above the CMC, see [10, 42]. In the present chapter, we extend the models investigated in [74, 89] by considering a separate balance equation to describe the surfactant concentration in the aqueous phase.

Several experimental investigations point to saturation and foam texture profiles similar to traveling waves [40, 41, 47, 48, 73, 74] motivating search for analytical solutions in the form of traveling waves [2, 3, 14, 55, 56, 89]. All these works considered the simplification of the apparent gas viscosity, originally proposed in [37, 59], assuming it to be Newtonian and independent of gas velocity. In the present chapter, we adopted these ideas and searched traveling wave solutions for the foam displacement model considering variable surfactant concentration and Newtonian foamed gas mobility.

This chapter is organized as follows. Section 5.1 presents a population balance foam model considering a separate balance equation to describe the surfactant concentration. Section 5.2 provides an adimesionalization for the model presented above. Section 5.3 formulated the system of ordinary differential equations describing the traveling wave solution. Section 5.4 investigates traveling wave solutions validating all analytical estimates with direct numerical simulations. Finally, in Section 5.5, some conclusions are summarized.

5.1 MATHEMATICAL FOUNDATIONS AND THE PHYSICAL MODEL

To describe the foam flow in a porous medium saturated with water and gas, we assume a one-dimensional flow with incompressible fluids, immediate attainment of

local steady-state mobilities, and negligible dispersion. The water mass conservation law (Rapoport-Leas) (5.1) and foam texture balance (5.2) equations are modeled following [74] with simplification proposed in [89], i.e., Newtonian mobilities and small pressure gradient resulting in a constant fluid velocity. Equation (5.3) describing a surfactant concentration follows [17] neglecting dispersion effects. Summarising, the model reads as

$$\frac{\partial}{\partial t}(\phi S_w) + \frac{\partial}{\partial x}(u\, f_w) + \frac{\partial}{\partial x}\left(f_w \lambda_g \frac{dP_c}{dS_w}\frac{\partial S_w}{\partial x}\right) = 0, \tag{5.1}$$

$$\frac{\partial}{\partial t}\left(\phi(1-S_w)n_f\right) + \frac{\partial}{\partial x}\left(u\,(1-f_w)n_f\right) - \frac{\partial}{\partial x}\left(f_w \lambda_g \frac{dP_c}{dS_w}\frac{\partial S_w}{\partial x} n_f\right) = Q, \tag{5.2}$$

$$\frac{\partial}{\partial t}\left(\phi S_w C_s\right) + \frac{\partial}{\partial x}\left(u\, f_w C_s\right) + \frac{\partial}{\partial x}\left(f_w \lambda_g \frac{dP_c}{dS_w}\frac{\partial S_w}{\partial x} C_s\right) = -\hat{\alpha}\, Q. \tag{5.3}$$

Inspired by the direct dependence between bubble generation and injected surfactant, which must increase until the latter reaches the CMC [28, 87], the foam generation source term Q [m^{-3}/s] is defined by

$$Q = \phi(1-S_w)[K_g\,(n_{max} - n_f)\,\Psi_s - K_d\, n_f], \tag{5.4}$$

$$\Psi_s = \Psi_s(C_s) = \begin{cases} C_s(2\widehat{C}_{cmc} - C_s)/(\widehat{C}_{cmc}^2) & \text{if } \; C_s \le \widehat{C}_{cmc}, \\ 1 & \text{if } \; C_s > \widehat{C}_{cmc}, \end{cases} \tag{5.5}$$

where K_g [s^{-1}] is the bubble generation coefficient, K_d [s^{-1}] is the bubble coalescence coefficient, and $\widehat{C}_{cmc}$ [mole/m^3] is the critical micelle concentration. In the equations above, ϕ [$\cdot$] is the porosity, u [m/s] is the total Darcy velocity, f_w [$\cdot$] is the water fractional flow, λ_g [m^2/Pa s] is the relative mobility of gas, P_c [Pa] is the capillary pressure, n_{max} [m^{-3}] is the maximum bubble density and $\hat{\alpha}$ [mole] is the surfactant amount in one average *lamellae*. The following variables depend on space x [m] and time $t \ge 0$ [s]: S_w [$\cdot$] is the water saturation, n_f [m^{-3}] is the dimensional foam texture and C_s [mole/m^3] is the surfactant concentration.

To complete model (5.1)-(5.3), we use the standard fractional flow theory functions presented in [12, 21] as it used in Chapter 4. The total Darcy velocity is $u = u_w + u_g$, u_w is water velocity, and u_g is gas velocity. The water fractional flow and relative mobilities are defined in Section (2.1). The water phase relative permeability k_{rw} is given in (4.4). The foam-free gas relative permeability k_{rg}^0 is given in (4.6). The foamed gas phase relative permeability k_{rg} is given by

$$k_{rg}(S_w, n_f) = \frac{k_{rg}^0(S_w)}{MRF(n_f)}. \tag{5.6}$$

The foam Mobility Reduction Factor, following the approach in [3], is given by

$$MRF(n_f) = \beta\, n_f + 1, \tag{5.7}$$

where $\beta = \alpha^0/((v_f)^d\, \mu_g^0)$ is a constant estimated, in Chapter 4, with the approximate foam velocity $v_f = u_g/(\phi S_g)$ and α^0 a viscosity proportionality constant. In this chapter, we use the capillary pressure is given in (4.7), [74].

We estimate the parameter value $\hat{\alpha}$ in Eq. (5.3) as ($4{\cdot}10^{-5}$[mole]) by using the bubble surface area ($1.26 \cdot 10^{-11}\mathrm{m}^2$), bubble thickness (100Å) and molar density of surfactant $(250\,\mathrm{ml/mole})^{-1}$.

5.1.1 Equilibrium foam texture as function of surfactant concentration

The choice of the function Ψ_s describing foam texture equilibrium dependence on surfactant concentration presented in this chapter (see (5.5)) allows the mathematical analysis presented in the next sections. In this section, we show that it corresponds to qualitatively the same mobility reduction factor as existing and widely used formulas.

Notice that, the foam generation source term Q, defined in (5.4), can be rewritten as

$$Q = \phi(1 - S_w)(K_g + K_d)(n_f^{LE} - n_f), \quad n_f^{LE} = n_f^{LE}(C_s) = \frac{K_g\, n_{max}\, \Psi_s}{K_g\, \Psi_s + K_d}, \tag{5.8}$$

such that n_f^{LE} is the dimensional foam texture in local equilibrium with Ψ_s given by Eq. (5.5). The gas mobility λ_g depends on the Mobility Reduction Factor MRF as [3, 89]

$$\lambda_g = \frac{k}{\mu_g}\frac{k_{rg}^0}{MRF} = \frac{\lambda_g^0}{MRF} = \frac{\lambda_g^0}{1 + \beta\, n_f}, \tag{5.9}$$

where λ_g^0 is the gas mobility in the absence of foam. The MRF on Steady-State is given by $1 + \beta\, n_f^{LE}$.

In the model implemented in CMG/STARS simulator [22, 43, 60, 93], the gas mobility λ_g is modified by multiplying a Mobility Factor MF obtaining

$$\lambda_g = \lambda_g^0\, MF = \frac{\lambda_g^0}{1 + fmmob\, F_1}, \tag{5.10}$$

where $fmmob$ is the maximum mobility-reduction factor. Function F_1 represents the effect of surfactant concentration given by

$$F_1 = F_1(C_s) = \begin{cases} \left(\dfrac{C_s}{fmsurf}\right)^{epsurf} & \text{if} \quad C_s < fmsurf, \\ 1 & \text{if} \quad C_s \geq fmsurf, \end{cases} \tag{5.11}$$

where $fmsurf$ is the critical surfactant concentration above which gas mobility is independent of the surfactant concentration, and $epsurf$ is a parameter that regulates the foam strength for surfactant concentrations below $fmsurf$.

Figure 31 shows that MRF and MF^{-1} functions present an excellent agreement.

5.2 DIMESIONLESS DIFFERENTIAL EQUATIONS

We introduce the following dimensionless dependent and independent variables as ratios of the dimensional quantities and reference quantities (denoted by stars):

$$\widetilde{x} = \frac{x}{x^*}, \quad \widetilde{t} = \frac{t}{t^*}, \quad n_D = \frac{n_f}{n^*}, \quad \text{and} \quad C = \frac{C_s}{C^*}, \tag{5.12}$$

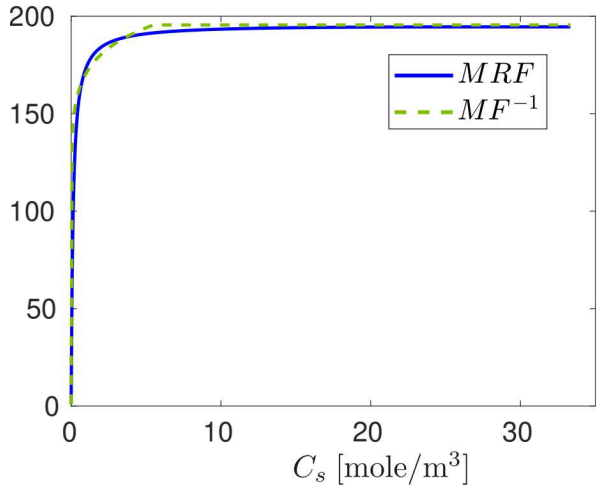

Figura 31 – Comparison between the functions MRF and MF^{-1} corresponding to the population balance model proposed in this chapter under LE conditions and the model implemented in CMG/STARS simulator.

where C^* is the maximum surfactant concentration yielding $0 \leq C \leq 1$. The other reference quantities are defined by

$$n^* = n_{max}, \quad x^* = L, \quad \text{and} \quad t^* = \frac{\phi L}{u}, \tag{5.13}$$

where L is the core length.

Remark 5.2.1. In order to estimate C^*, we use the following parameters [74]: surfactant density 1.05 g/cm^3, molecular weight 315 g/mole, and solution concentration 1 w/w % = 1g/100g. The molar concentration of surfactant in a solution can be approximated as C^*= 33.33 [mole/m^3].

Using (5.12) and (5.13), and omitting the tildes, System (5.1)-(5.3) becomes the dimensionless System (5.14)-(5.16):

$$\frac{\partial S_w}{\partial t} + \frac{\partial f_w}{\partial x} + \frac{\partial}{\partial x}\left(\delta f_w \lambda_g \frac{dP_c}{dS_w}\frac{\partial S_w}{\partial x}\right) = 0, \tag{5.14}$$

$$\frac{\partial((1-S_w)n_D)}{\partial t} + \frac{\partial((1-f_w)n_D)}{\partial x} - \frac{\partial}{\partial x}\left(\delta f \lambda_g \frac{dP_c}{dS_w}\frac{\partial S_w}{\partial x} n_D\right) = \Phi, \tag{5.15}$$

$$\frac{\partial(S_w C)}{\partial t} + \frac{\partial(f_w C)}{\partial x} + \frac{\partial}{\partial x}\left(\delta f \lambda_g \frac{dP_c}{dS_w}\frac{\partial S_w}{\partial x} C\right) = -\alpha\,\Phi, \tag{5.16}$$

where $\delta = 1/(u\,L)$, $\alpha = \hat{\alpha}\, n_{max}/C^*$, and

$$\Phi = \frac{L\,Q}{u\,n_{max}} = \frac{L\phi}{u}(1-S_w)(K_g\,(1-n_D)\,\Psi - K_d\,n_D). \tag{5.17}$$

We can rewrite Φ as

$$\Phi = \frac{L\phi}{u}(1-S_w)(K_g + K_d)(n_D^{LE} - n_D), \quad n_D^{LE} = \frac{K_g\,\Psi}{K_g\,\Psi + K_d}, \tag{5.18}$$

such that n_D^{LE} is the foam texture in local equilibrium with Ψ given by

$$\Psi = \Psi(C) = \begin{cases} C(2C_{cmc} - C)/(C_{cmc}^2) & \text{if } C \leq C_{cmc}, \\ 1 & \text{if } C > C_{cmc}, \end{cases} \tag{5.19}$$

where $C_{cmc} = \widehat{C}_{cmc}/C^*$.

In what follows, we will search for the solution of System (5.14)-(5.16) with a step function type initial conditions:

$$(S_w, n_D, C)(x, 0) = \begin{cases} (S_w^-, n_D^-, C^-) & \text{if } x < 0, \\ (S_w^+, n_D^+, C^+) & \text{if } x > 0. \end{cases} \tag{5.20}$$

The problem (5.14)-(5.16), (5.20) is known as Riemann problem. The superscripts "$-$" and "$+$" mean that the variable is evaluated at conditions upstream (or injection condition) and downstream (or initial reservoir condition) of the wave, corresponding to left and right states, respectively.

In the following sections, we present a semi-analytical investigation of the traveling wave solution of (5.14)-(5.16), (5.20) with parameter values from Table 4.

Tabela 4 – Parameter values used in this chapter. These values are obtained from [74, 89].

Symbol	*Parameter*	*Values*
ϕ [-]	Porosity	0.21
u [m/s]	Total Darcy velocity	$1.6156 \cdot 10^{-5}$
u_w [m/s]	Water velocity	$1.446 \cdot 10^{-6}$
u_g [m/s]	Gas velocity	$1.471 \cdot 10^{-5}$
$\hat{\alpha}$ [mole]	Surfactant per *lamellae*	$4 \cdot 10^{-5}$
K_g [s^{-1}]	Bubble generation coefficient	0.1
K_d [s^{-1}]	Bubble destruction coefficient	0.05
n_{max} [m^{-3}]	Maximum bubble density	$2.5 \cdot 10^{11}$
C^* [mole/m^3]	Maximum surfactant concentration	33.33
C_{cmc} [mole/m^3]	Critical micelle concentration	0.8
k [m^2]	Absolute permeability	$2.5 \cdot 10^{-12}$
S_{wc} [-]	Connate water saturation	0.10
S_{gr} [-]	Residual gas saturation	0.0
μ_w [Pa s]	Water viscosity	$1.0 \cdot 10^{-3}$
μ_g [Pa s]	Gas viscosity	$1.8 \cdot 10^{-5}$
β [m^3]	Non-Newtonian mobility param.	$7.8185 \cdot 10^{-10}$
α^0 [Pa $\mathrm{s}^{2/3}$ $\mathrm{m}^{10/3}$]	Viscosity proportionality const.	$5.8 \cdot 10^{-16}$

5.3 TRAVELING WAVE FORMULATION

The system of partial differential equations (5.14)-(5.16) admits a traveling wave solution if, similarly to definition presented in Section 2.5, by considering traveling variable $(x, t) \longrightarrow (\xi = x - vt, t)$ with $S_w(\xi, t) = \widetilde{S}_w(x - vt, t)$, $n_D(\xi, t) = \widetilde{n}_D(x - vt, t)$ and $C(\xi, t) = \widetilde{C}(x - vt, t)$ there is a solution for the system of ordinary differential equations (5.22)-(5.24)

obtained from this transformation, which propagates with a constant velocity $v > 0$ and satisfies asymptotic conditions

$$\begin{aligned} &\lim_{\xi\to\pm\infty}(\widetilde{S}_w, \widetilde{n}_D, \widetilde{C})(\xi) = (S_w^{\pm}, n_D^{\pm}, C^{\pm}),\\ &\lim_{\xi\to\pm\infty}\left(\frac{d\widetilde{S}_w}{d\xi}, \frac{d\widetilde{n}_D}{d\xi}, \frac{d\widetilde{C}}{d\xi}\right)(\xi) = (0,0,0). \end{aligned} \tag{5.21}$$

For a more detailed explanation please see [56, 84]. Applying the traveling wave variables, System (5.14)-(5.16) is rewritten (omitting the tildes) as

$$-v\frac{dS_w}{d\xi} + \frac{df_w}{d\xi} + \frac{d}{d\xi}\left(\delta f_w \lambda_g \frac{dP_c}{dS_w}\frac{dS_w}{d\xi}\right) = 0, \tag{5.22}$$

$$-v\frac{d((1-S_w)n_D)}{d\xi} + \frac{d((1-f_w)n_D)}{d\xi} - \frac{d}{d\xi}\left(\delta f_w \lambda_g \frac{dP_c}{dS_w}\frac{dS_w}{d\xi} n_D\right) = \Phi, \tag{5.23}$$

$$-v\frac{d(S_w C)}{d\xi} + \frac{d(f_w C)}{d\xi} + \frac{d}{d\xi}\left(\delta f_w \lambda_g \frac{dP_c}{dS_w}\frac{dS_w}{d\xi} C\right) = -\alpha\,\Phi. \tag{5.24}$$

Integration of Eq. (5.22) results in the following expression

$$-v\,S_w + f_w + \delta\lambda_g f_w \frac{dP_c}{dS_w}\frac{dS_w}{d\xi} = -vS_w^- + f_w^- = -vS_w^+ + f_w^+. \tag{5.25}$$

From (5.25), we obtain the velocity of the traveling wave

$$v = \frac{f_w^- - f_w^+}{S_w^- - S_w^+} \tag{5.26}$$

and

$$\delta\lambda_g f_w \frac{dP_c}{dS_w}\frac{dS_w}{d\xi} = v(S_w - S_w^+) + f_w^+ - f_w. \tag{5.27}$$

On the other hand, using (5.25), equations (5.23) and (5.24) can be rewritten as

$$(-v(1-S_w)^+ + (1-f_w)^+)\frac{dn_D}{d\xi} = \Phi, \tag{5.28}$$

$$(-vS_w^+ + f_w^+)\frac{dC}{d\xi} = -\alpha\,\Phi. \tag{5.29}$$

Furthermore, if we sum Eq. (5.29) to the product of (5.28) and α yields:

$$\alpha(-v(1-S_w)^+ + (1-f_w)^+)\frac{dn_D}{d\xi} + (-vS_w^+ + f_w^+)\frac{dC}{d\xi} = 0. \tag{5.30}$$

Then, integrating (5.30) from ξ to $\xi \to \infty$, follows that

$$-\alpha(-v(1-S_w^+) + (1-f_w^+))\,(n_D - n_D^+) = (-vS_w^+ + f_w^+)\,(C - C^+). \tag{5.31}$$

If we integrate (5.30) from $\xi \to -\infty$ to $\xi \to \infty$, results in

$$-\alpha(-v(1-S_w^+) + (1-f_w^+))\,(n_D^- - n_D^+) = (-vS_w^+ + f_w^+)\,(C^- - C^+). \tag{5.32}$$

From (5.27) and (5.29), System (5.22)-(5.24) becomes two ordinary differential equations:

$$\left(\delta\lambda_g f_w \frac{dP_c}{dS_w}\right)\frac{dS_w}{d\xi} = v(S_w - S_w^+) + f_w^+ - f_w, \tag{5.33}$$

$$(-vS_w^+ + f_w^+)\frac{dC}{d\xi} = -\alpha(L/u)\phi(1-S_w)[K_g\,(1-n_D)\,\Psi - K_d\,n_D], \tag{5.34}$$

where n_D satisfies the expression (5.31) and the traveling wave velocity v is given in (5.26). In what follows we analyze two cases:

- Assuming $-vS_w^+ + f_w^+ \neq 0$, System (5.33)-(5.34) can be rewritten in the standard form:

$$\frac{dS_w}{d\xi} = \frac{v(S_w - S_w^+) + (f_w^+ - f_w)}{\delta\lambda_g f_w \dfrac{dP_c}{dS_w}}, \tag{5.35}$$

$$\frac{dC}{d\xi} = \frac{-\alpha(L/u)\phi(1-S_w)[K_g\,(1-n_D)\,\Psi - K_d\,n_D]}{-vS_w^+ + f_w^+}, \tag{5.36}$$

$$n_D = \frac{(-vS_w^+ + f_w^+)\,(C - C^+)}{-\alpha(-v(1-S_w^+) + (1-f_w^+))} + n_D^+, \tag{5.37}$$

  where the traveling wave velocity v is given in (5.26).

- In the case $-vS_w^+ + f_w^+ = 0$, System (5.33)-(5.34) becomes

$$\frac{dS_w}{d\xi} = \frac{v(S_w - S_w^+) + f_w^+ - f_w}{\delta\lambda_g f_w \dfrac{dP_c}{dS_w}}, \tag{5.38}$$

$$K_g\,(1-n_D)\,\Psi(C) - K_d\,n_D = 0, \tag{5.39}$$

$$n_D = n_D^+, \tag{5.40}$$

  where the traveling wave velocity v is given in (5.26).

Proposition 5.3.1. *For the case, $-vS_w^+ + f_w^+ = 0$, the solution of System* (5.33)-(5.34) *corresponds to constant surfactant concentration.*

Proof: In this case, System (5.33)-(5.34) reads as System (5.38)-(5.40). From (5.40), it follows that $n_D = n_D^+ = n_D^{LE}(C^+)$ is a constant. Denoting

$$T_s = -v\,S_w + f_w + \delta\lambda_g f_w \frac{dP_c}{dS_w}\frac{dS_w}{d\xi}, \tag{5.41}$$

Equation (5.24) is rewritten as

$$\frac{d\,(T_s\,C)}{d\xi} = -\alpha\,\Phi. \tag{5.42}$$

As n_D is constant, it follows that $\Phi = 0$. Applying the chain rule yields

$$\frac{d\,T_s}{d\xi}C + T_s\,\frac{d\,C}{d\xi} = 0. \tag{5.43}$$

Using (5.22) and (5.25), it follows that $(dT_s/d\xi) = 0$ and consequently T_s is constant. Using (5.43) yields C is constant.

□

5.3.1 Equilibria of system of ordinary differential equation

In general, the equilibria of a system of ODEs are points that turn the flux functions equal to zero [34, 76]. In case $-vS_w^+ + f_w^+ \neq 0$, the equilibria of System (5.35)-(5.37) are the points (S_w, C) that turn the right side of (5.35) and (5.36) equal to zero.

In this chapter, we fix $S_w^+ = 0.94$ corresponding to the drainage case and consider $0 < C < 1$. We fix C^- and C^+ searching for possible values of S_w^-, n_D^-, and n_D^+, such that (S_w^-, C^-) and (S_w^+, C^+) are equilibria of System (5.35)-(5.37). The left equilibrium (S_w^-, C^-) corresponds to the injection conditions (left state, see (5.20)) and right equilibrium (S_w^+, C^+) corresponds to initial reservoir conditions (right state, see (5.20)). Calculating the limits $\xi \to \pm\infty$ of the right side of (5.36), the values $S_w^\pm$, $n_D^\pm$, and $C^\pm$ are related to each other:

$$n_D^\pm = n_D^{LE}(C^\pm) = \frac{K_g\,\Psi^\pm}{K_g\,\Psi^\pm + K_d}, \qquad \Psi^\pm = \Psi(C^\pm). \tag{5.44}$$

Notice that if $C^- \neq C^+$, using relation (5.32), the velocity v of the traveling wave can be rewritten independently of S_w^-:

$$v = \frac{\alpha(1 - f_w^+)(n_D^- - n_D^+) + f_w^+\,(C^- - C^+)}{\alpha(1 - S_w^+)(n_D^- - n_D^+) + S_w^+\,(C^- - C^+)}. \tag{5.45}$$

Calculating the limits $\xi \to \pm\infty$ of the right side of (5.35) an equilibrium (S_w^-, C^-) satisfies

$$f_w(S_w^-, C^-) = f_w^+ - v(S_w^+ - S_w^-), \tag{5.46}$$

meaning that S_w^- stays on the intersection between $f_w(S_w, C^-)$ and the straight line passing through point (S_w^+, f_w^+) with slope v from (5.45), see Figure 32. In Eq. (5.46) we abused of notation indicating $f_w(S_w, C) = f_w(S_w, n_D^{LE}(C))$; this notation will be used henceforth. Figure 32 also shows $f_w(S_w, C)$ for different values of C as function of S_w. Notice that other equilibria (when they exist) are found at this intersection. Varying C^- and C^+, we notice that the velocity of traveling wave v changes yielding different possibilities of S_w^-. Thus we classify the parameter space $C^- \times C^+$, as shown in Figure 33, in regions with different equilibria quantities and their properties. Also, the quantity and type of equilibrium points change in the boundaries of regions. Thus, we divide the parameter space as

$$C^- \times C^+ = \mathfrak{R}^1 \cup \mathfrak{R}^2 \cup \mathfrak{R}^3 \cup \mathfrak{R}^4 \cup \mathfrak{R}^5 \cup \mathfrak{R}^6 \cup \mathfrak{R}^7 \cup \mathfrak{L} \cup \mathfrak{N} \cup \mathfrak{T} \cup \mathfrak{D}. \tag{5.47}$$

The boundaries between the regions are:

- Curve $\mathfrak{L}$ contains the points (C^-, C^+) such that $v = v^L$, where v^L is the slope of the tangent line to $f_w(S_w, C^-)$ that passes through the point (S_w^+, f_w^+) with $S_w^l < S_w^+$ as shown in Figure 34(a). The tangent point is $f_w(S_w^l, C^-)$.

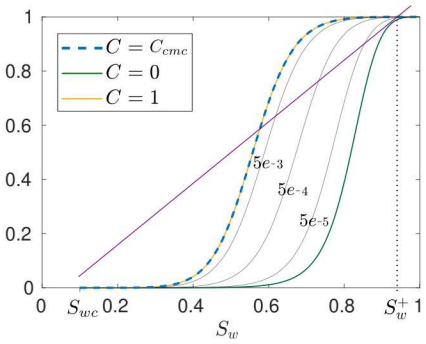

Figura 32 – Water fractional flow for different values of C for the case $C_{cmc} = 0.8$. The vertical dotted line corresponds to $S_w^+ = 0.94$. The purple line passes through the point (S_w^+, f_w^+) with slope v.

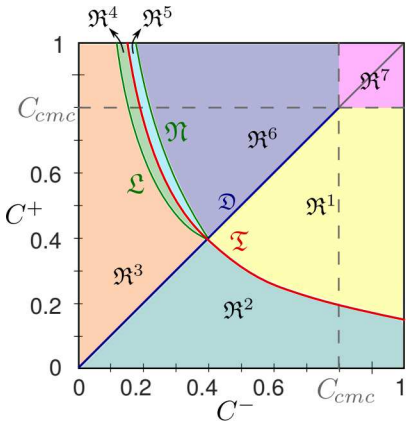

Figura 33 – The parameter space $C^- \times C^+$ divided into regions with different equilibria quantities and their properties. We used $S_w^+ = 0.94$.

- Curve $\mathfrak{N}$ contains the points (C^-, C^+) such that $v = v^N$, where v^N is the slope of the tangent line to $f_w(S_w, C^-)$ that passes through the point (S_w^+, f_w^+) with $S_w^l > S_w^+$ as shown in Figure 34(b). The tangent point is $f_w(S_w^l, C^-)$.

- Curve $\mathfrak{T}$ contains the points (C^-, C^+) such that $v = v^\tau$, where v^τ is the slope of the tangent line to $f_w(S_w, C^+)$ through (S_w^+, f_w^+) given by

$$v^\tau = \frac{df_w}{dS_w}(S_w^+, C^+), \tag{5.48}$$

  see Figure 35.

- Curve $\mathfrak{D}$ contains the points (C^-, C^+) such that $C^- = C^+$ and $C^- < C_{cmc}$.

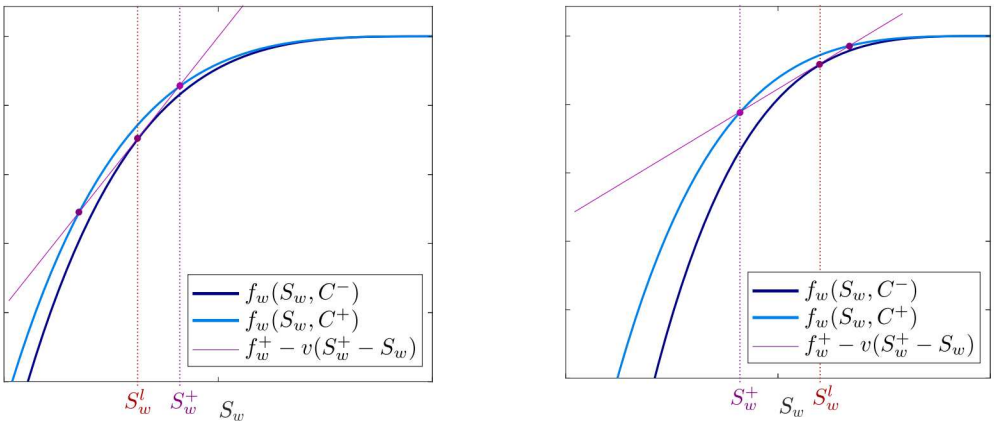

Figura 34 – Intersection between $f_w(S_w, C^-)$ and the straight line that passes through point (S_w^+, f_w^+) with slope v. The value S_w^l coincides with S_w^-. The purple line passes through the point (S_w^+, f_w^+) with slope v. (a) $v = v^L$ and $S_w^l < S_w^+$. (b) $v = v^N$ and $S_w^l > S_w^+$.

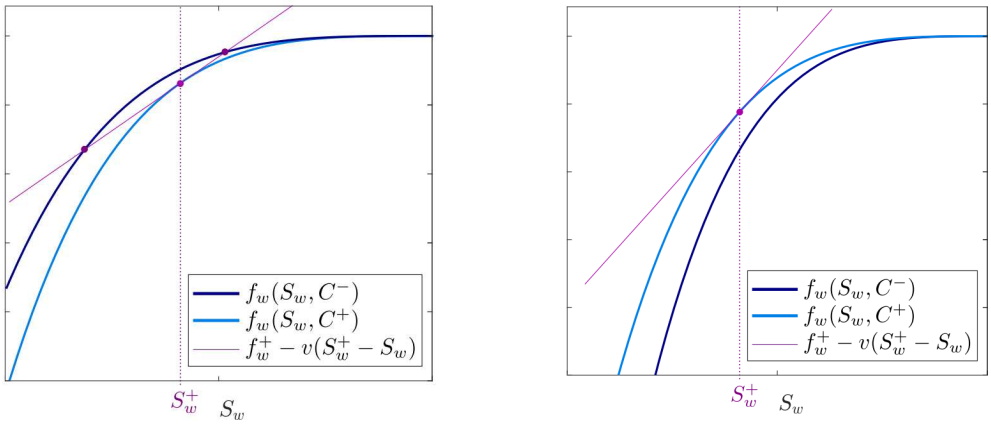

Figura 35 – Intersection between $f_w(S_w, C^-)$ and the straight line that passes through point (S_w^+, f_w^+) with slope v. The value S_w^τ coincides with S_w^-. The purple line passes through the point (S_w^+, f_w^+) with slope v. (a) $v = v^\tau$ and $C^+ < C^-$. (b) $v = v^\tau$ and $C^+ > C^-$.

The regions are:

$$
\begin{aligned}
\mathfrak{R}^1 &= \{(C^-, C^+):\ 0 < C^- < 1;\ C^+ < C_{cmc};\ C^- > C^+;\ v > v^\tau\},\\
\mathfrak{R}^2 &= \{(C^-, C^+):\ 0 < C^- < 1;\ C^- > C^+;\ v < v^\tau\},\\
\mathfrak{R}^3 &= \{(C^-, C^+):\ 0 < C^+ < 1;\ C^- < C^+;\ v < v^L\},\\
\mathfrak{R}^4 &= \{(C^-, C^+):\ 0 < C^+ < 1;\ C^- < C^+;\ v^L < v < v^\tau\},\\
\mathfrak{R}^5 &= \{(C^-, C^+):\ 0 < C^+ < 1;\ C^- < C^+;\ v^\tau < v < v^N\},\\
\mathfrak{R}^6 &= \{(C^-, C^+):\ 0 < C^+ < 1;\ C^- < C_{cmc};\ C^- < C^+;\ v^N < v\},\\
\mathfrak{R}^7 &= \{(C^-, C^+):\ C_{cmc} \leq C^- < 1;\ C_{cmc} \leq C^+ < 1\}.
\end{aligned}
\tag{5.49}
$$

Different regions correspond to the different quantities of possible equilibria:

- For regions $\mathfrak{R}^1$, $\mathfrak{R}^2$, $\mathfrak{R}^3$, and $\mathfrak{R}^6$: In intersection between $f_w(S_w, C^-)$ and the straight line that passes through point (S_w^+, f_w^+) with slope v, there are two equilibria in $f_w(S_w, C^-)$. So, we obtain two possibilities for S_w^-.
- For regions $\mathfrak{R}^4$, $\mathfrak{R}^5$, and $\mathfrak{T}$ if $C^- < C^+$: In intersection between $f_w(S_w, C^-)$ and the straight line that passes through point (S_w^+, f_w^+) with slope v, there is no equilibrium in $f_w(S_w, C^-)$. So, there is no possible S_w^-.
- For curves $\mathfrak{L}$, $\mathfrak{N}$, and $\mathfrak{T}$ if $C^- > C^+$: In intersection between $f_w(S_w, C^-)$ and the straight line that passes through point (S_w^+, f_w^+) with slope v, there is one equilibrium in $f_w(S_w, C^-)$. So, we obtain only one possibility for S_w^-.
- For $\mathfrak{R}^7$ and $\mathfrak{D}$: The point (S_w^-, C_s^-) is equilibrium for all values of $S_w^- \in (S_{wc}, 1 - S_{gr})$.

Notice that, $C^- \neq C^+$ in regions $\mathfrak{R}^1$, $\mathfrak{R}^2$, $\mathfrak{R}^3$, $\mathfrak{R}^4$, $\mathfrak{R}^5$, $\mathfrak{R}^6$, $\mathfrak{L}$, $\mathfrak{N}$, and $\mathfrak{T}$. Thus, in these regions v is calculated using (5.45) and, according to Proposition 5.3.1, $-vS_w^+ + f_w^+ \neq 0$.

On the other side, in $\mathfrak{R}^7$ and $\mathfrak{D}$, it is possible to have $C^- = C^+$, and v is calculated using (5.26).

Remark 5.3.1. Notice that, in general, the straight line with slope v that passes through (S_w^+, f_w^+) may intersect the two fractional functions at up to six points, including (S_w^+, f_w^+). However, fixing $S_w^+ = 0.94$, we only have up to four equilibrium points. For example, Figure 36 shows the case $(C^-, C^+) \in \mathfrak{R}^1$.

The equilibrium points can be classified according to the eigenvalue signs of the corresponding flux's Jacobian as a source, a sink, a saddle, or a node; see [34, 76] for details. In two-dimensional space, a source possesses two eigenvalues with positive real parts, a sink possesses two eigenvalues with negative real parts, a saddle possesses two eigenvalues with real parts of different signs, and a node possesses one null eigenvalue and another different from zero.

More specifically, the Jacobian of the flux associated with the vector field of System (5.35)-(5.36) is given by

$$J = \begin{bmatrix} \dfrac{\partial_s N^F\, D^F - N^F\, \partial_s D^F}{(D^F)^2} & \dfrac{\partial_c N^F\, D^F - N^F\, \partial_c D^F}{(D^F)^2} \\ \dfrac{-\alpha\, \partial_s \Phi}{-v\, S_w^+ + f_w^+} & \dfrac{-\alpha\, \partial_c \Phi}{-v\, S_w^+ + f_w^+} \end{bmatrix}, \tag{5.50}$$

where

$$N^F = v\,(S_w - S_w^+) + (f_w^+ - f_w), \qquad D^F = \delta\, \lambda_g\, f_w\, \partial_s P_c. \tag{5.51}$$

In the points (S_w^-, C^-) and (S_w^+, C^+), the matrix J is rewritten as:

$$M(\pm) = \begin{bmatrix} \dfrac{v - \partial_s f_w}{\delta\, \lambda_g\, f_w\, \partial_s P_c} & \dfrac{-\partial_n f_w\, d_c n_D}{\delta\, \lambda_g\, f_w\, \partial_s P_c} \\ 0 & \dfrac{-\alpha\, \partial_c \Phi}{-v\, S_w^+ + f_w^+} \end{bmatrix}_{(S_w^\pm, C^\pm)}. \tag{5.52}$$

Thus, the eigenvalues in (S_w^-, C^-) are

$$\lambda_1^- = \left.\frac{-\alpha\, \partial_c \Phi}{-v\, S_w^+ + f_w^+}\right|_{(S_w^-, C^-)} \qquad \lambda_2^- = \left.\frac{v - \partial_s f_w}{\delta\, \lambda_g\, f_w\, \partial_s P_c}\right|_{(S_w^-, C^-)}, \tag{5.53}$$

and the eigenvalues in (S_w^+, C^+) are

$$\lambda_1^+ = \left.\frac{-\alpha\, \partial_c \Phi}{-v\, S_w^+ + f_w^+}\right|_{(S_w^+, C^+)} \qquad \lambda_2^+ = \left.\frac{v - \partial_s f_w}{\delta\, \lambda_g\, f_w\, \partial_s P_c}\right|_{(S_w^+, C^+)}. \tag{5.54}$$

Notice that, the eigenvalues associated with left and right states are real.

As it was not possible to obtain the signs in (5.53) and (5.54) analytically, they were determined numerically. In the next section, we will use this information to determine the equilibria type for each region. A source (repeller) will be denoted by $P_{\mathcal{R}}$, a saddle by $P_{\mathcal{S}}$, and a sink (attractor) by $P_{\mathcal{A}}$.

5.4 EXISTENCE OF TRAVELING WAVE CONNECTION

The existence of the traveling wave solution of System (5.14)-(5.16) is directly related to the existence of the solution of System (5.33)-(5.34), which can be rewritten in two forms.

- If $-vS_w^+ + f_w^+ = 0$, using the Proposition 5.3.1, it follows that n_D and C are constants. Thus, this case exists only in Region $\mathfrak{R}^7$.
- For the case $-vS_w^+ + f_w^+ \neq 0$, we follow [56, 89] and study the phase portrait corresponding to System (5.35)-(5.37).

After knowing the number and type of equilibrium points in each region, we look for a *traveling wave connection*, defined as a solution of System (5.35)-(5.37) connecting the left equilibrium to the right one in the sense of $\alpha-$ and $\omega-$ limits as defined in (5.21).

To validate our analytical approximations, we compare them with numerical simulations of System (5.14)-(5.16) obtained using the nonlinear Crank-Nicolson implicit finite-difference scheme combined with Newton's method; see [50] for details. This scheme is second-order accurate both in space and time.

5.4.1 **Region $\mathfrak{R}^1$** ($C^- > C^+$ & $v > v^\tau$):

In this case, from Eq. (5.46) and calculating the eigenvalues' sign, there are four equilibria a source $P_{\mathcal{R}}$, a sink $P_{\mathcal{A}}$, and two saddles $P_{\mathcal{S}}^1$ and $P_{\mathcal{S}}^2$, as seen in Figure 36. Figure 36(a) shows all the equilibria located in the intersection of respective curves of water fractional flow and the line with slope v that passes through the point (S_w^+, f_w^+). Figure 36(b) shows the equilibria located in the phase portrait $S_w \times C$, where F_1 and F_2 represent the right sides of (5.35) and (5.36), respectively. In fact, the scheme presented in Figure 36(b) is valid in all regions ($\mathfrak{R}^1$, $\mathfrak{R}^2$, $\mathfrak{R}^3$, and $\mathfrak{R}^6$) with four equilibria.

In this region, since $C^- \neq C^+$ it follows that the left equilibrium (S_w^-, C^-) is on $f_w(S_w, C^-)$ and the right equilibrium (S_w^+, C^+) is on $f_w(S_w, C^+)$. As we fixed $S_w^+ = 0.94$, $P_{\mathcal{A}}$ corresponds to (S_w^+, C^+). The points $P_{\mathcal{R}}$ and $P_{\mathcal{S}}^1$ satisfy condition (5.46) to be the left equilibrium.

5.4.1.1 Case (S_w^-, C^-) is $P_{\mathcal{R}}$.

To obtain a traveling wave connecting the left equilibrium $P_{\mathcal{R}}$ to the right equilibrium $P_{\mathcal{A}}$, we use *ode45* of MATLAB. The source equilibrium $P_{\mathcal{R}}$ possesses two eigenvalues with a positive real part. Using the stable manifold theorem [34], the two-dimensional unstable manifold of (5.35)-(5.37) at $P_{\mathcal{R}}$ is tangent to the eigenvectors corresponding to the eigenvalues with a positive real part. Then, we start integrating from points close to

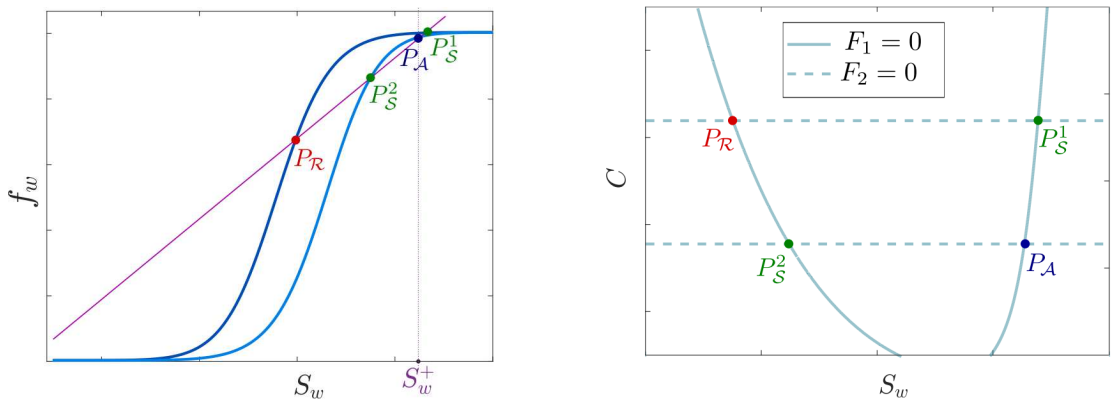

Figura 36 – Schematic representation showing the equilibrium points of System (5.35)-(5.37) in $\mathfrak{R}^1$. Point $P_{\mathcal{R}}$ represents a source, $P_{\mathcal{S}}$ represents a saddle, and $P_{\mathcal{A}}$ represents a sink. (a) Intersection between $f_w(S_w, C^-)$ and the straight line that passes through point (S_w^+, f_w^+) with slope v. The equilibrium points are placed on the purple solid line. (b) Equilibria in phase portrait $S_w \times C$. Functions F_1 and F_2 represent to right sides of (5.35) and (5.36).

the left state $P_{\mathcal{R}}$ on this unstable manifold. We integrate until reaching the neighborhood of the right equilibrium $P_{\mathcal{A}}$. For more details on this methodology, see [56].

If (S_w^-, C^-) is $P_{\mathcal{R}}$, there are infinite traveling wave connection of System (5.35)-(5.37) connecting the left equilibrium $P_{\mathcal{R}}$ to the right equilibrium $P_{\mathcal{A}}$; see Figure 37(a). From the mathematical perspective, it happens because the equilibria configuration separates the phase space into two regions: the inner and outer regions. The border that separates these two regions is composed of the stable and unstable manifolds of saddle equilibria connecting them with the other two equilibria; see Figure 37(a). For each point in the internal region of the phase space, there is a traveling wave connecting (S_w^-, C^-) to (S_w^+, C^+), satisfying the associated dynamic system (5.35)-(5.36), with the same velocity v.

The direct numerical simulation of System (5.14)-(5.16) produces a solution corresponding to the traveling wave connection passing close to point P_S^1, see the purple line in Figure 37(a). Figure 37(b) compares the analytical solution connecting $P_{\mathcal{R}}$ to $P_{\mathcal{S}}^1$ and then to $P_{\mathcal{A}}$ with the numerical simulation as a function of x. Thus, the system of partial differential equations points out that only one physically admissible traveling wave solution exists.

5.4.1.2 Case (S_w^-, C^-) is $P_{\mathcal{S}}^1$.

To obtain a traveling wave connection from the left equilibrium $P_{\mathcal{S}}^1$ to the right equilibrium $P_{\mathcal{A}}$, we use *ode45* of MATLAB. The saddle equilibrium $P_{\mathcal{S}}^1$ possesses one eigenvalue with a positive real part. Using the Stable Manifold Theorem [34], the one-dimensional unstable manifold of (5.35)-(5.37) at $P_{\mathcal{S}}^1$ is tangent to the eigenvector corresponding to the

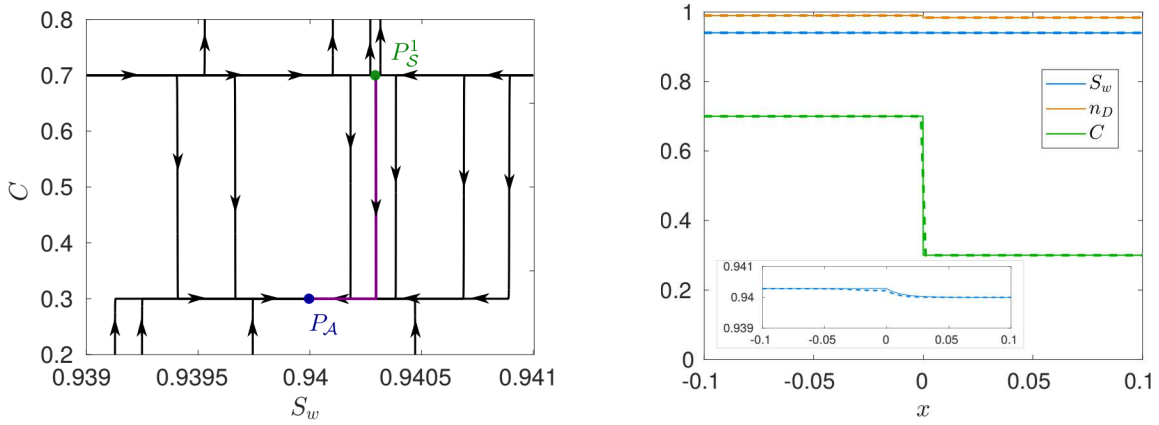

Figura 37 – Solution of System (5.35)-(5.37) for $(C^-, C^+) \in \mathfrak{R}^1$ with $(S_w^-, C^-) = P_{\mathcal{R}} = (0.92722, 0.7)$, $(S_w^+, C^+) = P_{\mathcal{A}} = (0.94, 0.3)$, and $v = 0.004538 > v^\tau = 0.003397$. (a) Analytical solution in the phase portrait. The purple line represents the traveling wave shown in Figure(b). (b) Solution profile. The solid line represents the analytical solution, and the dashed line corresponds to the numerical result.

eigenvalue with a positive real part. That is why, to obtain the traveling wave connection, we start integrating from a point close to the left state $P_{\mathcal{S}}^1$ in the direction of the eigenvector corresponding to the eigenvalue with a positive real part. We integrate until reaching the neighborhood of the right equilibrium $P_{\mathcal{A}}$. For more details on this methodology, see [56].

If (S_w^-, C^-) is $P_{\mathcal{S}}^1$, only one solution connects the left equilibrium to the right equilibrium. Figure 38(a) shows this connection in the phase space $S_w \times C$. The purple line corresponds to the numerical solution of the system of PDEs (5.14)-(5.16), and it almost coincides with the traveling wave connection. Figure 38(b) shows the agreement of analytical and numerical solutions as functions of x. As the variations in variables S_w and n_D are not visible in Figure 38(b), we plot them separately in Figs. 38(c) and 38(d).

5.4.2 **Region $\mathfrak{R}^2$** ($C^- > C^+$ & $v < v^\tau$):

Similarly to region $\mathfrak{R}^1$, there are four equilibria in the intersection between $f(S_w, C^-)$ and the line with slope v that passes through the point (S_w^+, f_w^+). Since $C^- \neq C^+$, it follows that $P_{\mathcal{S}}^2$ corresponds to (S_w^+, C^+). The points $P_{\mathcal{R}}$ and $P_{\mathcal{S}}^1$ satisfy conditions (5.46) to be the left equilibrium.

5.4.2.1 Case (S_w^-, C^-) is $P_{\mathcal{R}}$

To obtain a connection from source $P_{\mathcal{R}}$ to saddle $P_{\mathcal{S}}^2$, we use *ode45* of MATLAB, as in the case 5.4.1.2. The obtained connection corresponds to the analytical solution plotted in Figure 39(a), for $(S_w^-, C^-) = P_{\mathcal{R}} = (0.9356, 0.7)$. The equilibrium points are also plotted in phase portrait. Figure 39(b) compares the analytical solution and the numerically

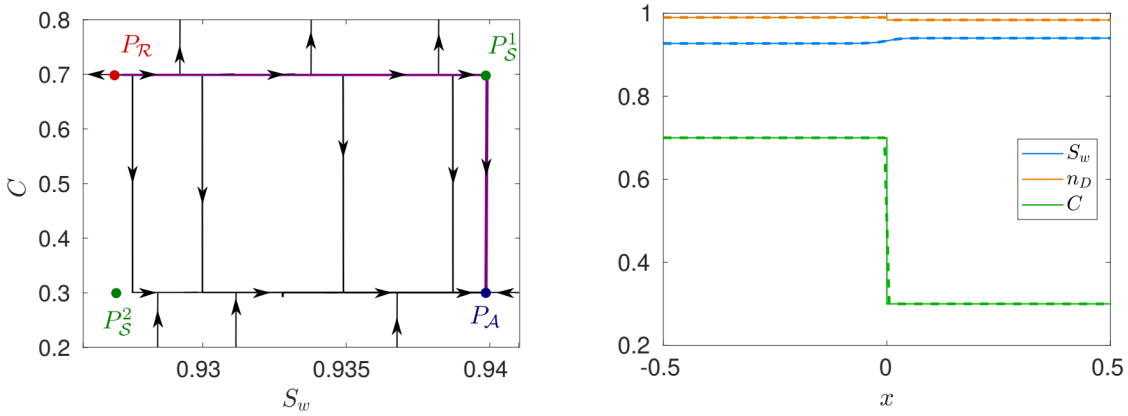

(a) (b)

Figura 38 – Solution of System (5.35)-(5.37) for $(C^-, C^+) \in \mathfrak{R}^1$ with $(S_w^-, C^-) = P_{\mathcal{S}}^1 = (0.94028, 0.7)$, $(S_w^+, C^+) = P_{\mathcal{A}} = (0.94, 0.3)$, and $v = 0.004538 > v^\tau = 0.003397$. (a) Analytical solution in the phase portrait. The purple line represents the traveling wave shown in Figure(b). (b) Solution profile. The solid line represents the analytical solution, and the dashed line corresponds to the numerical result.

obtained solution showing a good agreement. For this case, System (5.35)-(5.37) possesses a unique traveling wave.

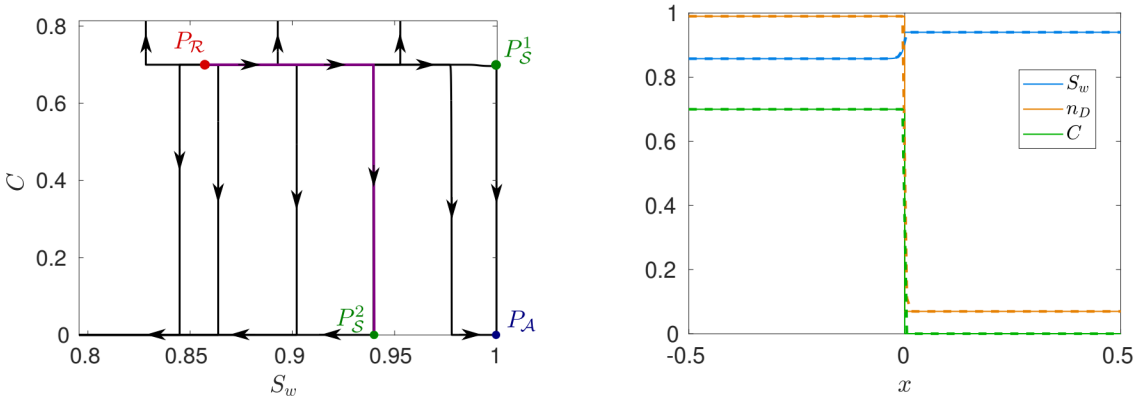

(a) (b)

Figura 39 – Solution of System (5.35)-(5.37) for $(C^-, C^+) \in \mathfrak{R}^2$ with $(S_w^+, C^+) = P_{\mathcal{S}}^2 = (0.94, 0.7)$ and $v = 0.004538 < v^\tau = 0.003397$. (a) Analytical solution in the phase portrait. The purple line represents the traveling wave. (b) Comparison between analytical (solid line) and numerical (dashed line) solution profiles.

5.4.2.2 Case (S_w^-, C^-) is $P_{\mathcal{S}}^1$

By using the same methodology as in case 5.4.1.2, the solutions obtained by integrating System (5.35)-(5.37) starting at a point close to equilibrium $P_{\mathcal{S}}^2$ for positive times reaching the neighborhood of $P_{\mathcal{A}}$ and for negative times reaching the neighborhood of $P_{\mathcal{R}}$; as seen in Figure 39. The solutions present the same behavior if we start integrating

at a point close to the right equilibrium $P_{\mathcal{S}}^2$. From the study of the phase portrait of System (5.35)-(5.37), the presence of the source $P_{\mathcal{R}}$ and of the sink $P_{\mathcal{A}}$ prohibit a direct connection from the left equilibrium to the right one. Then, when (S_w^-, C^-) is $P_{\mathcal{S}}^1$ there is no traveling wave solution of System (5.14)-(5.16).

5.4.3 **Region $\mathfrak{R}^3$** ($C^- < C^+$ & $v < v^L$):

This case is analogous to the regions $\mathfrak{R}^1$ and $\mathfrak{R}^2$. System (5.35)-(5.37) possesses four equilibria ($P_{\mathcal{R}}$, $P_{\mathcal{S}}^1$, $P_{\mathcal{S}}^2$, and $P_{\mathcal{A}}$), see Figure 36(b). Since $C^- \neq C^+$, it follows that $P_{\mathcal{R}}$ corresponds to (S_w^+, C^+). The points $P_{\mathcal{S}}^2$ and $P_{\mathcal{A}}$ satisfy conditions (5.46) to be the left equilibrium.

Similar to the case 5.4.1.1, the source equilibrium $P_{\mathcal{R}}$ possesses two eigenvalues with a positive real part. Using the stable manifold theorem [34], the two-dimensional unstable manifold of (5.35)-(5.37) at $P_{\mathcal{R}}$ is tangent to the eigenspace generated by eigenvectors corresponding to the eigenvalues with a positive real part. All traveling wave connections starting at a point in the neighborhood of the right equilibrium $P_{\mathcal{R}}$ move away from $P_{\mathcal{R}}$. Thus, there is no traveling wave connection starting in the left equilibrium and reaching the $P_{\mathcal{R}}$ for both possibilities of (S_w^-, C^-) (when the left equilibrium is $P_{\mathcal{S}}^2$ or $P_{\mathcal{A}}$). Therefore, there is no traveling wave of System (5.14)-(5.16).

5.4.4 **Region $\mathfrak{R}^4$** ($C^- < C^+$ & $v^L < v < v^\tau$) :

For this case, System (5.35)-(5.37) possesses two equilibria; both are on $f_w(S_w, C^+)$. Since $C^- \neq C^+$, the right equilibrium correspond to $P_{\mathcal{R}}$. There is no (S_w^-, C^-) that satisfies (5.46), see Figure 40(a). Therefore, there is no traveling wave connection.

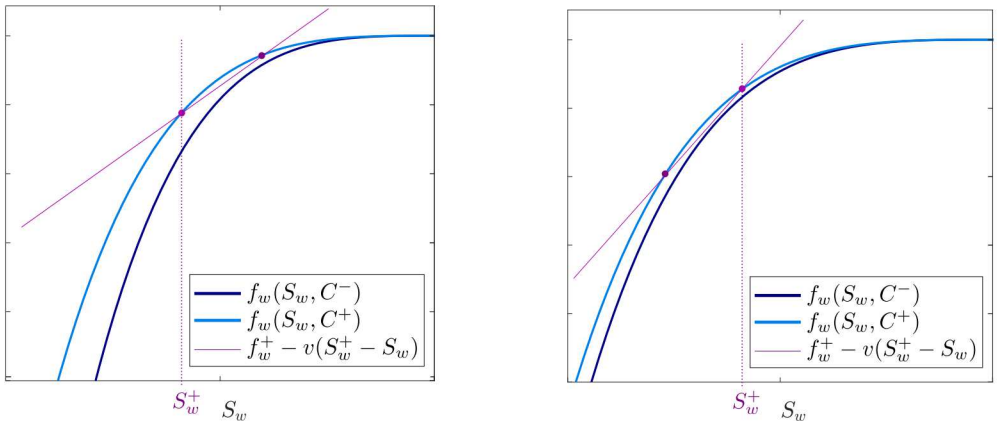

(a) (b)

Figura 40 – Equilibria in curves of water fractional flow for C^- and C^+. The purple line passes through the point (S_w^+, f_w^+) with slope v. (a) Case $(C^-, C^+) \in \mathfrak{R}^4$. (b) Case $(C^-, C^+) \in \mathfrak{R}^5$.

5.4.5 **Region $\mathfrak{R}^5$** ($C^- < C^+$ & $v^\tau < v < v^N$):

For this case, System (5.35)-(5.37) possesses only two equilibria; both on $f_w(S_w, C^+)$. Since $C^- \neq C^+$, the right equilibrium correspond to $P^1_{\mathcal{S}}$. There is no (S^-_w, C^-) that satisfies (5.46), see Figure 40(a). Therefore, there is no traveling wave connection.

5.4.6 **Region $\mathfrak{R}^6$** ($C^- < C^+$ & $v^N < v$):

Similarly to region $\mathfrak{R}^3$, there are four equilibria in the intersection between $f(S_w, C^-)$ and the line with slope v that passes through the point (S^+_w, f^+_w). Since $C^- \neq C^+$, it follows that saddle $P^1_{\mathcal{S}}$ corresponds to (S^+_w, C^+). The points $P^2_{\mathcal{S}}$ and $P_{\mathcal{A}}$ satisfy conditions (5.46) to be the left equilibrium.

5.4.6.1 Case (S^-_w, C^-) is $P^2_{\mathcal{S}}$

By using the same methodology as in case 5.4.2.2, from the study of the phase portrait of System (5.35)-(5.37), the presence of the source $P_{\mathcal{R}}$ and of the sink $P_{\mathcal{A}}$ prohibit a direct connection from the left equilibrium to the right one. Then, when (S^-_w, C^-) is $P^2_{\mathcal{S}}$ there is no traveling wave connection of System (5.14)-(5.16).

5.4.6.2 Case (S^-_w, C^-) is $P_{\mathcal{A}}$

Similarly to region $\mathfrak{R}^3$, all traveling wave connections start at a point in the neighborhood of left equilibrium $P_{\mathcal{A}}$ approach $P_{\mathcal{A}}$ (it is a sink). Thus, there is no traveling wave connection starting in $P_{\mathcal{A}}$ and reaching the $P^1_{\mathcal{S}}$. Therefore, since we only considered connections with direction, there is no traveling wave solution of System (5.14)-(5.16).

5.4.7 **Region $\mathfrak{R}^7$** ($C^- \geq C_{cmc}$ & $C^+ \geq C_{cmc}$):

In this case, using the relation (5.44), it follows that $n^-_D = n^+_D$. Then, from (5.32), $-vS^+_w + f^+_w = 0$ or $C^- = C^+$.

5.4.7.1 Case $-vS^+_w + f^+_w = 0$

From Proposition 5.3.1, n_D and C are constant. Therefore, for $-vS^+_w + f^+_w = 0$ and $C^- \neq C^+$, there is no traveling wave for this case.

5.4.7.2 Case $C^- = C^+$

In this case, an equilibrium (S_w, C) of System (5.35)-(5.37) satisfies

$$f_w(S_w, C^+) = v(S_w - S^+_w) + f^+_w, \tag{5.55}$$

and

$$n_D = n^{LE}_D(C^+) = K_g/(K_g + K_d). \tag{5.56}$$

Notice that $f_w(S_w, C^+)$ is the same for C^+ such that $C^+ \geq C_{cmc}$, as seen in Figure 32. Hence, S_w^- satisfies (5.55), and all equilibria of System (5.35)-(5.37) stay on the same $f(S_w, C^+)$, see Figure 41. In this case, the surfactant concentration does not affect the foam displacement, and the solution coincides with one presented in [89].

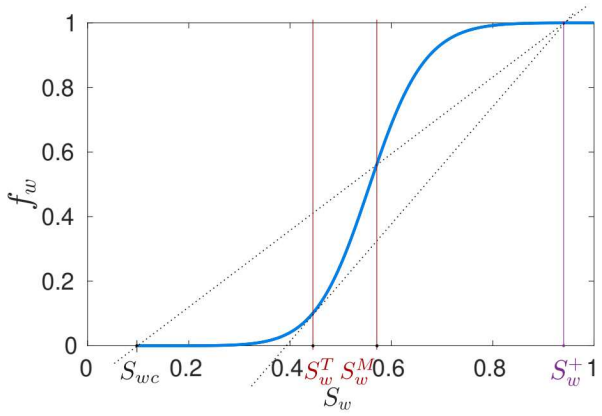

Figura 41 – Water fractional flow for $C > C_{cmc}$ corresponding to $\mathfrak{R}^7$. The dotted lines pass through (S_w^+, f_w^+). Value S_w^T corresponds the intersection point between $f_w(S_w, C^+)$ and the tangent line to $f_w(S_w, C^+)$ that passes through (S_w^+, f_w^+). Value S_w^M corresponds the intersection between $f_w(S_w, C^+)$ and the line connecting (S_{wc}, f_{wc}) to (S_w^+, f_w^+), where $f_{wc} = f_w(S_{wc}, C^+)$.

At the equilibria, $n_D = n_D^{LE}(C^+)$ is constant. Then, as in previous case using equations (5.41)-(5.43), it follows that $C = C^+ = C^-$ is constant. Let S_w^T indicate the intersection point between $f_w(S_w, C^+)$ and the tangent line to $f_w(S_w, C^+)$ that passes through (S_w^+, f_w^+). Value S_w^M indicates the intersection between $f_w(S_w, C^+)$ and the line connecting (S_{wc}, f_{wc}) to (S_w^+, f_w^+), where $f_{wc} = f_w(S_{wc}, C^+)$. Similarly to the results shown in the literature (see [32, 89] for details), it follows that the type of solution depends on S_w^- in relation to S_w^T and S_w^M, see Figure 41. There are five possibilities (for more details, see [89]):

(i) If $S_{wc} < S_w^- < S_w^T$. In this case, the left and right states of System (5.35)-(5.37) are saddle points. Besides, there exists a third equilibrium (S_w^e, C^+) satisfying $S_w^- < S_w^e < S_w^+$. Thus there is no direct connection from (S_w^-, C^+) to (S_w^+, C^+), and the solution is a sequence of two waves: one spreading wave connecting (S_w^-, C^+) to (S_w^T, C^+) and one traveling wave connecting (S_w^T, C^+) to (S_w^+, C^+), see Figure 42(a).

(ii) If $S_w^- = S_w^T$. When S_w^- approaches continuously to S_w^T, the eigenvalue λ_1^- tends to zero and S_w^e approaches S_w^T. In this case, there exist two equilibria (left and right). The left equilibrium (S_w^T, C^+) is a node with one positive and other zero eigenvalues, where the zero eigenvalue possesses one unstable and other stable sides. The right equilibrium (S_w^+, C^+) is a saddle. Here, there is a connection from one

of the unstable directions of the node (S_w^-, C^+) to the saddle (S_w^+, C^+). Therefore, there is a traveling wave solution, as shown in Figure 42(b).

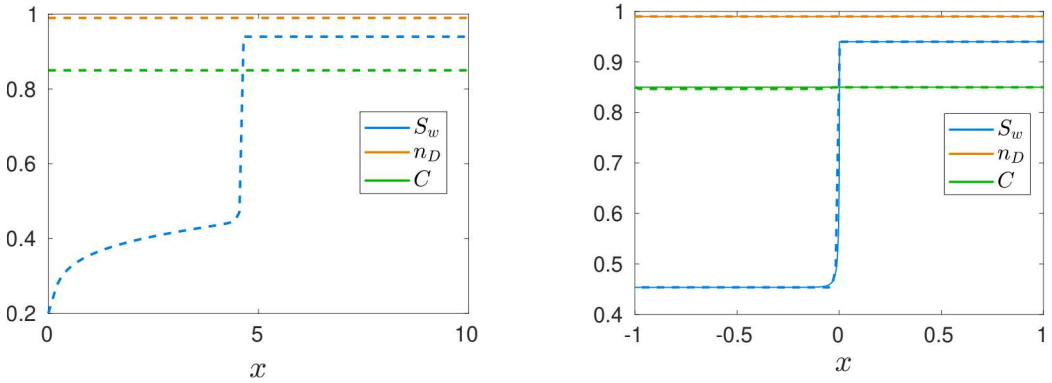

Figura 42 – Solution of System (5.35)-(5.37) for $(C^-, C^+) \in \mathfrak{R}^7$ for $(S_w^+, C^+) = (0.94, 0.85)$. The solid line represents the analytical solution, and the dashed line corresponds to the numerical simulation. (a) Case $S_{wc} < S_w^- < S_w^T$ with $S_w^- = 0.2$. (b) Case $S_w^- = S_w^T$.

(*iii*) If $S_w^T < S_w^- < S_w^M$. System (5.35)-(5.37) possesses three equilibria. The left sate (S_w^-, C^+) is a source, (S_w^+, C^+) is a saddle and the third equilibrium (S_w^e, C^+) is a saddle, where $S_{wc} < S_w^e < S_w^T$. There is a connection traveling wave as shown in Figure 43(a).

(*iv*) If $S_w^M < S_w^- < S_w^+$. There are only two equilibria: the left and right states, which are source and saddle. Hence, there exists a traveling wave solution from the left to the right state as shown in Figure 43(b).

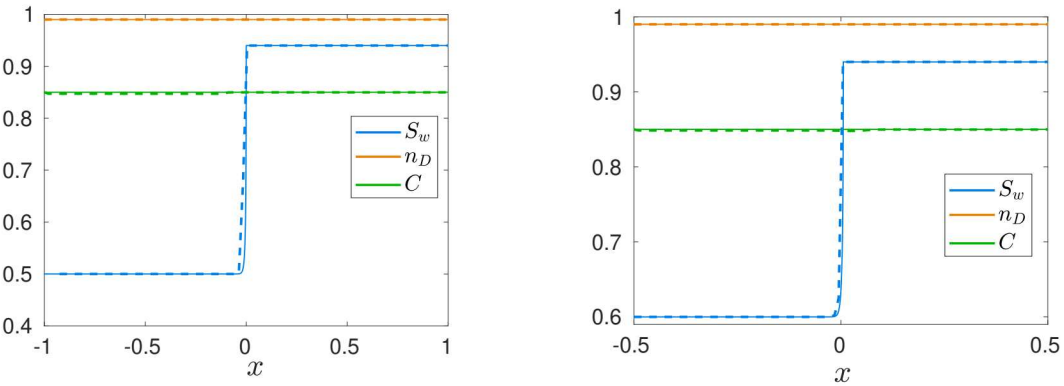

Figura 43 – Riemann problem solution of System (5.35)-(5.37) in Region $\mathfrak{R}^7$ for $(S_w^+, C^+) = (0.94, 0.85)$. The solid line represents the analytical solution, and the dashed line corresponds to the numerical simulation. (a) Case $S_w^T < S_w^- < S_w^M$ with $S_w^- = 0.5$. (b) Case $S_w^M < S_w^- < S_w^+$ with $S_w^- = 0.6$.

(v) If $S_w^+ < S_w^- < 1$. System (5.35)-(5.37) possesses two equilibria. The right equilibrium is a source, then there is no connection from the left equilibrium to the right one.

5.4.8 **Curve $\mathfrak{L}$** ($v = v^L$):

In this case, using Eq. (5.46) and eigenvalues signs, there are three equilibria: the source $P_{\mathcal{R}}$, the saddle $P_{\mathcal{S}}^1$, and the non-hyperbolic node equilibrium $P_{\mathcal{N}}$, which possesses one negative and other zero eigenvalues (the later corresponds to one stable and other unstable semi-manifolds). This later point appears from the collision of the equilibria $P_{\mathcal{S}}^2$ and $P_{\mathcal{A}}$ in Region $\mathfrak{R}^3$ and (differently from $P_{\mathcal{R}}$ and $P_{\mathcal{S}}^1$) it satisfies the condition (5.46).

Since $C^- \neq C^+$, the right equilibrium (S_w^+, C^+) is a source $P_{\mathcal{R}}$. Thus, the left equilibrium corresponds to $P_{\mathcal{N}}$. At the left equilibrium (S_w^-, C^-), the value $S_w^- = S_w^l$ corresponds to the tangent point of $f_w(S_w, C^-)$ that passes through the point (S_w^+, f_w^+) with $v = v^L$. Value v^L is the slope of the tangent line to $f_w(S_w, C^-)$ that passes through the point (S_w^+, f_w^+) with $S_w^l < S_w^+$ as shown in Figure 34(a).

As (S_w^+, C^+) is source $P_{\mathcal{R}}$, similarly to Region $\mathfrak{R}^3$, all traveling wave connections starting at a point in the neighborhood of right equilibrium $P_{\mathcal{R}}$ move away from $P_{\mathcal{R}}$, see Figure 44. Then, there is no traveling wave connection from $P_{\mathcal{N}}$ to $P_{\mathcal{R}}$.

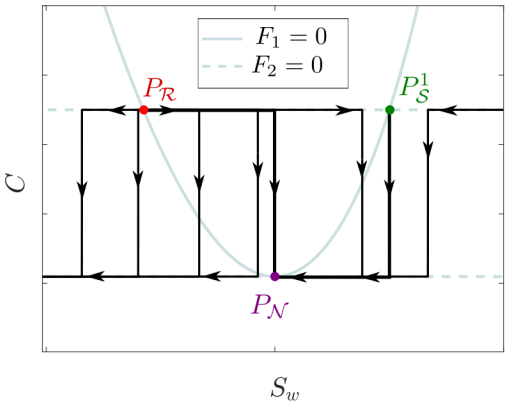

Figura 44 – Schematic phase portrait for regions $\mathfrak{L}$ and $\mathfrak{N}$. Functions F_1 and F_2 represent to right sides of (5.35) and (5.36), respectively.

5.4.9 **Curve $\mathfrak{N}$** ($v = v^N$):

Similarly to curve $\mathfrak{L}$, there are three equilibria: the source $P_{\mathcal{R}}$, the saddle $P_{\mathcal{S}}^1$, and the non-hyperbolic node equilibrium $P_{\mathcal{N}}$. Since $C^- \neq C^+$, the right equilibrium (S_w^+, C^+) is a source $P_{\mathcal{S}}^1$. Point $P_{\mathcal{N}}$ appears from the collision of equilibria $P_{\mathcal{S}}^2$ and $P_{\mathcal{A}}$ in Region $\mathfrak{R}^6$ and (differently from $P_{\mathcal{R}}$ and $P_{\mathcal{S}}^1$) it satisfies the condition (5.46). At the left equilibrium (S_w^-, C^-), the value $S_w^- = S_w^l$ corresponds to the tangent point of $f_w(S_w, C^-)$ that passes through the point (S_w^+, f_w^+) with $v = v^N$. Value v^N is the slope of the tangent

line to $f_w(S_w, C^-)$ that passes through the point (S_w^+, f_w^+) with $S_w^l > S_w^+$ as shown in Figure 34(b).

As (S_w^+, C^+) is saddle $P_{\mathcal{S}}^1$, similarly to Region $\mathfrak{R}^6$, it follows that there is no connection from left equilibrium $P_{\mathcal{N}}$ to $P_{\mathcal{S}}^1$. The phase portrait is schematically plotted in Figure 44.

5.4.10 **Curve $\mathfrak{T}$ ($v = v^\tau$):**

Let us study two cases.

5.4.10.1 Case $C^- > C^+$

Here $v = v^\tau$ and the equilibria $P_{\mathcal{S}}^2$ and $P_{\mathcal{A}}$ collapse into a non-hyperbolic node equilibrium $P_{\mathcal{N}}$. Since $C^- \neq C^+$, the right equilibrium (S_w^+, C^+) corresponds to saddle $P_{\mathcal{N}}$. The source $P_{\mathcal{R}}$ or the saddle $P_{\mathcal{S}}^1$ satisfy the condition (5.46), thus the left equilibrium can be the source $P_{\mathcal{R}}$ or the saddle $P_{\mathcal{S}}^1$, as seen in Figure 45.

- If (S_w^-, C^-) is $P_{\mathcal{R}}$ there is a traveling wave connection from $P_{\mathcal{R}}$ to $P_{\mathcal{N}}$ plotted as a red curve in Figure 45. Then, System (5.14)-(5.16) possesses a traveling wave solution, see Figure 46.
- If (S_w^-, C^-) is $P_{\mathcal{S}}^2$, there is a traveling wave connection from $P_{\mathcal{S}}^1$ to $P_{\mathcal{N}}$ plotted as a green curve in Figure 45. System (5.14)-(5.16) possesses a traveling wave solution.

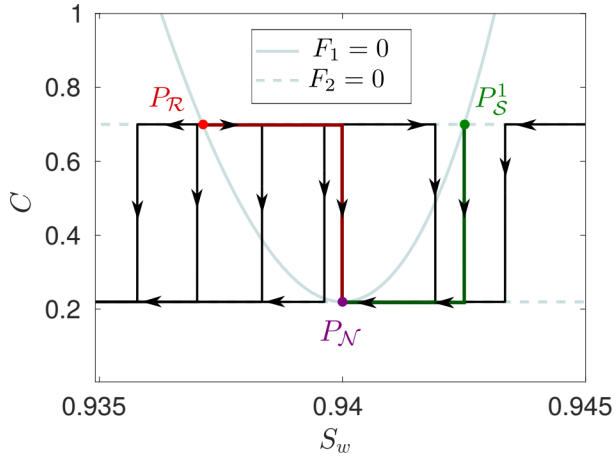

Figura 45 – Phase portrait for $(C^-, C^+) \in \mathfrak{T}$ with $C^- > C^+$. Functions F_1 and F_2 represent to right sides of (5.35) and (5.36), respectively. The red line represents the traveling wave from $P_{\mathcal{R}}$ to $P_{\mathcal{N}}$. The green line represents the traveling wave from $P_{\mathcal{S}}^1$ to (S_w^+, C^+).

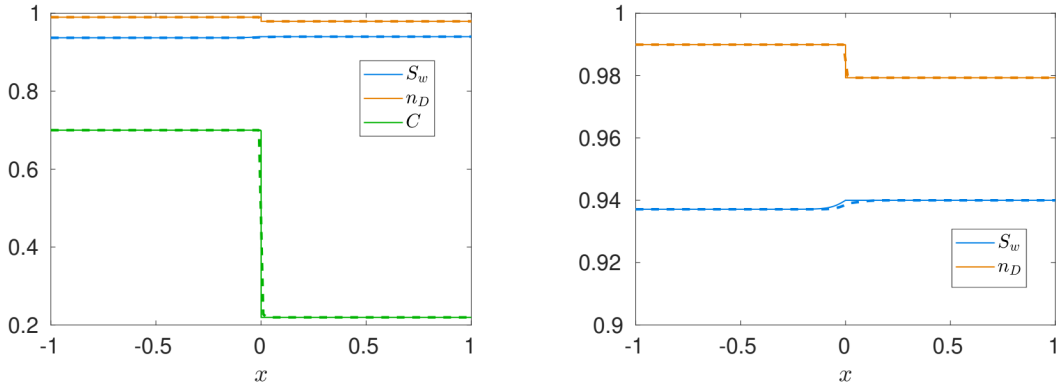

(a) (b)

Figura 46 – Solution of System (5.35)(5.37) for $(C^-, C^+) \in \mathfrak{T}$ with $C^- > C^+$ for $(S_w^-, C^-) = P_{\mathcal{R}} = (0.937126, 0.7)$ and $(S_w^+, C^+) = P_{\mathcal{N}} = (0.94, 0.219605)$. The solid line represents the analytical, and the dashed line corresponds to the numerical solution. (a) Comparison between solution profiles. (b) Zoom of Figure(a) for S_w and n_D.

5.4.10.2 Case $C^- \leq C^+$

Here, $v = v^\tau$ and the equilibria $P_{\mathcal{R}}$ and $P_{\mathcal{S}}^1$ collapse into a non-hyperbolic equilibrium (or node), which is the right equilibrium (S_w^+, C^+). Since $C^- \neq C^+$, there is no S_w^- that satisfies (5.46) nor a traveling wave connection.

5.4.11 **Curve $\mathfrak{D}$** $(C^- = C^+ < C_{cmc})$:

This case is similar to region $\mathfrak{R}^7$ and presents the same solution type as in [32, 89]. An equilibrium (S_w, C) of System (5.35)-(5.37) satisfy (5.46). Therefore, n_D in local equilibrium is constant, and it is written as

$$n_D = \frac{K_g\, C^+ \,(2C_{cmc} - C^+)}{K_g\, C^+ \,(2C_{cmc} - C^+) + K_d\, C_{cmc}^2}. \tag{5.57}$$

As presented in [32, 89], there exists a value S_w^T that represents the intersection point between $f_w(S_w, C^+)$ and the tangent line to $f_w(S_w, C^+)$ that passes through (S_w^+, f_w^+). Since $f_w(S_w, C^+)$ changes as a function of the value of $C^+ = C^-$, point S_w^T also changes depending on $C^+ = C^-$, which defines a curve presented in Figure 47. Therefore, if $S_w^- \in (S_{wc}, S_w^T(C^-))$, it possesses no traveling wave, and the solution is a wave sequence. On the other hand, if $S_w^- \in (S_w^T(C^-), S_w^+)$, there exists a traveling wave.

5.5 PARTIAL CONCLUSIONS

In this chapter, we extended a previously studied model describing the foam flow in porous media by considering the variable surfactant concentration. We obtained semi-analytical solutions for this model in the form of traveling waves using phase portrait

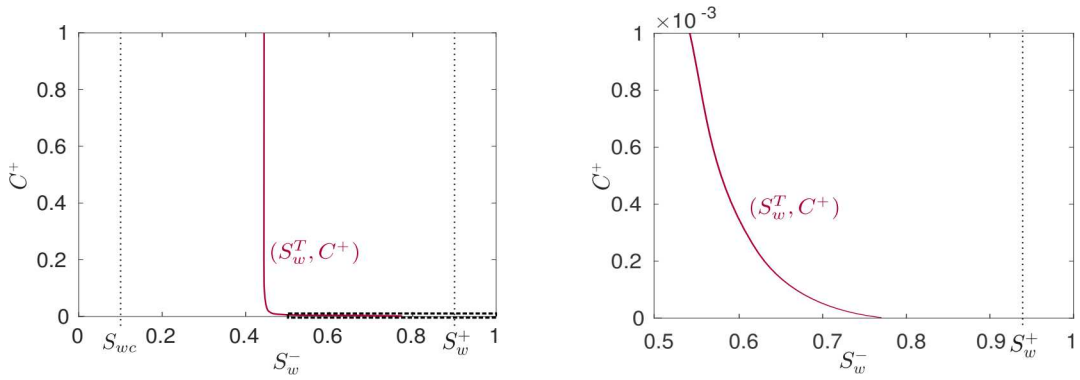

Figura 47 – Case $C^- = C^+$ with $C^- < C_{cmc}$. Value S_w^T represents the intersection point between $f_w(S_w, C^+)$ and the tangent line to $f_w(S_w, C^+)$ that passes through (S_w^+, f_w^+). In S_w^T, the type of solution changes from a sequence wave to a traveling wave. (a) Representation of all values S_w^T depending on $C^+ = C^-$. (b) Zoom of Figure(a) close to $C^+ = 0$.

analysis in a drainage scenario. We classify possible traveling wave solutions according to surfactant concentration at injection and initial conditions.

When surfactant concentrations at both injection and initial conditions are above the critical micelle concentration (CMC), the only possible traveling wave solutions occur when these concentrations are equal. As expected, the solution found in this case coincides with the one found for the simple model considering large surfactant concentrations. When surfactant concentrations at both injection and initial conditions are below the CMC, we found traveling wave solutions only in regions where surfactant concentration at the injection is greater or equal to that at the initial condition.

Our analysis allows obtaining an analytical formula for the traveling foam front, which is useful in previewing the gas breakthrough time, for example. With this equation, one can quantify how the decrease in surfactant concentration impacts the foam traveling wave front velocity.

A mathematically challenging case was found in Region $\mathfrak{R}^1$ (see Subsection 5.4.1) where there are infinite possibilities for the traveling wave connecting a source equilibria to a sink one, all of them with the same wave velocity. Although we do not have a mathematical explanation, the direct numerical simulations point out that the correct solution happens when the surfactant variation happens after the water saturation variation (inflow to outflow direction).

All obtained traveling wave solutions were validated using direct numerical simulations of the system of partial differential equations.

6 CONCLUSIONS AND DISCUSSIONS

In this thesis, different systems of partial differential equations that describe the foam displacement in porous media were analytically studied. In modeling, we assumed the dynamic behavior of foam as Newtonian. For our analysis, we considered a high initial water saturation (drainage scenario) and varied the injected water saturation. In all cases, we analyze the phase portrait of the systems of ordinary differential equations obtained from the systems of partial differential equations through a traveling variable. Traveling wave solutions were obtained and validated with direct numerical simulations.

The first model, studied in Chapter 3 and called the First Order Kinetic model (FOK), considers an abrupt weakening or collapse of foam at a limiting water saturation. The second model, studied in Chapter 4, is a simplification of the Stochastic Bubble Population model (SBP). We correlate the gas phase mobility expressions for two models (FOK and SBP models), obtaining the mobility reduction factor as a linear function of foam texture. Finally, the third model, introduced in Chapter 5, considers a separate balance equation to describe the surfactant concentration. In this case, the gas mobility is affected by surfactant concentration.

For the first two investigated models, we fixed the surfactant concentration above the critical micelle concentration. Both models, studied in this thesis, present identical solutions for relatively high values of injected water saturation, where the foam texture in local equilibrium of both models coincides. Besides, if we use in the FOK model, the same parameters of relatives permeabilities and capillary pressure used in the SBP model, then it is possible to obtain a region (Region I presented in 4.2.2), where the SBP is a particular case of FOK model as shown in [32]. The models studied in chapters 4 and 5 possess similar behaviors for all the values of injected water saturation since the surfactant concentration at the injection and initial conditions are equal. Hence, the solutions of all three models are similar for high values of injected water saturation and the surfactant concentration above the critical micelle concentration. Since the model of Chapter 4 was validated with experimental results for relatively high values of water saturation, highlighting that the velocity of the wave coincides in later times. So, in some cases, the dynamic foam behavior in porous media can be modeled as Newtonian.

For small values of injected water saturation, the models' solutions possess different behaviors. A significant difference between these models is the influence of critical water saturation in the first model. This influence can induce the presence of two types of structural instabilities close to this point. Our results suggest the need of experimental data corresponding to injected water fractional flow (or, equivalently, lower injected water saturation) to verify the validity of the investigated models.

Finally, from the model studied in Chapter 5, we noticed that the surfactant

concentration significantly influences the foam's behavior. In addition, there exists a traveling wave solution for the model with surfactant concentration below the critical micelle.

6.1 ACADEMIC CONTRIBUTIONS

During the development of the present thesis, different academic contributions were realized.
Articles published in conference proceedings, [15]:

1. J. B. Cedro, R. Q. Zavala, M. C. Coaquira, L. F. Lozano, and G. Chapiro. Estudo de um modelo cinético para escoamento de espuma em meios porosos. In XL Ibero-Latin-American Congress on Computational Methods in Engineering (CILAMCE), Natal, Brazil, 2019

Complete articles published in journals, [56, 89, 90]:

1. R. Q. Zavala, & G. Chapiro. Classification of the traveling wave solutions for filtration combustion considering thermal losses. Combustion and Flame, 2020. doi: 10.1016/j.combustflame.2020.06.017

2. L. F. Lozano, R. Q. Zavala, & G. Chapiro. Mathematical Properties of Foam Flow in Porous Media. Computational Geosciences, 2021. doi: 10.1007/s10596-020-10020-3

3. R. Q. Zavala, L. F. Lozano, P. L. J. Zitha, & G. Chapiro. Analytical solution for the population-balance model describing foam displacement. Transport in Porous Media, 2021. doi: 10.1007/s11242-021-01589-z.

Colaboration in articles published in journals, [55]:

1. L. F. Lozano, J. B. Cedro, R. Q. Zavala, & G. Chapiro. How simplifying capillary effects can affect the traveling wave solution profiles of the foam flow in porous media. International Journal of Non-Linear Mechanics, 2021.
   doi: 10.1016/j.ijnonlinmec.2021.103867.

Presentations:

1. "Analytical solution for the population-balance model describing foam displacement". Porous Media Tea Time Talks - PMTTT, Apr 2021. Presented by R. Q. Zavala. https://www.youtube.com/watch?v=2C7taEoei5g

2. “Solución analítica para el modelo de balance poblacional que describe el desplazamiento de espuma”, Apr 2022. Presented by R. V. Quispe Zavala. Congreso Internacional Multidisciplinario de Matemática (CIMM-UNI-2022) (Perú).

REFERENCES

[1] T. Ahmed. *Reservoir engineering handbook*. Elsevier, Gulf professional publishing, New York, 2018.

[2] E. Ashoori, D. Marchesin, and W. R. Rossen. Dynamic foam behavior in the entrance region of a porous medium. *Colloids and Surfaces A: Physicochemical and Engineering Aspects*, 377(1):217–227, 2011.

[3] E. Ashoori, D. Marchesin, and W. R. Rossen. Roles of transient and local equilibrium foam behavior in porous media: Traveling wave. *Colloids and Surfaces A: Physicochemical and Engineering Aspects*, 377(1):228–242, 2011.

[4] E. Ashoori, D. Marchesin, and W. R. Rossen. Multiple foam states and long-distance foam propagation in porous media. *SPE Journal*, 17(4):1231–1245, 2012.

[5] K. Aziz and A. Settari. *Petroleum reservoir simulation*. Applied Science Publishers, London, UK, 1979.

[6] T. Babadagli. Philosophy of EOR. *Journal of Petroleum Science and Engineering*, 188:106930, 2020.

[7] J. Bear. *Modeling phenomena of flow and transport in porous media*, volume 1. Springer, New York, 2018.

[8] H. J. Bertin, M. Y. Quintard, and L. M. Castanier. Development of a bubble-population correlation for foam-flow modeling in porous media. *SPE Journal*, 3(4):356–362, 1998.

[9] R. J. Biezuner. *Notas de Aula: Equações Diferenciais Parciais I/II*, volume 6. UFMG, Minas Gerais, 2010.

[10] J. Boos, W. Drenckhan, and C. Stubenrauch. On how surfactant depletion during foam generation influences foam properties. *Langmuir*, 28(25):9303–9310, 2012.

[11] R. H. Brooks and A. T. Corey. Properties of porous media affecting fluid flow. *Journal of the irrigation and drainage division*, 92(2):61–88, 1966.

[12] H. Bruining. *Upscaling of Single-and Two-Phase Flow in Reservoir Engineering*. CRC Press, 2021.

[13] S. E. Buckley and M. C. Leverett. Mechanism of fluid displacement in sands. *Transactions of the AIME*, 146(1):107–116, 1942.

[14] A. J. Castrillón, L. F. Lozano, W. S. Pereira, J. B. Cedro, and G. Chapiro. The traveling wavefront for foam flow in two-layer porous media. *Computational Geosciences*, 26(1):1549–1561, 2022.

[15] J. B. Cedro, R. V. Q. Zavala, M. C. Coaquira, L. F. Lozano, and G. Chapiro. Estudo de um modelo cinético para escoamento de espuma em meios porosos. In *XL Ibero-Latin-American Congress on Computational Methods in Engineering (CILAMCE)*, Natal, Brazil, 2019.

[16] G. Chapiro, L. Furtado, D. Marchesin, and S. Schecter. Stability of interacting traveling waves in Reaction-Convection-Diffusion systems. *DCDS*, Issue special:258–266, 2015.

[17] G. Chapiro and L. F. Lozano. Analytical solution for the population-balance model describing foam displacement considering surfactant dispersion. In *ECMOR 2022*, volume 2022, pages 1–12. European Association of Geoscientists & Engineers, 2022.

[18] G. Chapiro, A. A. Mailybaev, A. J. Souza, D. Marchesin, and J. Bruining. Asymptotic approximation of long-time solution for low-temperature filtration combustion. *Computational geosciences*, 16:799–808, 2012.

[19] G. Chapiro, D. Marchesin, and S. Schecter. Combustion waves and Riemann solutions in light porous foam. *Journal of Hyperbolic Differential Equations*, 11(02):295–328, 2014.

[20] G. Chapiro and L. Senos. Riemann solutions for counterflow combustion in light porous foam. *Computational and Applied Mathematics*, 37(2):1721–1736, 2018.

[21] Z. Chen, G. Huan, and Y. Ma. *Computational methods for multiphase flows in porous media*. Society for Industrial and Applied Mathematics, Texas, USA, 2006.

[22] L. Cheng, A. B. Reme, D. Shan, D. A. Coombe, and W. R. Rossen. *Simulating foam processes at high and low foam qualities*. Society of Petroleum Engineers, Tulsa, OK, 2000.

[23] R. E. Collins. *Flow of fluids through porous materials*. Petroleum Publishing Co., Tulsa, OK, 1976.

[24] A. T. Corey. The interrelation between gas and oil relative permeabilities. *Producers monthly*, pages 38–41, 1954.

[25] H. R. P. G. Darcy. Les fontaines publiques de la ville de dijon. *The Flow of Homogeneous Fluids Through Porous Media*, 1856.

[26] Ø. Eide, M. Fernø, S. Bryant, A. Kovscek, and J. Gauteplass. Population-balance modeling of CO2 foam for CCUS using nanoparticles. *Journal of Natural Gas Science and Engineering*, 80:103378, 2020.

[27] L. C. Evans. *Partial Differential Equations*, volume 19. American Mathematical Society, Providence, Rhode Island, 2nd edition, 2010.

[28] D. Exerowa and P. M. Kruglyakov. *Foam and foam films: Theory, experiment and application*, volume 5 of *Studies in Interface Science*. Elsevier, Amsterdam, 1998.

[29] A. H. Falls, G. J. Hirasaki, T. W. Patzek, D. A. Gauglitz, D. D. Miller, and T. Ratoulowski. Development of a mechanistic foam simulator: The population balance and generation by snap-off. *SPE Reservoir Engineering*, 3:884–892, 1988.

[30] R. Farajzadeh, A. A. Eftekhari, H. Hajibeygi, S. Kahrobaei, J. M. Van der Meer, S. Vincent-Bonnieu, and W. S. Rossen. Simulation of instabilities and fingering in surfactant alternating gas (SAG) foam enhanced oil recovery. *Journal of Natural Gas Science and Engineering*, 34:1191–1204, 2016.

[31] F. Friedmann, W. H. Chen, and P. A. Gauglitz. Experimental and simulation study of high-temperature foam displacement in porous media. *SPE Reservoir Engineering*, 6(1):37–45, 1991.

[32] G. Fritis, L. Lozano, and G. Chapiro. Analise de produção avançada de petróleo usando espumas através de novas ferramentas analíticas. In *Rio Oil & Gas Expo And Conference*, 2022.

[33] B. H. Gilding and R. Kersner. *Travelling waves in nonlinear Diffusion-Convection-Reaction*, volume 60. Birkhäuser, Basel, 2012.

[34] J. Guckenheimer and P. J. Holmes. *Nonlinear oscillations, dynamical systems, and bifurcations of vector fields*, volume 42. Springer, New York, 2013.

[35] H. Hematpur, S. M. Mahmood, N. H. Nasr, and K. A. Elraies. Foam flow in porous media: Concepts, models and challenges. *Journal of Natural Gas Science and Engineering*, 53:163–180, 2018.

[36] G. J. Hirasaki. The steam-foam process. *Journal of Petroleum Technology*, 41(5):449–456, 1989.

[37] G. J. Hirasaki and J. B. Lawson. Mechanisms of foam flow in porous media: Apparent viscosity in smooth capillaries. *SPE Journal*, 25(2):176–190, 1985.

[38] G. J. Hirasaki, C. A. Miller, R. Szafranski, J. B. Lawson, and N. Akiya. Surfactant/foam process for aquifer remediation. In *International symposium on oilfield chemistry*, pages 471–480, Texas, USA, 1997. SPE.

[39] M. R. Islam and S. M. Farouq Ali. Numerical simulation of foam flow in porous media. *Journal of Canadian Petroleum Technology*, 29(4):47–51, 1990.

[40] M. T. G. Janssen, F. A. Torres Mendez, and P. L. J. Zitha. Mechanistic modeling of Water-Alternating-Gas injection and foam-assisted chemical flooding for Enhanced Oil Recovery. *Industrial & Engineering Chemistry Research*, 59(8):3606–3616, 2020.

[41] M. T. G. Janssen, R. M. Pilus, and P. L. J. Zitha. A comparative study of gas flooding and foam-assisted chemical flooding in bentheimer sandstones. *Transport in Porous Media*, 131(1):101–134, 2020.

[42] S. A. Jones, G. Laskaris, S. Vincent-Bonnieu, R. Farajzadeh, and W. R. Rossen. Effect of surfactant concentration on foam: From coreflood experiments to implicit-texture foam-model parameters. *Journal of Industrial and Engineering Chemistry*, 37:268–276, 2016.

[43] S. Kahrobaei and R. Farajzadeh. Insights into effects of surfactant concentration on foam behavior in porous media. In *IOR 2019–20th European Symposium on Improved Oil Recovery*, volume 2019, pages 1–13. European Association of Geoscientists & Engineers, 2019.

[44] S. I. Kam. Improved mechanistic foam simulation with foam catastrophe theory. *Colloids and Surfaces A: Physicochemical and Engineering Aspects*, 318(1):62–77, 2008.

[45] S. I. Kam, Q. P. Nguyen, Q. Li, and W. R. Rossen. Dynamic simulations with an improved model for foam generation. *SPE Journal*, 12(1):35–48, 2007.

[46] H. Kharabaf and Y. C. Yortsos. Solution of hyperbolic equations involving chemical reactions. *Industrial & engineering chemistry research*, 34(8):2728–2732, 1995.

[47] A. R. Kovscek, Q. Chen, and M. Gerritsen. Modeling foam displacement with the local-equilibrium approximation: Theory and experimental verification. *SPE Journal*, 15(1):171–183, 2010.

[48] A. R. Kovscek, T. W. Patzek, and C. J. Radke. A mechanistic population balance model for transient and steady-state foam flow in Boise sandstone. *Chemical Engineering Science*, 50(23):3783–3799, 1995.

[49] L. Lake. *Enhanced oil recovery*. Prentice Hall, New Jersey, 1989.

[50] W. Lambert, A. Alvarez, I. Ledoino, D. Tadeu, D. Marchesin, and J. Bruining. Mathematics and numerics for balance Partial Differential-Algebraic Equations (PDAEs). *Journal of Scientific Computing*, 84(2):1–56, 2020.

[51] D. Langevin. Rheology of adsorbed surfactant monolayers at fluid surfaces. *Annual Review of Fluid Mechanics*, 46:47–65, 2014.

[52] P. D. Lax. Hyperbolic systems of conservation laws II. *Communications on pure and applied mathematics*, 10(4):537–566, 1957.

[53] K. Li and R. N. Horne. Comparison of methods to calculate relative permeability from capillary pressure in consolidated water-wet porous media. *Water Resources Research*, 42(6):1–9, 2006.

[54] M. Lotfollahi, R. Farajzadeh, M. Delshad, A. Varavei, and W. R. Rossen. Comparison of implicit-texture and population-balance foam models. *Journal of Natural Gas Science and Engineering*, 31:184–197, 2016.

[55] L. F. Lozano, J. B. Cedro, R. Q. Zavala, and G. Chapiro. How simplifying capillary effects can affect the traveling wave solution profiles of the foam flow in porous media. *International Journal of Non-Linear Mechanics*, 139:103867, 2022.

[56] L. F. Lozano, R. Q. Zavala, and G. Chapiro. Mathematical properties of the foam flow in porous media. *Computational Geosciences*, 25(1):515–527, 2021.

[57] K. Ma, J. L. Lopez-Salinas, M. C. Puerto, C. A. Miller, S. L. Biswal, and G. J. Hirasaki. Estimation of parameters for the simulation of foam flow through porous media. part 1: The dry-out effect. *Energy & fuels*, 27(5):2363–2375, 2013.

[58] K. Mannhardt, L. L. Schramm, and J. J. Novosad. Adsorption of anionic and amphoteric foam-forming surfactants on different rock types. *Colloids and surfaces*, 68(1-2):37–53, 1992.

[59] S. S. Marsden and S. A. Khan. The flow of foam through short porous media and apparent viscosity measurements. *SPE Journal*, March:17–25, 1966.

[60] S. Mohammadi, D. Coombe, and V. Stevenson. Test of steam-foam process for mobility control in south Casper Creek reservoir. *Journal of Canadian Petroleum Technology*, 32(10):49–54, 1993.

[61] O. A. Oleĭnik. On the uniqueness of generalized solution of cauchy problem for non linear system of equations ocurring in mechanics. *Uspekhi Mat. Nauk*, 12(6(78)):169–176, 1957.

[62] F. Ozbag, S. Schecter, and G. Chapiro. Traveling waves in a simplified gas-solid combustion model in porous media. *Advances in differential equations*, 23(5/6):409–454, 2018.

[63] L. Perko. *Differential equations and dynamical systems*, volume 7. Springer Science & Business Media, New York, 2013.

[64] G. A. Pope. The application of fractional flow theory to enhanced oil recovery. *Society of Petroleum Engineers Journal*, 20(3):191–205, 1980.

[65] J. L. Randall. Numerical methods for conservation laws. *Lectures in Mathematics ETH Zürich*, 1992.

[66] L. Romero-Zerón. *Introduction to enhanced oil recovery (EOR) processes and bioremediation of oil-contaminated sites*. BoD–Books on Demand, InTech, Rijeka, 2012.

[67] W. R. Rossen. Foams in enhanced oil recovery. *Foams: Theory, measurements and applications*, 57:413–464, 1996.

[68] W. R. Rossen. *Numerical challenges in foam simulation: A review*. Society of Petroleum Engineers, New Orleans, Louisiana, USA, 2013.

[69] W. R. Rossen and J. Bruining. Foam displacements with multiple steady states. In *SPE/DOE Symposium on Improved Oil Recovery*, Oklahoma, USA, 2004. SPE.

[70] W. R. Rossen and C. J. Van Duijn. Gravity segregation in steady-state horizontal flow in homogeneous reservoirs. *Journal of Petroleum Science and Engineering*, 43(1-2):99–111, 2004.

[71] W. R. Rossen and P. A. Gauglitz. Percolation theory of creation and mobilization of foams in porous media. *AIChE Journal*, 36(8):1176–1188, 1990.

[72] D. Shan and W. R. Rossen. Optimal injection strategies for foam IOR. *SPE Journal*, 9(02):132–150, 2004.

[73] M. Simjoo, Y. Dong, A. Andrianov, M. Talanana, and P. L. J. Zitha. Novel insight into foam mobility control. *SPE Journal*, 18(3):416–427, 2013.

[74] M. Simjoo and P. L. J. Zitha. Modeling of foam flow using stochastic bubble population model and experimental validation. *Transport in Porous Media*, 107(3):799–820, 2015.

[75] J. Smoller. *Shock waves and Reaction-Diffusion equations*, volume 258. Springer-Verlag New York, New York, 1994.

[76] J. Sotomayor. *Curvas definidas por equações diferenciais no plano*. Instituto de Matemática Pura e Aplicada, Rio de Janeiro, 1981.

[77] S. Talebian, R. Masoudi, I. Tan, and P. Zitha. Foam assisted CO2-EOR: A review of concept, challenges, and future prospects. *Journal of Petroleum Science and Engineering*, 120:202–215, 2014.

[78] J. Tang, P. Castañeda, D. Marchesin, and W. R. Rossen. Three-phase fractional-flow theory of foam-oil displacement in porous media with multiple steady states. *Water Resources Research*, 2019.

[79] J. H. M. Thomeer. Introduction of a pore geometrical factor defined by the capillary pressure curve. *J. Pet. Technol.*, 12(03):73–77, 1960.

[80] R. Thorat and H. Bruining. Foam flow experiments. I. Estimation of the bubble generation-coalescence function. *Transport in Porous Media*, 112(1):53–76, 2016.

[81] J. M. van der Meer, R. Farajzadeh, W. R. Rossen, and J. D. Jansen. Influence of foam on the stability characteristics of immiscible flow in porous media. *Physics of Fluids*, 30(1):014106, 2018.

[82] C. J. van Duijn. *An introduction to conservation laws: Theory and applications to multi-phase flow*. Eindhoven University of Technology, The Netherlands, 2003.

[83] M. T. Van Genuchten. A closed-form equation for predicting the hydraulic conductivity of unsaturated soils. *Soil science society of America journal*, 44(5):892–898, 1980.

[84] A. I. Volpert, V. A. Volpert, and V. A. Volpert. *Traveling wave solutions of parabolic systems*, volume 140. American Mathematical Soc., Providence, Rhode Island, 1994.

[85] M. P. Walsh and L. W. Lake. Applying fractional flow theory to solvent flooding and chase fluids. *Journal of Petroleum Science and Engineering*, 2(4):281–303, 1989.

[86] S. Wang and C. N. Mulligan. An evaluation of surfactant foam technology in remediation of contaminated soil. *Chemosphere*, 57(9):1079–1089, 2004.

[87] D. L. Weaire and S. Hutzler. *The physics of foams*. Oxford University Press, Clarendon Press, Oxford, 2001.

[88] H. Yunfei, S. Yazhuo, L. Honglai, L. Dominique, and S. Anniina. Surfactant adsorption onto interfaces: measuring the surface excess in time. *Langmuir*, 28(6):3146–3151, 2012.

[89] R. Q. Zavala, L. F. Lozano, P. L. J. Zitha, and G. Chapiro. Analytical solution for the population-balance model describing foam displacement. *Transport in Porous Media*, pages 1–17, 2021.

[90] R.V. Q. Zavala and G. Chapiro. Classification of the traveling wave solutions for filtration combustion considering thermal losses. *Combustion and Flame*, 219:416–424, 2020.

[91] Z. F. Zhang, V. L. Freedman, and L. Zhong. *Foam transport in porous media: A review*. Pacific Northwest National Lab.(PNNL), Richland, WA (United States), 2009.

[92] Z. H. Zhou and W. R. Rossen. Applying fractional-flow theory to foams for diversion in matrix acidization. *SPE Production & Facilities*, 9(1):29–35, 1994.

[93] Z. H. Zhou and W. R. Rossen. Applying fractional-flow theory to foam processes at the limiting capillary pressure. *SPE Advanced Technology Series*, 3(01):154–162, 1995.

[94] P. L. J. Zitha and D. X. Du. A new stochastic bubble population model for foam flow in porous media. *Transport in Porous Media*, 83(3):603–621, 2010.

APPENDIX A – Variation in parameter A

A.1 Maintaining $S_w^+ = 0.72$. and considering $A = 10$.

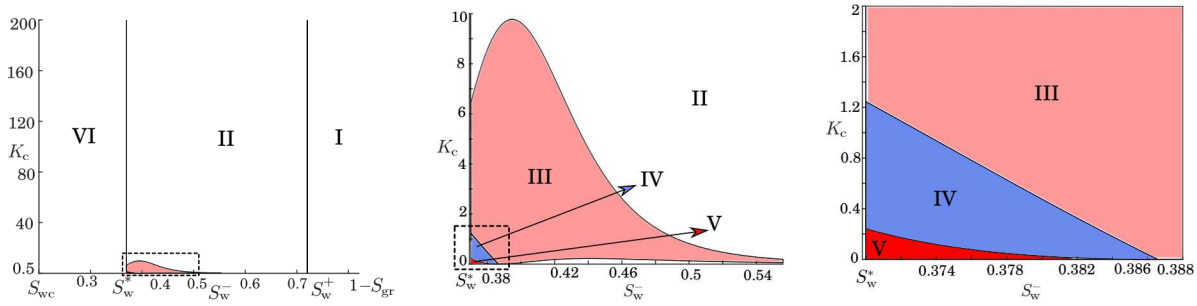

(a) (b) (c)

Figura R_1 – Classification of the eigenvalues of the Jacobian matrix associated to the vector field of (3.12)-(3.13) in the semi plane $[S_{wc}, 1 - S_{gr}] \times K_c$ for $A = 10$ and $S_w^+ = 0.72$. (a) As we can see, decreasing A, the size of regions **III**, **IV**, and **V** decrease in K_c and increase in S_w, when compared with the original plot in Fig. 3. (b) Zoom of the small area close to S_w^* indicated by a black rectangle in the panel (a). Notice that the pinched part of Region **III** in Region **II** remains and increases in size. (c) Zoom of the small area close to S_w^* indicated by a black rectangle in the panel (b). The relative position of regions **IV** and **V** do not change.

A.2 Maintaining $S_w^+ = 0.72$. and considering $A = 100$.

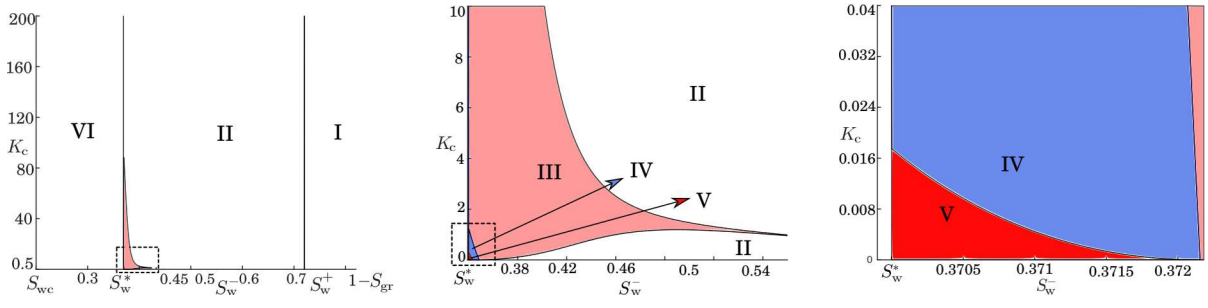

(a) (b) (c)

Figura R_2 – Classification of the eigenvalues of the Jacobian matrix associated to the vector field of (3.12)-(3.13) in the semi plane $[S_{wc}, 1 - S_{gr}] \times K_c$ for $A = 100$ and $S_w^+ = 0.72$. (a) As we can see, decreasing A, the size of regions **III**, **IV**, and **V** decrease in K_c and increase in S_w, when compared with the original plot in Fig. 3. (b) Zoom of the small area close to S_w^* indicated by a black rectangle in the panel (a). Notice that the pinched part of Region **III** in Region **II** remains and increases in size. (c) Zoom of the small area close to S_w^* indicated by a black rectangle in the panel (b). The relative position of regions **IV** and **V** do not change.

A.3 Maintaining $S_w^+ = 0.72$. and considering $A = 200$.

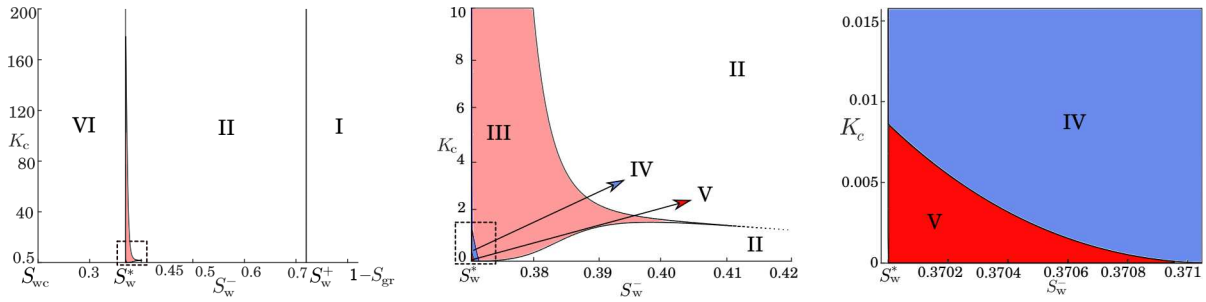

(a) (b) (c)

Figura R_3 – Classification of the eigenvalues of the Jacobian matrix associated to the vector field of (3.12)-(3.13) in the semi plane $[S_{wc}, 1 - S_{gr}] \times K_c$ for $A = 200$ and $S_w^+ = 0.72$. (a) As we can see, decreasing A, the size of regions **III**, **IV**, and **V** decrease in K_c and increase in S_w, when compared with the original plot in Fig. 3. (b) Zoom of the small area close to S_w^* indicated by a black rectangle in the panel (a). Notice that the pinched part of Region **III** in Region **II** remains and increases in size. (c) Zoom of the small area close to S_w^* indicated by a black rectangle in the panel (b). The relative position of regions **IV** and **V** do not change.

A.4 Maintaining $S_w^+ = 0.72$. and considering $A = 300$.

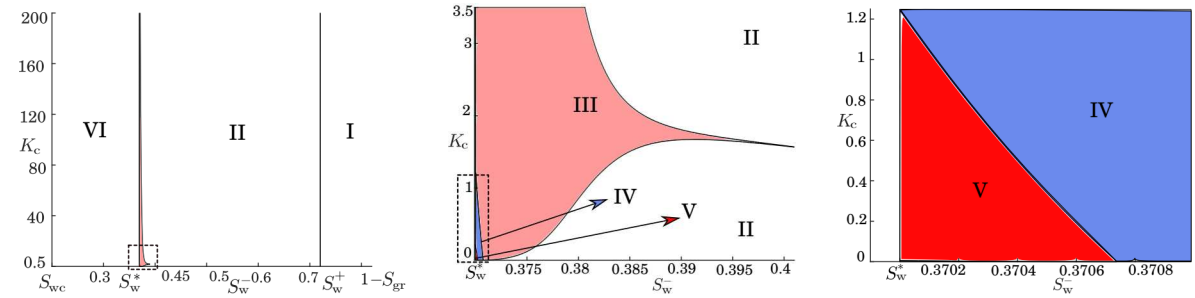

(a) (b) (c)

Figura R_4 – Classification of the eigenvalues of the Jacobian matrix associated to the vector field of (3.12)-(3.13) in the semi plane $[S_{wc}, 1 - S_{gr}] \times K_c$ for $A = 300$ and $S_w^+ = 0.72$. (a) As we can see, decreasing A, the size of regions **III**, **IV**, and **V** decrease in K_c and increase in S_w, when compared with the original plot in Fig. 3. (b) Zoom of the small area close to S_w^* indicated by a black rectangle in the panel (a). Notice that the pinched part of Region **III** in Region **II** remains and increases in size. (c) Zoom of the small area close to S_w^* indicated by a black rectangle in the panel (b). The relative position of regions **IV** and **V** do not change.

A.5 Maintaining $S_w^+ = 0.72$. and considering $A = 500$.

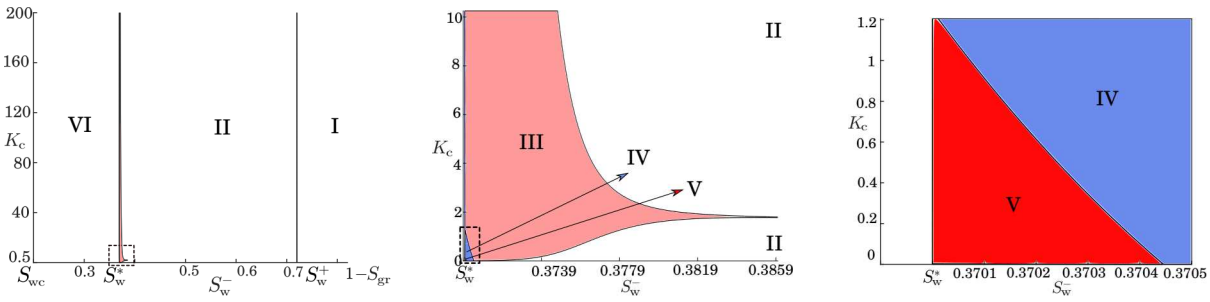

(a) (b) (c)

Figura R_5 – Classification of the eigenvalues of the Jacobian matrix associated to the vector field of (3.12)-(3.13) in the semi plane $[S_{wc}, 1 - S_{gr}] \times K_c$ for $A = 500$ and $S_w^+ = 0.72$. (a) As we can see, increasing A, the size of regions **III**, **IV**, and **V** increase in K_c and decrease in S_w, when compared with the original plot in Fig. 3. (b) Zoom of the small area close to S_w^* indicated by a black rectangle in the panel (a). Notice that the pinched part of Region **III** in Region **II** remains and decreases in size. (c) Zoom of the small area close to S_w^* indicated by a black rectangle in the panel (b). The relative position of regions **IV** and **V** do not change.

APPENDIX B – Variation in parameter S_w^+

B.1 Maintaining $A = 400$ and considering $S_w^+ = 0.68$.

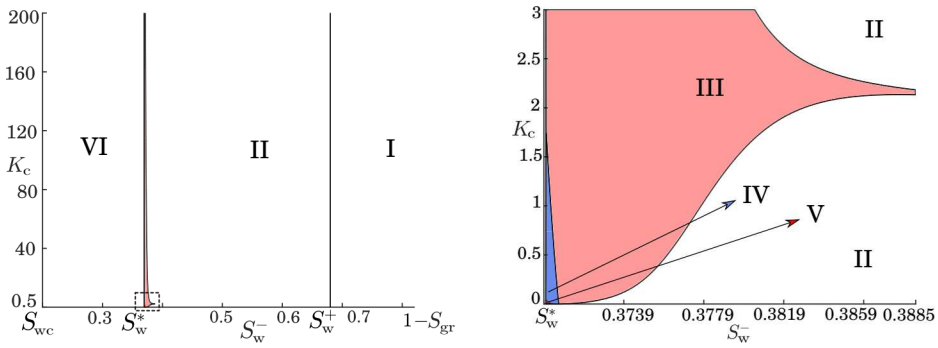

Figura R_6 – Classification of the eigenvalues of the Jacobian matrix associated to the vector field of (3.12)-(3.13) in the semi plane $[S_{wc}, 1 - S_{gr}] \times K_c$ for $A = 400$ and $S_w^+ = 0.68$. (a) As we can see, decreasing S_w, the size of regions **III**, **IV**, and **V** increase in K_c and decrease in S_w, when compared with the original plot in Fig. 3. (b) Zoom of the small area close to S_w^* indicated by a black rectangle in the panel (a). Notice that the pinched part of Region **III** in Region **II** remains and decreases in size.

B.2 Maintaining $A = 400$ and considering $S_w^+ = 0.55$.

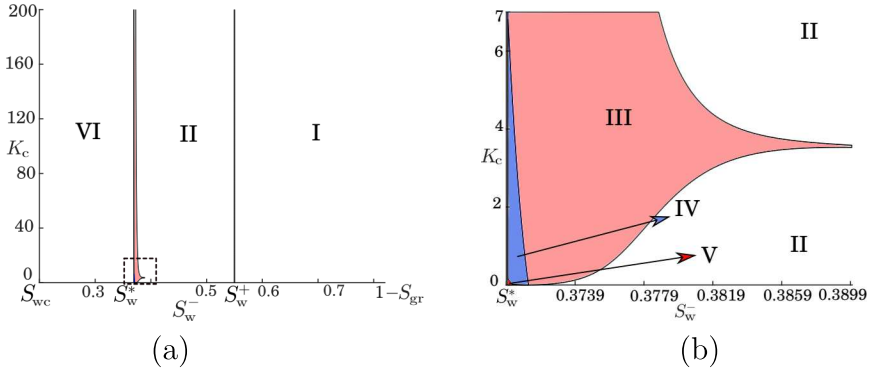

Figura R_7 – Classification of the eigenvalues of the Jacobian matrix associated to the vector field of (3.12)-(3.13) in the semi plane $[S_{wc}, 1 - S_{gr}] \times K_c$ for $A = 400$ and $S_w^+ = 0.55$. (a) As we can see, decreasing S_w, the size of regions **III**, **IV**, and **V** increase in K_c and decrease in S_w, when compared with the original plot in Fig. 3. (b) Zoom of the small area close to S_w^* indicated by a black rectangle in the panel (a). Notice that the pinched part of Region **III** in Region **II** remains and decreases in size.

B.3 Maintaining $A = 400$ and considering $S_w^+ = 0.47$.

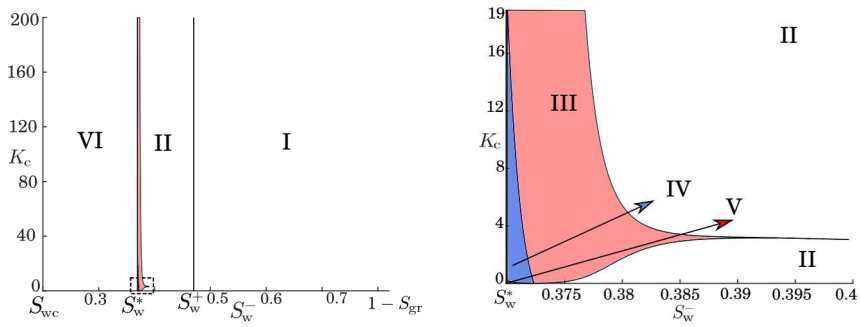

Figura R_8 – Classification of the eigenvalues of the Jacobian matrix associated to the vector field of (3.12)-(3.13) in the semi plane $[S_{wc}, 1 - S_{gr}] \times K_c$ for $A = 400$ and $S_w^+ = 0.47$. (a) As we can see, decreasing S_w, the size of regions **III**, **IV**, and **V** increase in K_c and decrease in S_w, when compared with the original plot in Fig. 3. (b) Zoom of the small area close to S_w^* indicated by a black rectangle in the panel (a). Notice that the pinched part of Region **III** in Region **II** remains and decreases in size.